POLITECNICO DI TORINO

DIPARTIMENTO DI INGEGNERIA MECCANICA E AEROSPAZIALE
Corso di Laurea Magistrale in **Ingegneria Aerospaziale**

Tesi di Laurea Magistrale

Low-Thrust Many-Revolutions maneuver optimization for future active debris removal applications

Candidato:
Andrea Verri
Matricola s258336

Professore:
Lorenzo Casalino

Anno Accademico 2021-2022

Contents

List of Figures

List of Tables

1 Introduction

1.1 Purpose of the study

In the last sixty years, space activity has increased exponentially. Satellites in orbit are used for countless purposes and they represent a unique resource for collecting scientific data and for creating new commercial opportunities and various essential applications and services.

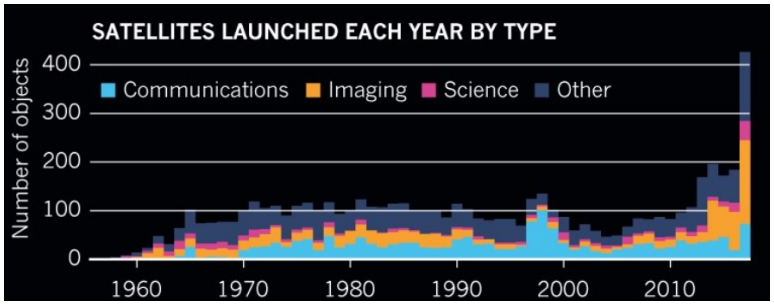

Figure 1.1: Satellites launched each year by type

However, as a consequence of this progressive growth (figure 1.1), a new hazard has become a concrete reality: *space debris*.
The great presence of space debris around Earth, and its continuous rise in number and mass, represents a big deal for active and future space missions, due to possible fatal collision, to the point that the majority of space agencies are busily dealing with the problem. In order to understand the relevance of this issue, it's enough to think that near Earth orbit is so polluted with "space junk" that the International Space Station is continuously moved to avoid impact with dangerous chunks of space debris. The solution is represented by *active debris removal mission*.
The purpose of the present study regards the utilization of an indirect method to achieve an optimization of low-thrust many revolutions maneuver for future active debris removal applications. Since multiple target missions would have a greater impact on space debris reduction, a minimal fuel consumption must be achieved, even accepting greater mission times. Electric propulsion is a suitable technology to achieve a low-consumption mission.

1.2 Space debris

Space debris is defined as all the inactive, man-made objects, including fragments, that are orbiting Earth or reentering the atmosphere. There have only been human-made objects in space since the start of the Space Age on October 4, 1957 with the launch of the first artificial satellite, Sputnik 1, till today, with more than 5560 launches made. About 24% of the cataloged objects are satellites, and about 18% are spent upper stages and mission--related objects such as launch adapters and lens covers. The greatest part of cataloged objects are caused by more than 500 break-ups in orbit, due to explosions, collisions or anomalous events. Major contribution to the population of fragments comes from a Chinese anti-satellite test targeting the Feng Yun-1C weather satellite on 11 January 2007, which created more than 3400 tracked fragments, and the approximately 2300 tracked fragments created from the first-ever accidental collision between two satellites, Iridium-33 and Cosmos-2251, on 10 February 2009. According to the latest data available, estimated by statistical models, the number of debris could be divided in: 34000 objects bigger than 10 cm (the main source of information on large space debris is the US Space Surveillance Network), 900.000 objects from grater than 1 cm to 10 cm and 128 million objects from greater than 1 mm to 1 cm.

Debris inside the space environment can be divided in two categories: the ones which can be traced back to a specific launch event with a well-defined nature and the ones untraceable. The last ones are defined as "Unidentified", whereas the first ones as:

- **Payloads**, space object designed to perform a specific function in space excluding launch functionality. This includes operational satellites as well as calibration objects.
- **Payload mission related objects**, space objects released as space debris which served a purpose for the functioning of a payload. Common examples include covers for optical instruments or astronaut tools.
- **Payload fragmentation debris**, space objects fragmented or unintentionally released from a payload as space debris for which their genesis can be traced back to a unique event. This class includes objects created when a payload explodes or when it collides with another object.

- **Payload debris**, space objects fragmented or unintentionally released from a payload as space debris for which the genesis is unclear but orbital or physical properties enable a correlation with a source.
- **Rocket body**, space object designed to perform launch related functionality; This includes the various orbital stages of launch vehicles, but not payloads which release smaller payloads themselves.
- **Rocket mission related objects**, space objects intentionally released as space debris which served a purpose for the function of a rocket body. Common examples include shrouds and engines.
- **Rocket fragmentation debris**, space objects fragmented or unintentionally released from a rocket body as space debris for which their genesis can be traced back to a unique event. This class includes objects created when a launch vehicle explodes.
- **Rocket debris**, space objects fragmented or unintentionally released from a rocket body as space debris for which the genesis is unclear but orbital or physical properties enable a correlation with a source.

Objects that are classified as general Payloads and Rocket debris will be reclassified when more information can be gathered. For a clear vision of the following chart, an abbreviation has been defined for each class of objects as follow(Table 1.1):

Table 1.1: Object classification

Type	**Description**
PL	Payload
PF	Payload Fragmentation Debris
PD	Payload Debris
PM	Payload Mission Related Object
RB	Rocket Body
RD	Rocket Debris
RM	Rocket Mission Related Object
UI	Unidentified

Once the space debris has been defined, it's possible to visualize a chart-trend of quantity, mass and occupied area of all space objects divided in the previous categories in Figure 1.2, Figure 1.3 and Figure 1.4.

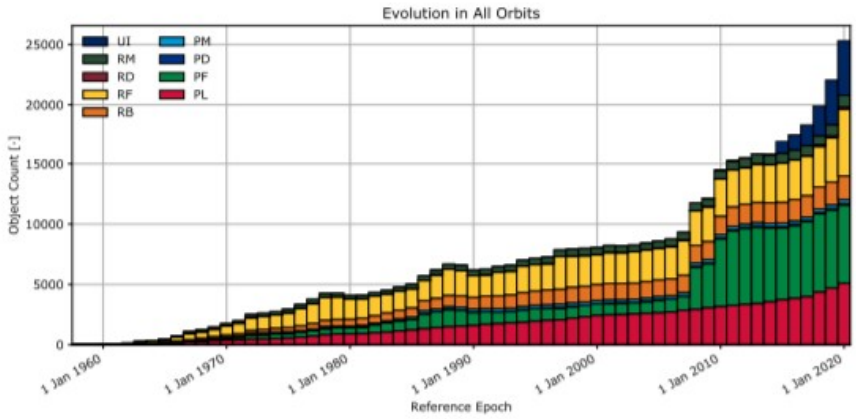

Figure 1.2: Number of objects divided by type

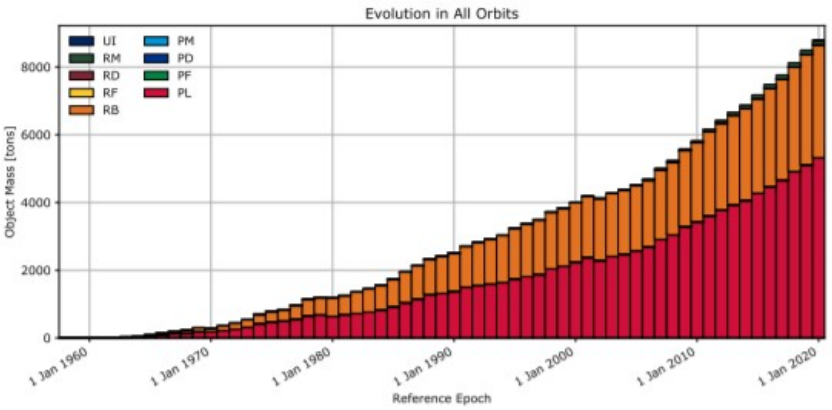

Figure 1.3: Evolution of total mass divided by type

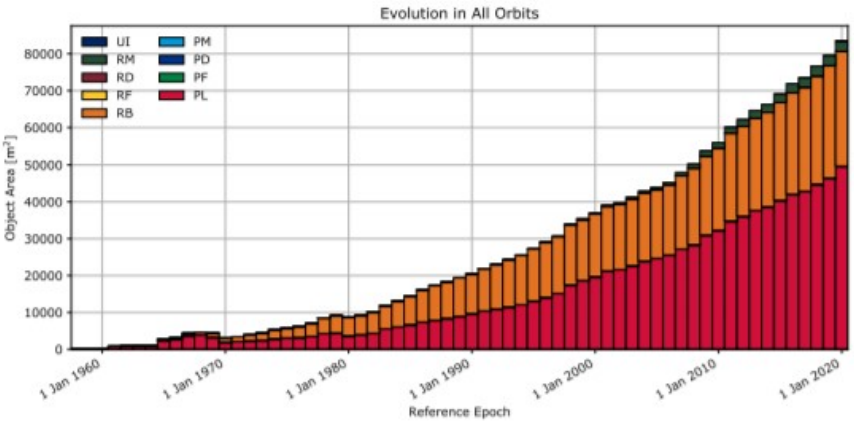

Figure 1.4: Evolution of total occupied area divided by type

The general growth trend can be seen on these charts, where Rocket body and Payload occupied a huge percentage of total mass and area occupied around all Earth Orbits. In terms of number, Payload Fragments and Rocket fragments play a huge role. The two main events of debris creation, the Chinese anti-satellite test on Feng Yun-1C weather satellite and the first-ever accidental collision between two satellites, Iridium-33 and Cosmos-2251, can be seen in Figure 2 where, in correspondence of years 2007 and 2009, takes place a well visible discontinuity.
Once the space debris has been divided by different types, it's possible to take a step forward and analyze for each orbit: mass, quantity and area occupied by space objects. First of all a preliminary description of different orbits is necessary(table 1.2):

Table 1.2: Orbital classes Description

Orbit	**Description**
GEO	Geostationary Orbit
IGO	Inclined Geosynchronous Orbit
EGO	Extended Geostationary Orbit
NSO	Navigation Satellites Orbit
GTO	GEO Transfer Orbit
MEO	Medium Earth Orbit
GHO	GEO-superGEO Crossing Orbits
LEO	Low Earth Orbit
HAO	High Altitude Earth Orbit
MGO	MEO-GEO Crossing Orbits
HEO	Highly Eccentric Earth Orbit
LMO	LEO-MEO Crossing Orbits
UFO	Undefined Orbit
ESO	Escape Orbits

Coupled to the description table is added an orbital classes definition through semi-major axis a, eccentricity e, inclination i, perigee height hp and apogee height ha (table 1.3). The units are km for heights and degrees for angles.

Table 1.3: Orbital classes Definition

Orbit	**Definition**
GEO	$i \in [0, 25], hp \in [35586, 35986], ha \in [35586, 35986]$
IGO	$a \in [37948, 46380], e \in [0.00, 0.25], i \in [25, 180]$
EGO	$a \in [37948, 46380], e \in [0.00, 0.25], i \in [0, 25]$
NSO	$i \in [50, 70], hp \in [18100, 24300], ha \in [18100, 24300]$
GTO	$i \in [0, 90], hp \in [0, 2000], ha \in [31570, 40002]$
MEO	$hp \in [2000, 31570], ha \in [2000, 31570]$
GHO	$hp \in [31570, 40002], ha > 40002$
LEO	$hp \in [0, 2000].ha \in [0, 2000]$
HAO	hp > 40002, ha > 40002
MGO	$hp \in [2000, 31570], ha \in [31570, 40002]$
HEO	$hp \in [0, 31570], ha > 40002$
LMO	$hp \in [0, 2000], ha \in [2000, 31570]$

It's now possible to visualize in figure 1.5, 1.6, 1.7 the trend-chart of space objects quantity, mass and occupied area for each type of orbital class. This study is necessary to find the most crowded orbit around Earth and discuss the nature of space objects that populate those regions.

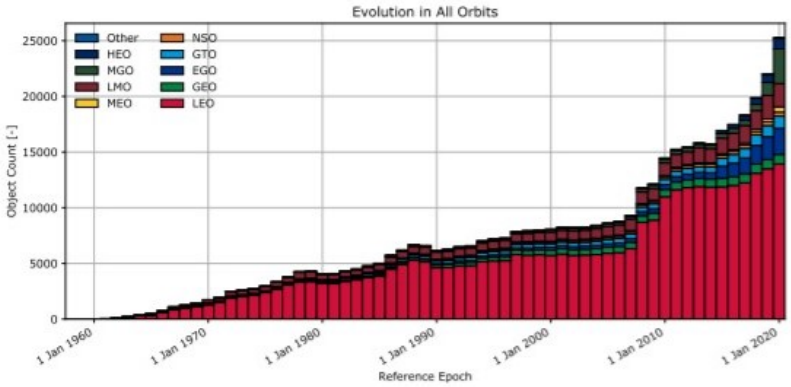

Figure 1.5: Number of objects divided by orbital class

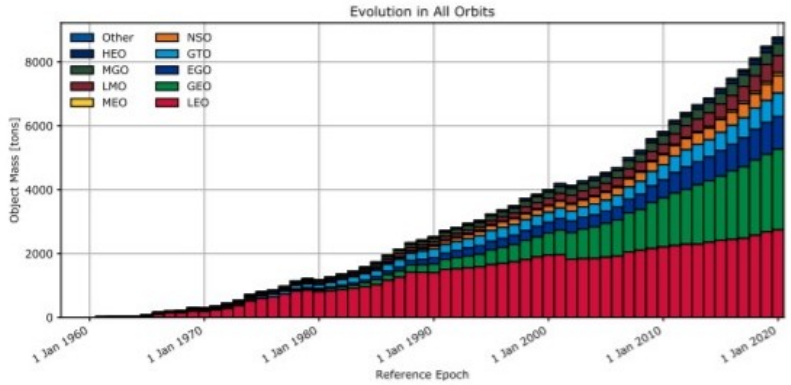

Figure 1.6: Evolution of total mass divided by orbital class

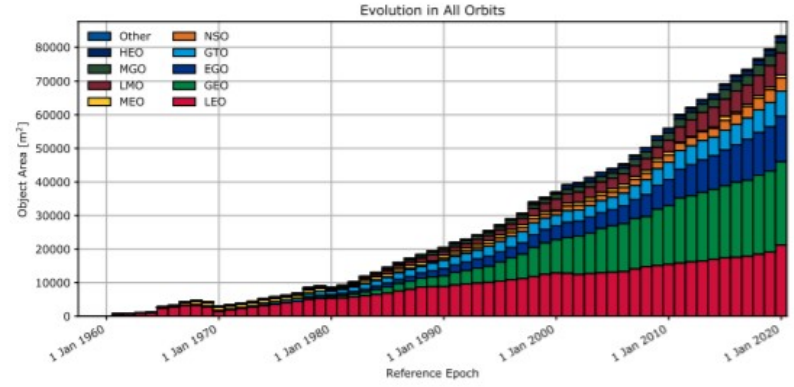

Figure 1.7: Evolution of total occupied area divided by orbital class

It's clear that the most crowded orbit in terms of quantity is Low Earth Orbit, but in terms of mass and occupied area even Geostationary orbit play a huge role. This is probably due to the fact that in Low Earth Orbit a huge amount of space debris is quite small and quantity dominates mass and occupied area.

1.3 Debris Measuraments

In order to obtain successfully measurements of space debris, modern technologies, such as ground-based radars and optical telescopes, space-based sensors, analysis of spacecraft surfaces returned from space, and ground-based laboratory experiments, such as *DebriSat*, are used. Some important data sources have been the U.S. Space Surveillance Network, the Haystack X-Band Radar, and returned surfaces from the Solar Max, the Long Duration Exposure Facility (LDEF), the Hubble Space Telescope (HST), and the Space Shuttle (figure 1.8).

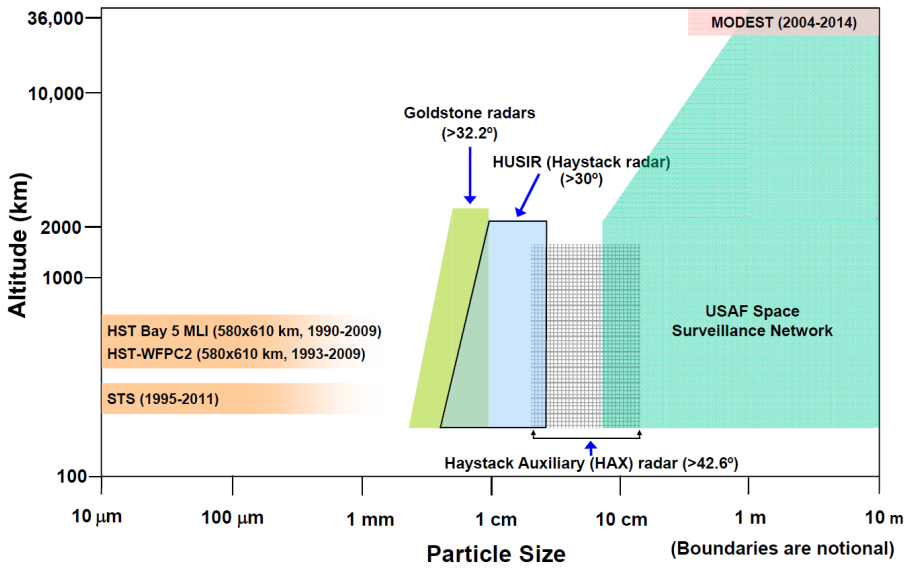

Figure 1.8: Space Debris Measuraments

Due to technological limitations it's impossible to trace every single space debris, in fact existing catalogs are typically limited to objects larger than 5–10 cm at low altitudes (LEO) and larger than 0.3–1 m at high altitudes (GEO). Passive optical telescopes are suited mainly for observing high alti-

tudes, over 2000 km, whereas radars work fine over 2000 km. An emerging technology is represented by Satellite Laser-Raging, which has been proved very effective for the detection and follow up of intact objects or fragments and for their attitude determination. Small debris, from the millimeter to centimeter range, is hardly traceable since space debris environment models are not suited for this class. Novel approaches for statistical characterization, such as through in situ detectors which provides a large collecting area or with space-based optical sensors, are being studied.

1.4 Impact Hazard and Protection

Consequences of impacts on satellites can range from small surface pits from micrometer-size objects, via clear-hole penetrations from mm-size objects, to mission-critical damage from projectiles larger than a centimeter (figure 1.9). The destructive energy is a consequence of the high impact speeds, which can reach more than 15 km/s. Assessing the risk that space debris affect to operational satellites and spacecraft is quite difficult and depends on many factors. The most important one is the risk of being hit by a tracked and well-known object or by an unknown one.
Nowadays tracked space debris is bigger than 5-10 cm and represents a huge deal, since a direct impact would means a deadly event, but the deep knowledge of their positions and path allow to carry out successfully collision avoidance maneuvers. However, assessing the risk due to smaller debris objects and meteoroids is an entirely different matter, as these are difficult or impossible to track.
Smaller debris could range from microscopic particles of dust, which are quite harmless, up to objects about 1 cm in diameter, that represents a real threat. In order to survive impact, protective shielding technology is used quite successfully but only for certain type of mission, such as in the International Space Station.
Objects from 1 to 10 cm in diameter are the real threat, they are numerous, hardly traceable and a single hit could cause a total loss of the mission.

Figure 1.9: 1.2 cm diameter sphere of aluminum at 6.8 km/s and a block of aluminum 18 cm thick

Orbital debris protection involves conducting hypervelocity impact tests to assess the risk presented by orbital debris to operating spacecraft and developing new materials and new designs to provide better protection from orbital debris with less weight penalty. The primary facility for this research is the Hyper-velocity *Impact Technology Facility (HITF)* at the Johnson Space Center in Houston. One of the main project conducted for testing hyper-velocity impact is *DebriSat* (figure 1.10), a collaboration the NASA Orbital Debris Program Office (ODPO), the Air Force Space and Missile Systems Center (SMC), The Aerospace Corporation (Aerospace), the University of Florida, and the Air Force Arnold Engineering Development Complex (AEDC). A 56 kg sacrificial satellite, that could effectively represents modern payloads in LEO environment, that is voluntarily hit by a hyper-velocity projectile to break it up and collect all the fragments, get useful data on fragments properties to increase space situational awareness and satellite breakup models.

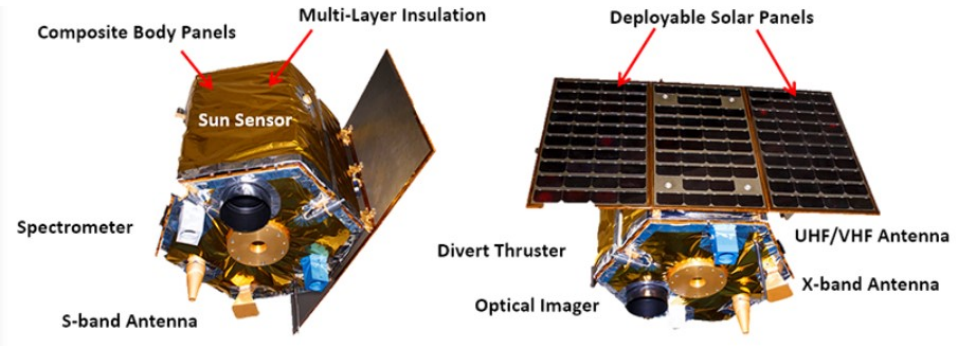

Figure 1.10: Picture of the DebriSat satellite

One of the main purpose of Hypervelociy Impact testing is the development of new shielding technology to protect spacecraft on orbit. The greatest part of development activities are focused on the support of the ISS surfaces, constantly hit by space debris and meteoroids. The aim of these projects is to build up shield that are effective, while being lightweight. Here follows a brief description of some existing shielding technology (figure 1.11):

- **Monolithic**: this type of shield represents a brute force approach, that's a simple slab of thick aluminum. It's very heavy and not efficient but it can be used as a "default shielding" against meteoroid and debris.
- **Whipple**: first shield ever implemented on a spacecraft. It consist of a sacrificial aluminum bumper in front of the spacecraft that absorb the initial impact. The whipple bumper splits up the projectile and creates a debris cloud of smaller pieces, less dangerous, that exert a full force on a greater area on the rear wall.
- **Stuffed Whipple**: is a variation of the whipple shield. Some layers of Kevlar and Nextel are inserted between the bumper and the rear wall. In this way it's possible to obtain a more effective pulverization of the projectile.
- **Multi-Shock**: is a popular shielding design. it consists of staggering layers of Nextel at a precise distance from each other. The layers split up the projectile multiple times to get a perfect pulverization.
- **Mesh Double Bumper**: consists of a double layer of aluminum mesh, followed by an aluminum rear wall.
- **Honeycomb Panel**: consists in two aluminum panel filled with an honeycomb aluminum structure, creating a sandwich panel. These panels are evaluated for their micrometeoroids and orbital debris (MMOD) shielding capacities.
- **Foam Panel**: metallic foam sandwich panels provide structural support similar to honeycomb but have better MMOD shielding capabilities.
- **Transhab**: the Mars Module Shield is a prototype developed for a future manned mission to Mars. This shield consists of layers of Mylar, Nextel, Kevlar and foam (in order to reduce mass). The foam design is used to get a compressible design for launch.

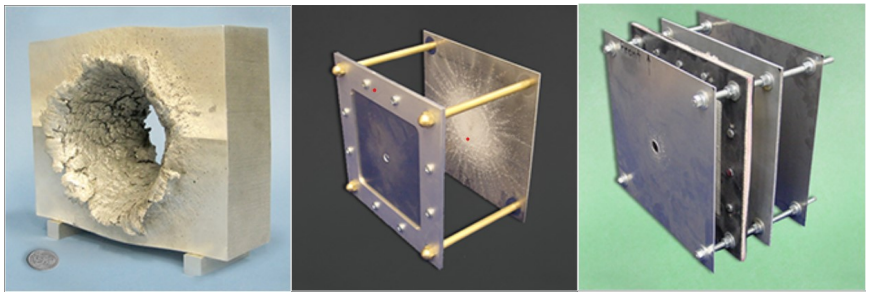

(a) *Monolithic shield* (b) *Whipple shield* (c) *Stuffed whipple shield*

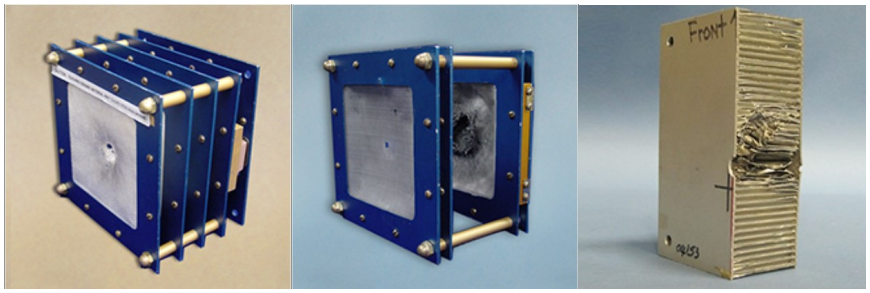

(d) *Multi shock shield* (e) *Mesh double bumper shield* (f) *honeycomb panel*

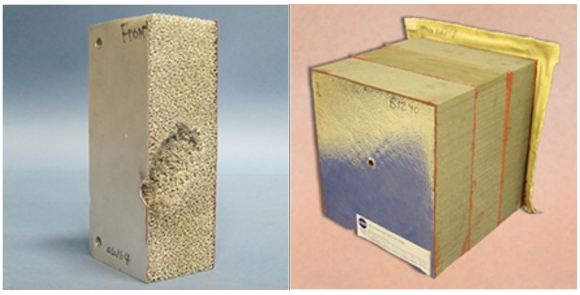

(g) *Foam panel* (h) *Transhab*

Figure 1.11: Different type of shields

In order to assess risk in the deadly 1 to 10 cm diameter debris impact, sophisticated probability models and software are used. Risk is predicted based on spacecraft cross-section area, its orbital attitude and flight path, the assumed size of debris and relative speed. For example, for a satellite with a 100 m^2 cross-sectional area (including solar panels) orbiting at 400 km altitude, the mean time between impact with a debris object 10 cm in size has been calculated to be on the order of 15 000 years.

1.5 Debris Mitigation

Controlling the growth of the orbital debris population is a high priority for all Space Agencies of the world in order to preserve near-Earth space for future generations. With today's rate of more than 100 launches per year and assuming future break-up will continue at mean historical rates of four to five per year, the number of space debris will increase steadily (figure 1.12). As a consequence of this trend, the probability of catastrophic collision will also grow.
Collision Fragments can trigger further collisions, leading to a self-sustain cascading process known as "Kessler Syndrome", a NASA space debris expert who observed that, once past a certain critical mass, the total amount of space debris will keep on increasing: collisions give rise to more debris creation that leads to more collisions, in a chain reaction. it's now clear that reduce the total mass of current debris is essential.
The most recognized debris mitigation measures can be summarized as follows:

- *The limitation of space debris released during normal operations*: all operational satellites, payloads and rocket should be designed to minimize released space debris, in order to prevent the Kessler syndrome, not only in number but even in occupied are and mass.

- *The minimization of the potential for on-orbit break-ups*: all operative satellite should be designed to reduce the probability of break-ups that can cause a total loss of the system. This can be conducted through a better analysis of the failure trees, an increase subsystem reliability, a minimization of the potential for post-mission break-ups and avoiding intentional destruction of the spacecraft.

- *Prevention of on-orbit collisions*: in developing the design and mission profile of a space object, a project should estimate and limit the probability of accidental collision with known objects the orbital lifetime.

- *Post mission disposal*: payloads and rocket bodies that are terminating their operational phases should be maneuvered to reduce their orbital lifetime or relocated to unused orbits. This practice could leads to a quite successful reduction of the Kessler syndrome, restraining number of possible fragments.

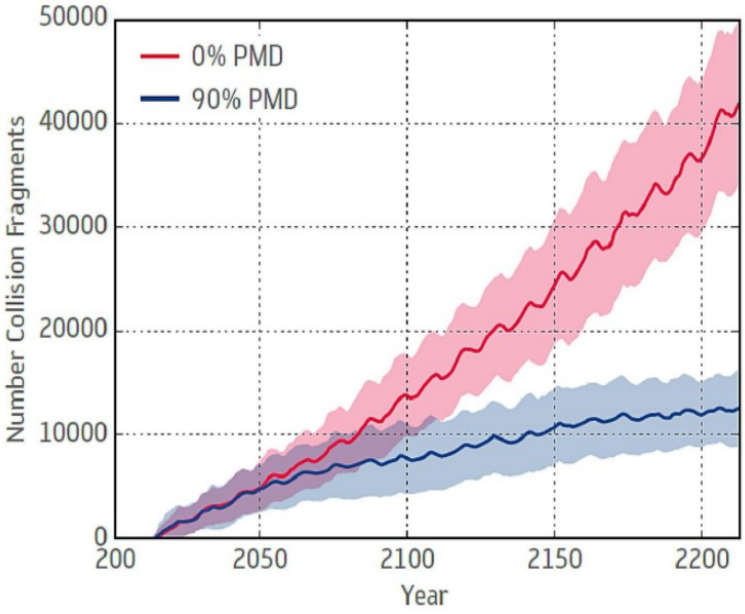

Figure 1.12: Evolution of objects larger than 10 cm in LEO, depending to the adherence to PDM guidelines

1.6 Active Debris Removal

Mitigation measures alone are not enough to fight the problem effectively, even with a full mitigation compliance and even if all launches activities are halted, a long-term proliferation of space debris would still be expected. This is an indication that the great presence of massive debris has already reached a critical concentration in LEO. *Active Debris Removal*, alongside mitigation measures, could be the only solution to reduce successfully the space debris population. Studies at NASA and ESA show that, with a removal strategy focusing on large target masses, the environment can be stabilized if about five to ten objects are removed from LEO per year with the following priorities:

- objects with a high mass
- objects with a high collision probability
- objects at high altitudes where atmospheric drag is very low

Long-term simulations can be used to analyses orbital regions that are hot-spots for collisions, finding that these regions are at around:

- 1000 km altitude and 82° inclination

- 800 km altitude and 98° inclination
- 850 km altitude and 71° inclination

The concentration of critical-size objects in these narrow orbital bands could allow multi-target removal missions.

1.7 Active Missions

In this section will be described some Active Debris Removal missions that has be presented in the past years.

1.7.1 e.Deorbit

This project was born in order to take down a single dead satellite and then redesigned for a wider role as a new space servicing vehicle to perform different roles in orbit, such as refueling, refurbishing or reboosting of satellites already in orbit. ESA's Clean Space initiative began developing the mission (figure 1.13) in 2013 to de-orbit the Envisat Earth-observing satellite, which broke unexpectedly after 10 years of in-orbit operations.

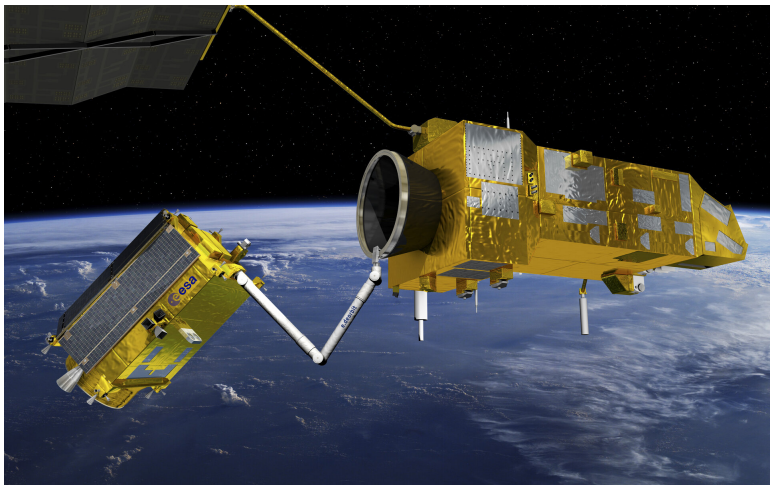

Figure 1.13: Illustration of e.Deorbit

Scientist began to work on a possible capture system, from a robotic arm to nets or even a harpoon, and the development of an high accuracy guidance navigation and control system to safely get closer to the target. After few years of studies, ESA decided to widen the scope of the mission, creating a "Swiss Army Knife" of a satellite with the agility, capability and autonomy to perform all kinds of complex tasks in space.

1.7.2 NASA's Restore-L mission

NASA's Restore-L mission (figure 1.14) concerns a robotic spacecraft able to refuel an operational satellite in LEO. The first of it's kind, it will demonstrate the feasibility of autonomous satellite rendezvous and grasping, in order to dramatically reduce or eliminate the need for crewed servicing flights from Earth. The first attempt will be in 2020 and the current candidate client to be refueled is Landsat-7, a government-owned satellite in LEO.

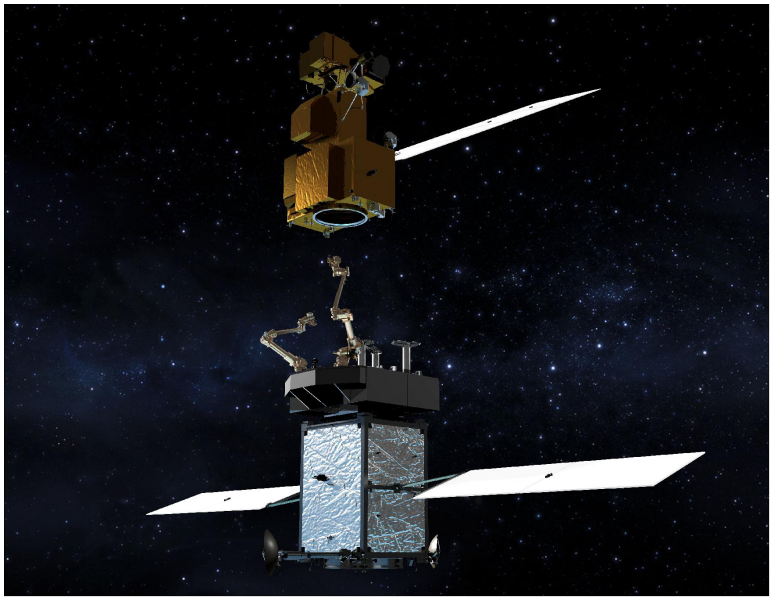

Figure 1.14: illustration of NASA's Restore-L mission

1.7.3 DARPA's RSGS

The aim of *Robotic Servicing of Geosynchronous Satellites*(RSGS) (figure 1.15) is to demonstrate the feasibility of a robotic servicing vehicle that can perform safely in GEO and support the development of a service spacecraft able to complete dozen of missions over several years. This could be done only with a robust spacecraft that can store a huge amount of propellant. The capabilities that RSGS aims to make possible include:

- High-resolution inspection
- Correction of some types of mechanical anomalies
- Assistance with relocation and other orbital maneuvers

- Installation of attachable payloads, enabling upgrades or entirely new capabilities for existing assets
- Refueling

Figure 1.15: illustration of RSGS

2 Electrostatic Propulsion

2.1 introduction

Since the purpose of the study regards low-thrust maneuver, a brief description of electrical thruster must be conducted. Propulsion is based on the action-reaction law. Assuming an isolated system, momentum is conserved and cannot be exchanged. Space is empty and represents an isolated system, in order to exchange momentum a means (propellant) is required, which represents a huge limitation. To exchange momentum, propellant must be energized chemically or electrically.
Assuming an isolated system with no external forces and considering a spacecraft at time t0, velocity V and mass m (figure 2.1):

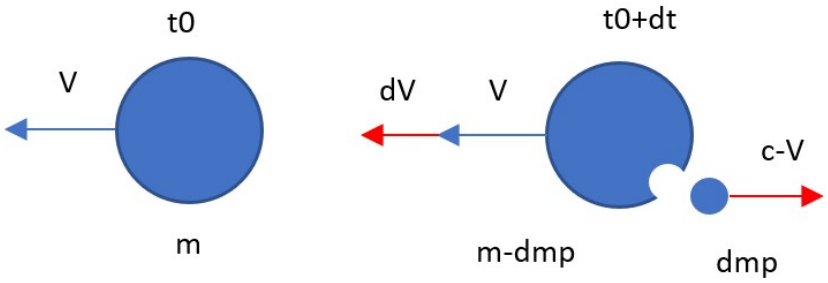

Figure 2.1: Momentum exchange

after a time dt the spacecraft have lost a small fraction of propellant, accelerated in the opposite direction of motion at "c-V" speed, where c is the propellant velocity relative to the reference system. Applying the conservation of momentum and assuming a continuous emission of propellant, thrust produced can be written as:

$$T = \dot{m}_{\mathrm{p}} c \tag{2.1}$$

For electrical propulsion a power is needed to accelerate the propellant, so it's necessary to define:

$$P_{\mathrm{T}} = \dot{m}_{\mathrm{p}} c^2/2 \tag{2.2}$$

When propellant comes out from the nozzle, it is not considered anymore part of the system and starts exerting a pressure force on the propellant inside the system (figure 2.2).

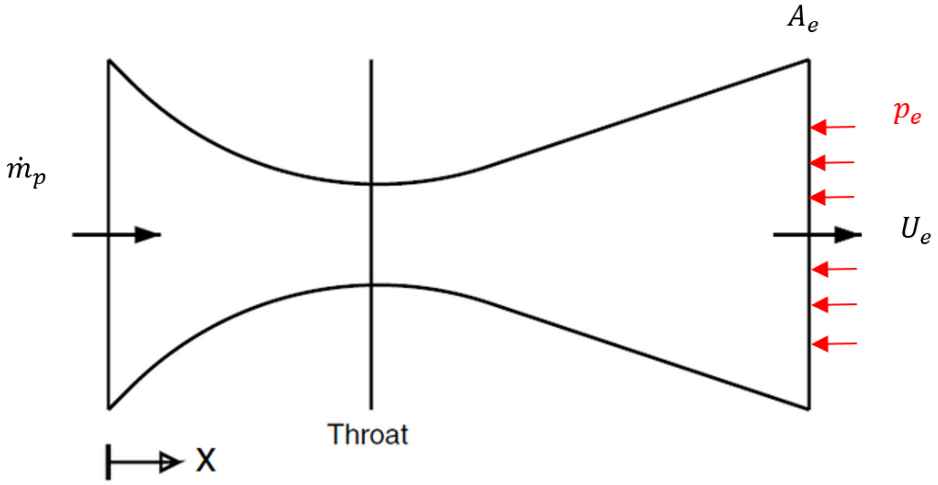

Figure 2.2: Nozzle

Thrust must be rewritten as the sum of a static component and a dynamic component:

$$T = \dot{m}_{\mathrm{p}} U_{\mathrm{e}} + A_{\mathrm{e}}(p_{\mathrm{e}} - p_0) \tag{2.3}$$

For simplicity, a single term could be defined to take into account the static thrust, the *effective exhaust velocity* "c" defined as:

$$c = T/\dot{m}_{\mathrm{p}} = (\dot{m}_{\mathrm{p}} U_{\mathrm{e}} + A_{\mathrm{e}}(p_{\mathrm{e}} - p_0))/\dot{m}_{\mathrm{p}} \tag{2.4}$$

it's useful to introduce the definition of total impulse, total propellant mass and specific impulse as:

$$I_{\mathrm{t}} = \int_{t_0}^{t_{\mathrm{f}}} T\, dt \tag{2.5}$$

$$m_{\mathrm{p}} = \int_{t_0}^{t_{\mathrm{f}}} \dot{m}_{\mathrm{p}}\, dt \tag{2.6}$$

$$I_{\mathrm{sp}} = I_{\mathrm{t}}/m_{\mathrm{p}} g_0 \tag{2.7}$$

Assuming m_p,T,c constant during the entire maneuver, I_{sp} could be rewritten as:

$$I_{\mathrm{sp}} = c/g_0 \tag{2.8}$$

Specific Impulse represents the utilization efficiency of the propellant and the time, in seconds , that our system could produce self-sustaining thrust. The engine must provide the correct ΔV in order to successfully de-orbit a specific debris. There are multiple possible solution for the engine design, but

basically the choice would be between *Chemical Propulsion* and *Electrical Propulsion*.

- **Chemical Propulsion**: Fuel and oxidizer are pumped inside tha combustion chamber where chemical energy (E_{ch}) is produced through combustion. Thermal energy is converted into kinetics energy thanks to the convergent-divergent nozzle, producing thrust (figure 2.3).

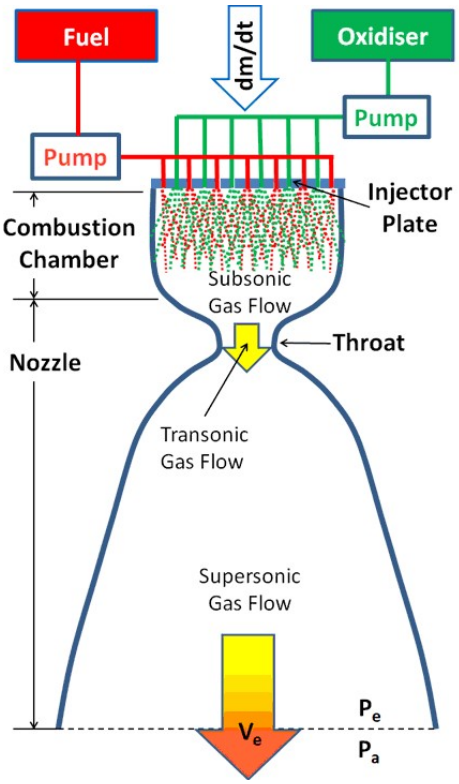

Figure 2.3: schematic of chemical propulsion

Through the energy balance, assuming that energy is preserved during the expansion inside the nozzle, it's possible to define the effective exhaust velocity as:

$$c = \sqrt{2}E_{\text{ch}} \tag{2.9}$$

Assuming that chemical energy is defined by what type of propellant is used, exhaust velocity is limited and consequently the specific impulse will be very low. Follows some examples (table 2.1):

Table 2.1: Different type of propellants

Propellants	State	Specific Impulse [s]
LOX/LH2	L	400-450
LOX/RP-1	L	300-330
LOX/CH4	L	280-310
NTO/Hydrazine	L	280-310
NTO/MMH	L	280-310
NC/NG	S	200-250
AP/PBAN/Al	S	260-290

The main advantages of chemical propulsion are a great value of thrust produced and the lack of need for any means to energize. For this project purposes, chemical propulsion provides the correct value of ΔV through an impulsive maneuver in order to reduce the perigee to r_p*. The deorbiting maneuver could be done in two different ways: a *controlled re-entry*, where the modify orbit must intersect the Earth surface, (r_p*=rE) and a *uncontrolled re-entry*, where the debris is inserted in a very low orbit (r_p*=1.02rE) to let atmospheric drag destroying it. The required velocity change can be evaluated as follow:

$$\Delta V = \sqrt{\mu/r_a} - \sqrt{2\mu(1/r_a - 1/(r_a + r_p^*))} \tag{2.10}$$

- **Electrical Propulsion**: The propellant goes through the engine and an electrical power, get from an external source, energizes it (figure 2.4).

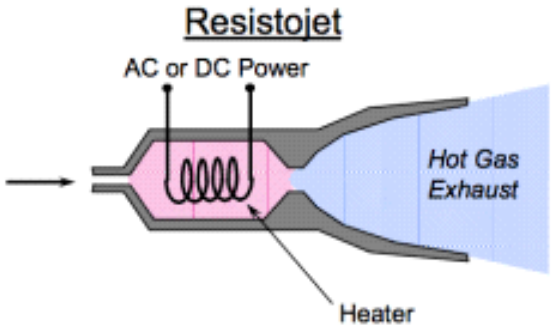

Figure 2.4: schematic of electrical propulsion

Thrust power for an electric engine could be written as:

$$P_{\mathrm{t}} = \eta P_{\mathrm{e}} = Tc/2 \tag{2.11}$$

consequently it's necessary to define the effective exhaust velocity:

$$c = 2\eta P_{\mathrm{e}}/T \tag{2.12}$$

High exhaust velocity and specific impulse could be obtained through great power or little thrust produced. Since the external power source mass depends on power produced, accept quite small thrust is preferred. On one side, unlike chemical propulsion, high specific impulse could be reached, even ten times greater, consuming less fuel, on the other impulsive maneuvers could not be performed, leading to greater missions time and losses.
Due to the low thrust generated by the thrusters, the orbit shape is modified gradually until the debris enters the atmosphere. Only an uncontrolled re-entry is allowed. The required velocity change could be evaluated through Edelbaum's approximation, assuming almost circular orbits:

$$\Delta V = \sqrt{\mu/r_{\mathrm{p}}^*} - \sqrt{\mu/a} \tag{2.13}$$

For this project, Electrical Propulsion has been chosen due to it's low fuel consumption and kit mass.

2.2 Electrical Propulsion

Electrical propulsion produces thrust through a gas accelerations using an external power source to energize it. Here follows a brief description of the main categories of electrical engines:

- **Electrothermic Propulsion**: propellant is heated through an external power source and then accelerated in a nozzle. Resitojet and Arcjet are the main electrothermal engines.
- **Electrostatic Propulsion**: propellant is ionized inside the engine and then accelerated through an electric field. Ion thrusters and Hall thrusters are the main electrostatic engines.
- **Electromagnetic Propulsion**: propellant is ionized inside the engine and then accelerated through an electromagnetic field. MPD, PPT and VASMIR are the main electromagnetic engines.

2.3 Ion Thrusters

In order to overtake limitations on specific impulse of Electrothermal propulsion, it's necessary to not heat the propellant but use the direct acceleration of charged particles to generate thrust. To achieve an effectively functioning there are some necessary requirements:

- *Ionization*: ions are generated and separated from electrons in order to get a resulting force different from zero.
- *Acceleration*: ions are accelerated by a strong electric field, generated inside the thruster.
- *Neutralization*: the ion beam coming out of the engine must be neutralized by an electron stream, otherwise the spacecraft would charge negatively and ions would be attracted back inside the thruster.

2.3.1 Ionization

Before gets into the ionization process, it's necessary to define how the ion thruster is composed (figure 2.5).

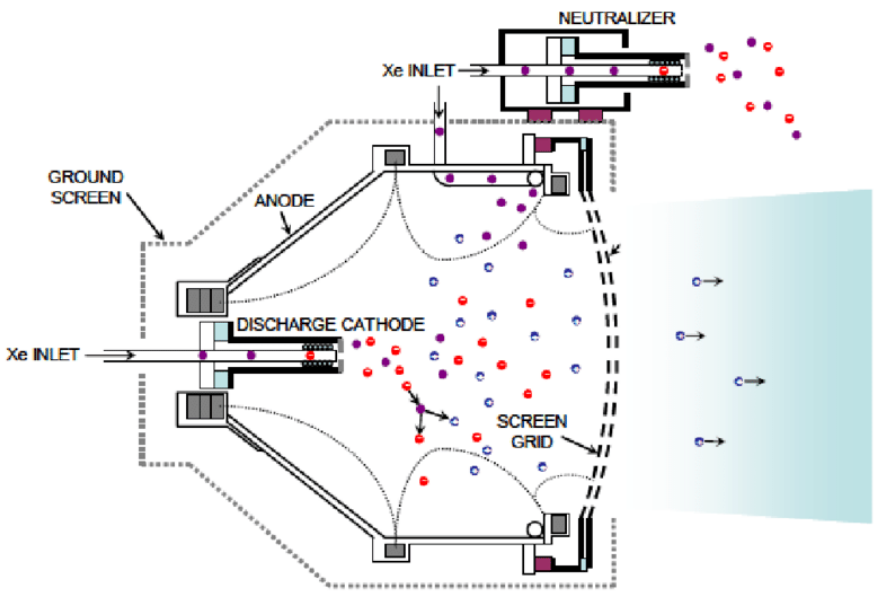

Figure 2.5: Schematic of a ion thruster

The thruster is composed by: a main chamber where the ionization takes place, a discharge cathode and an anode to create the electron stream inside the chamber, injectors at the base of the engine where propellant is injected, an external cathode for the neutralization of the ion beam and, finally, a screen grid and an acceleration grid to accelerate ions. There are two different strategies to accomplish the ionization:

- **Electron Bombardment**: high energy electron emitted by the discharge cathode, at the base of the engine, that moves towards the anode. Along the way to the anode there is a probability of hitting an atom of propellant, injected in the main chamber, and ionize it.
- **Radio Frequency Ionization**: free electrons are accelerated by electromagnetic waves, generated by an antenna, that collide with neutral atoms of propellant.

Each ionized atom will produce an ion and an electron. A certain quantity of energy has been spent to accelerate each electrons, but not all of them will ionize an atom, so it's possible to define a cost of production for a single ion, ϵ_b, energy that represents a loss. The ideal efficiency of ionization process coul be defined as:

$$\eta_{in} = 1/(1 + (2\epsilon_b/m_+ u_+^2)) \tag{2.14}$$

The value of η_{in} will be high if a proper propellant is chosen, one with a high atomic mass, velocity and with a low cost of ionization. On one side a proper value of m_+ and ϵ_b could be chosen based on the propellant choice, on the other u_+ is linked to the specific impulse I_{sp} and could not be decided freely. In conclusion ion thruster is suited only for high specific impulse missions. Follows a comparison of some propellant used in ion thrusters (table 2.2): In

Table 2.2: Comparison of different type of propellants

Propellant	Cs	Hg	Xe	Kr	Ar
M	132.9	200.6	131.3	83.8	39.9
m, 10^{-25} kg	2.21	3.33	2.18	1.39	0.66
q/m, 10^5 C/kg	7.25	4.80	7.34	11.50	24.13
ϵ_i, eV	3.89	10.44	12.13	14.00	15.80
ϵ_i/m, Mj/kg	2.82	5.02	8.90	16.12	38.30
Notes	toxic	toxic			

addition of the electrical field, a magnetic field in the axial direction helps

to confine the electrons in the main chamber in order to increase residence time and the collision probability with a neutral propellant atom, leading to a ϵ_b reduction. Electrons, along the way towards the anode, will start a circular motion around the engine axis in ExB direction (figure 2.6). In

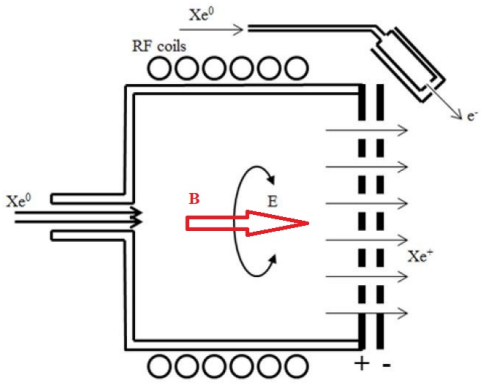

Figure 2.6: Magnetic and Electrostatic field direction

order to maintain the circular motion around the engine axis, the probability of collision between electrons must be reduce, since after a collision electrons velocity and consequently the magnetic force upon them is inhibited, in favor of the electrical force that pushes electrons towards the anode. Choosing the right potential between the anode and the cathode is essential, it must be over the first ionization potential (12.13eV) and high enough to get a good confinement. A value of 30ev it's acceptable (figure 2.7).

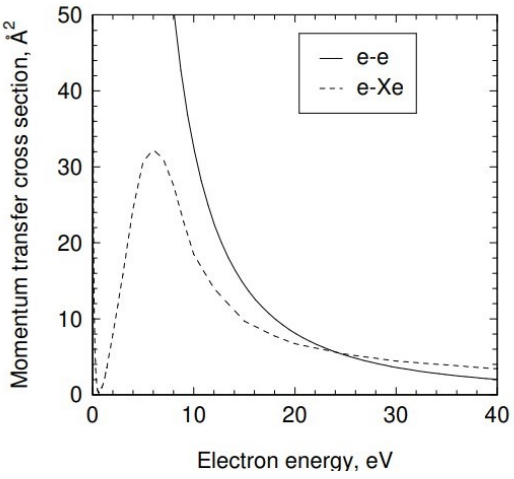

Figure 2.7: Cross section over Electron energy

2.3.2 Acceleration

Once ions have been generated, they are attracted inside two grids where the acceleration takes place, due to an applied potential difference. Assuming a constant value of electrical field between the two grids, an ion that gets inside the acceleration chamber has, on one side the beneficial effect of the electrical field that pushes it forward and, on the other side, the presence of others ions ahead exerts on it a repulsion force that pushes it back. Reached a certain ions density, the resulting force became zero and the thruster chokes, the *maximum current* is reached. This behavior causes a limitation on the maximum quantity of ions per area unit inside the acceleration chamber and consequently a maximum thrust production.
In order to define the amount of maximum thrust production, assuming a 1D problem, a constant electrical field between the two grids and the potential of the acceleration grid equal to zero, the *Child's law* allows to find the potential distribution between the two grids (figure 2.8).

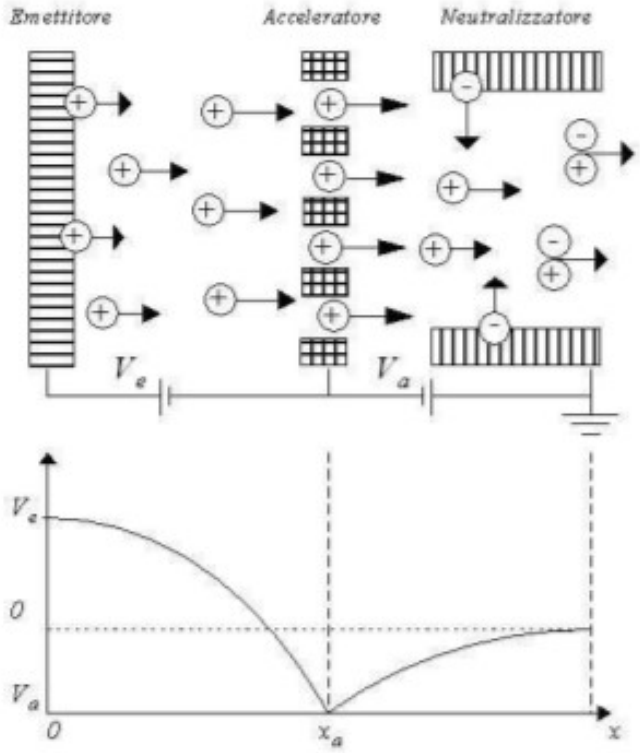

Figure 2.8: Potential trend between grids

Once the potential trend has been defined, the maximum current can be written as:

$$j_{\max} = (4\epsilon_0/9)(2q/m_+)^{1/2}(V_g^{3/2}/x_a^2) \tag{2.15}$$

where:

- $\epsilon_0 = 8.85418 * 10^{-12}$ is the vacuum permittivity
- q is the ion electric charge
- m $_+$ is the ion mass
- V_g is the screen grid potential
- x_a is the distance between the two grids

Consequently the maximum thrust per area unit colud be written as:

$$T/A = (4\epsilon_0/9)(2m_+/q)^{1/2}(V_g^{3/2}/x_a^2)c \tag{2.16}$$

There is a direct dependence on the effective velocity c, increasing this value allows to raise T/A, but the effective velocity could not be chosen freely, since there is an optimal specific impulse for each mission. At the same time c is linked to V_g and the same problem would rise again.
A possible solution is represented by *Acceleration-Deceleration concept* where the acceleration grid is charged negatively causing a region, just before the second grid, where ions decelerate (figure 2.9).

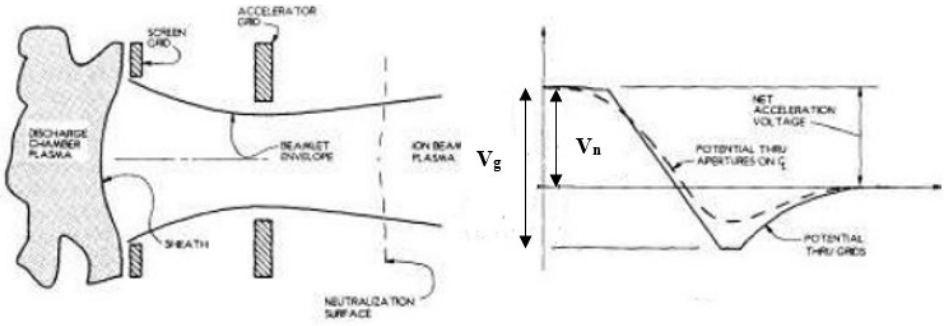

Figure 2.9: Acceleration-Deceleration concept

Using this concept, V_g and c have been successfully decoupled and now exhaust velocity can be rewritten as:

$$u_+ = \sqrt{(2q/m_+)V_n} \tag{2.17}$$

where V_n is the new screen grid potential. Now V_g can be increased to rise the thrust production and the maximum current while V_n value defined the effective velocity. Another beneficial effect is represented by the repulsive effect that the acceleration grid exerts to electrons, out of the engine, used to neutralize the ions beam avoiding an unwanted re-entry.
In addition to the acceleration process, grids carry out another fundamental task, *reduction of the ions beam divergence* that is crucial for avoiding thrust loss. The beam inside grids is composed mainly by ions, charged positively, that exert repulsive action among them causing a divergence of the beam (figure 2.10).

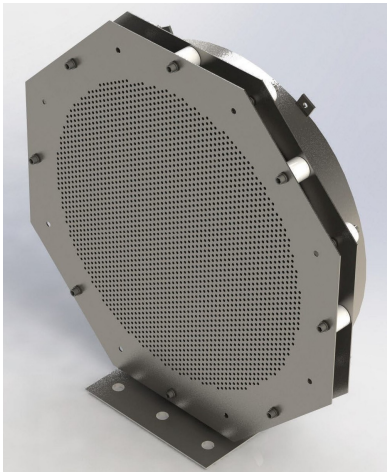

Figure 2.10: Gridded Ion Thruster

Creating multiple holes on the grid allows to isolate each ions beam to the others, thanks to the accumulation of electrons on the grid. Due to an ions sheaths that forms just before the screen grid, the ions beam first converge and then diverge after the screen grid, obtaining an acceptable degree of divergence outside the engine (figure 2.11).

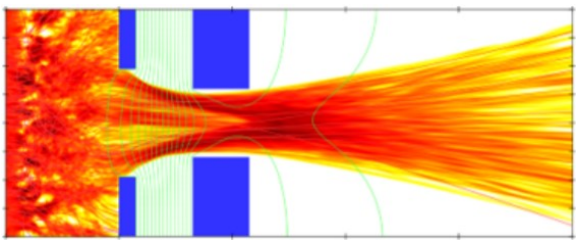

Figure 2.11: Ions beam divergence

2.3.3 Neutralization

Once ions have been accelerated through the two grids, negative charge of the spacecraft start increasing and ions start to be attracted back inside the engine or on a spacecraft surface. In order to avoid this process, at a certain distance form the engine exit, an electrons beam must be used to neutralize ions. The neutralization must be done before a well defined distance to avoid an ions back-stream, exactly $2\sqrt{2}$ times x_a starting from the acceleration grid. In conclusion the neutralization should be done close to the exit but an emitter located just ahead of the grid would be seriously damaged. The solution is represented by an *Hollow Cathode* (figure 2.12).

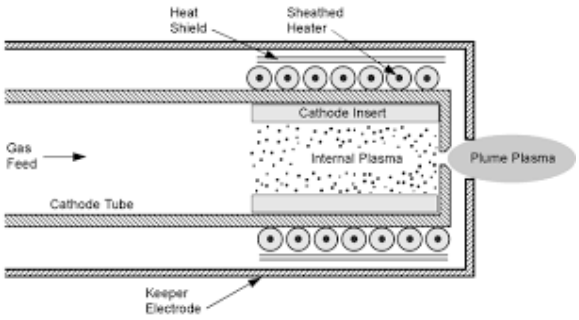

Figure 2.12: Schematic of an Hollow Cathode

A small fraction of propellant passes through the cathode, where an insert is heated in order to activate the *Thermoionic emission* and to liberate electrons, that will collide with the neutral atoms of propellant ionizing them. A plasma of electrons and ions comes out from the cathode exit and is accelerated by a small potential difference. Since the propellant injected in the Hollow Cathode does not produce thrust, it represents a loss.

2.3.4 Performance

Since in this paper a real system is presented, it's necessary to define a global efficiency of the system and losses. First of all an incomplete ionization and the hollow cathode loss should be introduced:

$$\dot{m_p} = \dot{m_+} + \dot{m_a} \tag{2.18}$$

where $\dot{m_+}$ represents ions flow and $\dot{m_a}$ represents the flow of not ionized atoms, escaped from the engine, combined with the propellant flow injected inside the hollow cathode. An *utilization efficiency* is defined as:

$$\eta_u = \dot{m_+}/\dot{m_p} \tag{2.19}$$

Electrical efficiency, η_{el}, include ionization cost and electrical losses. *Global efficiency* could be defined as:

$$\eta_{\text{g}} = \eta_{\text{u}}\eta_{\text{el}} \tag{2.20}$$

There are two ways to improve the global efficiency:

- increasing the propellant mass flow leads to a ionization cost reduction but the amount of atoms that escapes increases and η_{u} decreases. Free neutral atoms inside the accelerations chamber are dangerous since could exchange charge with ions and then hit grids, damaging them.
- increasing the electrons current leads to a density reduction inside the ionization chamber and a consequently better ionization. η_{u} increase but there si a probability of double ionization, dangerous for possible high energy impact on grids.

The performance of this type of thruster could be summarize as follows (table 2.3):

Table 2.3: ion thruster performance

Power	$\mathbf{I_{sp}}$	**Thrust**	**Diameter**
1 to 5 KW	2500 to 5000 s	0.01 to 0.2 N	10 to 30 cm

Some examples of existing ion thrusters are listed below (table 2.4 and figure 2.13).

Table 2.4: Ion thrusters

Name	**P**[kW]	$\mathbf{I_{sp}}$[s]	**T**[N]	η	**D**[cm]
XIPS 13	0.33	2570	18	0.7	13
XIPS 25	4.5	3800	165	0.7	25
NSTAR	0.5-2.3	3100	20-95	0.63	30
RITA 15	0.5	5000	15		10
RITA 150	4.3	5000	150		22
T5	0.27-0.65	3500	10-25	0.65	10
T6	5.2	3500	40-200		22

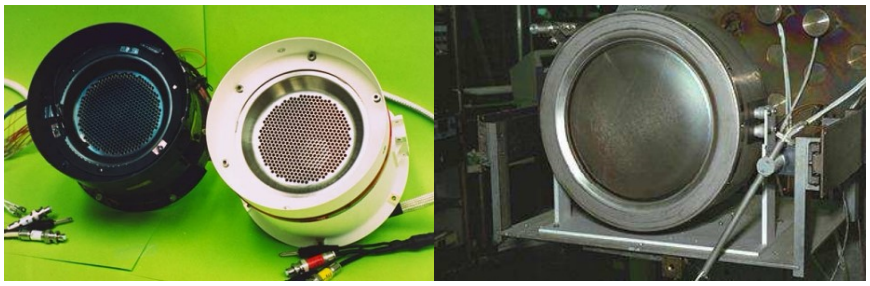

(a) *RITA 15,T5* (b) *NSTAR*

Figure 2.13: Picture of existing ion thrusters

2.3.5 Key issues

Here follows a list of issues that regards ions thrusters:

- Presence of magnetic filed to improve confinement, maximum intensity near walls (10T)
- Doubly charged ions that could seriously damage grids on impact
- Charge-exchange between atoms and ions inside tha acceleration chamber that could strike grids and cause erosion
- Ions thrusters are made by stainless steel for the discharge chamber and molybdenum for grids

2.4 Hall Thrusters

Due to Child's law, in ion thrusters, there is a maximum current/thrust density. In Hall thrusters this limitation is overtaken, accelerating not only ions but even electrons. Compared to ion thrusters, ionization and acceleration now happen in the same chamber.

2.4.1 Particles Motion

In order to avoid that the resulting force is zero, a magnetic field is used (figure 2.14).

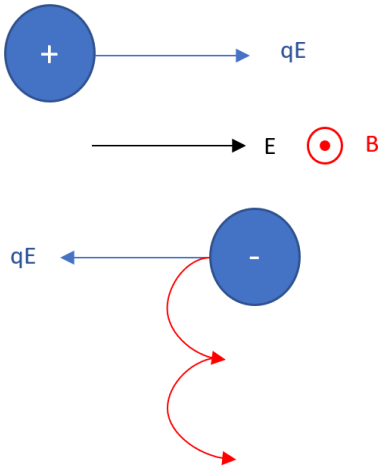

Figure 2.14: Particles motion

Charged particles in motion in electric and magnetic field have a particular behavior, while electric field accelerates charged particles, magnetic field exerts a force, perpendicular to the direction of velocity, that tends to change the trajectory. The result of this forces leads to a *cycloidal motion* that could be visualized as follows (figure 2.15):

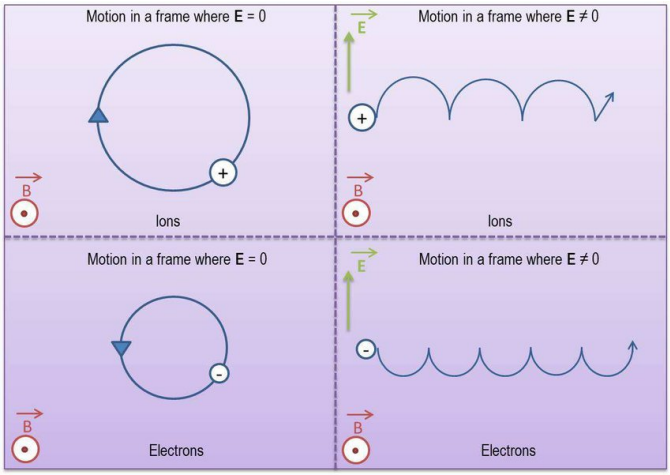

Figure 2.15: Particles motion in electric and magnetic field

Taking into account even particles collisions, each time an electron collides it stops and, since magnetic force depends on velocity, electric force becomes preponderant and cycloidal motion is inhibited. Introducing ω_B as cycloidal frequency and γ_c as collisions frequency, the *Hall parameter* could be defined

as:

$$\Omega = \omega_B/\gamma_c \tag{2.21}$$

when:

- $\Omega << 1$: high collision frequencies inhibits cycloidal motion and electrons move towards the electrical field direction
- $\Omega >> 1$: low collision frequencies emphasizes cycloidal motion and electrons move towards ExB direction

In hall thrusters electrons must be confined inside the chamber with a cycloidal motion around the engine axes in order to guarantee a good level of ionization, through electron bombardment, and to cut out maximum density of ions. To obtain this result it's necessary to guarantee two conditions:

- $\mathbf{r_{B+} \gg d \gg r_{B-}}$: since even ions are influenced by electric and magnetic field, to produce thrust ions must not be influenced too much by them and the cycloidal radius must be greater than the engine characteristic dimension. Whereas, electrons must be confined inside the engine so the cycloidal radius must be small enough.
- $\Omega >> 1$: since electrons must be confined inside the engine chamber, cycloidal motion must not be inhibited by collisions

2.4.2 Functioning

Here follows a visualization of the Hall thruster annular structure (figure 2.16):

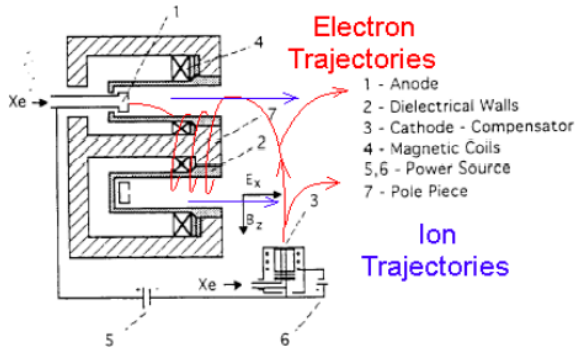

Figure 2.16: Schematic of an Hall thruster

The engine has a annular structure, with the anode located at the base and the hollow cathode external to the engine. Propellant is injected from the base and gets ionized by electrons bombardment. Electric field is directed towards the engine axis, whereas magnetic field is perpendicular to the electric field.
The functioning of this type of thruster is dictated by electrons emitted by the external cathode, that are divided into two beams: one that gets confined into the engine and one used to neutralized the ions beam coming out of the engine. Electrons attracted inside the engine finds a strong magnetic field which obliges them to rotate around the engine axis. Here Ω has a great value, like 100, so electrons make a lot of cycloids before a collision with a neutral atom of propellant. Each time electrons collide, they get a little closer to the anode. Since *medium free path* of the propellant, assuming Xeno as propellant, is in the order of a millimeter and the engine chamber is usually longer than 1cm, propellant ionization is almost complete.
There are two main types of Hall thrusters (figure 2.17):

- **Magnetic Layer**: made with insulating walls with the maximum value of magnetic field inside the engine main chamber. Acceleration zone is quite long, in the order of a centimeter.
- **Anode Layer**: made with conductive walls that amplify the electric field with the maximum value of the magnetic filed external to the engine. Acceleration zone is very short, in the order of a millimeter.

(a) *PPS 1350 (Magnetic Layer)* (b) *TM-50 (Anode Layer)*

Figure 2.17: Picture of existing Hall thrusters

2.4.3 Performance

As it has been done for the ion thruster, a global efficiency for Hall thrusters is defined. In this case, electrons and ions are accelerated together so not all the potential is used by ions, just a fraction. Ions exhaust velocity can be written as:

$$u_+ = \sqrt{2fqV_\mathrm{D}/m_+} \tag{2.22}$$

where f is the potential fraction used by ions. Since ionization process is almost complete, utilization efficiency, η_u, is near 1. Whereas, electrical efficiency could be written as:

$$\eta_\mathrm{el} = f/(1 + J_\mathrm{E}/J_+) \tag{2.23}$$

where $\mathrm{J_E}$ represents electrons current and $\mathrm{J_+}$ represents ions current.
Global efficiency rise as the specific impulse and potential increases, but, unlike ion thrusters, with quite low specific impulse, global efficiency value is acceptable. Hall thrusters can be used for mission with specific impulse lower than 2500s with similar performances of ion thrusters. Performances could be summarized as follows (table 2.5):

Table 2.5: Hall thrusters performance

Power	$\mathbf{I_{sp}}$	η	$\mathbf{V_D}$
0.3 to 10 KW	1500 to 2500 s	0.5-0.7	200-600

2.4.4 Key issues

Here follows a list of issues that regards Hall thrusters:

- Plasma non-uniformity causes electrical field fluctuations and electromagnetic interference generations that leads to walls erosion
- Magnetic field profile along the main chamber must be well calculated for stable operation and to limit erosion
- Ions lost to wall
- Presence of doubly charged ions
- The absence of grids causes great divergence of the beam
- Generation of azimuthal momentum due to Larmor motion

2.5 Comparison

In conclusion it's showed a table of comparison between ions thrusters and Hall thrusters (table 2.6):

Table 2.6: Comparison Table

Type	**Hall**	**Ion**
propellant	Xe	Xe
Isp[s]	1500-2500	2000-4000
PE[W]	300-10000	200-5000
η	0.5	0.65
voltage[V]	200-600	1000-2000
thruster mass[kg/kW]	2-3	3-6
PPU mass[kg/kW]	6-10	6-10
feed system	regulated	regulated
lifetime[h]	> 7000	> 10000
missions	SK	SK
	Orbit transfer	Orbit transfer
	Medium ΔV	Large ΔV

3 Mathematical Models

3.1 Fundamentals of Astrodynamics

Before the study of *Edelbaum's theory*, an introduction to astrodynamic concepts is necessary to fully undertsand the purpose of this study.

3.1.1 Orbital elements

Thank to the solution of the *two-body problem*, it has been found that the orbit of a body (point mass), with respect to a non-rotating reference frame, fixed on the other body, is a conic section with a shape, size and orientation constant respect to the reference frame. A *conic section* can be defined as the geometric collection of all points P for wich the ratio of the distance to a fixed point F and the distance to a fixed line l is constant (Figure 3.1).

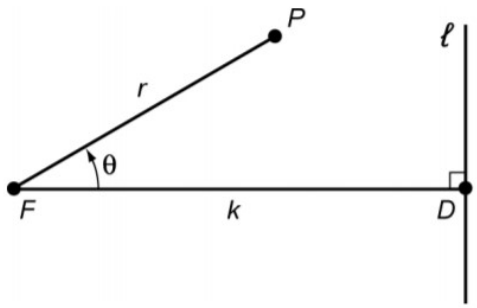

Figure 3.1: Geometric definition of a conic section

The fixed point F is called *focus*, the fixed line is called the *directrix* and the ratio of the distances is called the eccentricity "e" of the conic section. Following the figure notation, it's possible to define:

- when P is to the left of l:

$$r = e(k - r\cos\theta) \tag{3.1}$$

- when P is to the right of l:

$$r = e(r\cos\theta - k) \tag{3.2}$$

Introducing the *focal parameter*, p:

$$p = ek \tag{3.3}$$

it's possible to rewrite the previous equations as follows:

- when P is to the left of l:

$$r = p/(1 + e\cos\theta) \tag{3.4}$$

- when P is to the right of l:

$$r = -p/(1 - e\cos\theta) \tag{3.5}$$

Because of the symmetry of cosine functions with respect to $\theta = 0°$, the line $\bar{FD}$ is an axis of symmetry of the conic section. The type of conic section depends on eccentricity value:

- e = 0 : circle
- 0 < e < 1 : ellipse
- e = 1 : parabola
- e > 1 : hyperbola

Since both e and k can't assume a negative value, p has a finite positive value for all conic sections, the same goes for r, therefore [3.4], [3.5] could be rewritten as:

- when P is to the left of l:

$$\cos\theta \geq -1/e \tag{3.6}$$

- when P is to the right of l:

$$\cos\theta \geq 1/e \tag{3.7}$$

Because $e \geq 0$ and $\cos\theta \leq 1$ it is clear that the curve to the right of l can only be realized for e > 1, which corresponds to an hyperbola. The circle, the ellipse and the parabola are entirely located to the left of l, whereas the hyperbola has a branch to the left as well as to the right of l.
In order to define orbital elements, a proper non-rotating reference frame must be defined. The *Equatorial coordinate system*, as shown in figure 3.2, is a celestial coordinate system with the origin fixed in the Earth's center, the reference plane is the equatorial plane.

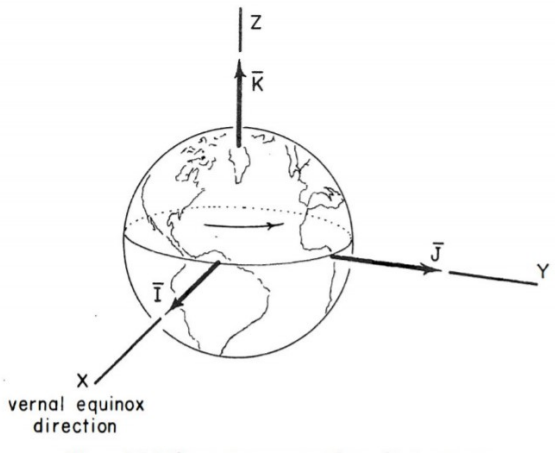

Figure 3.2: Equatorial coordinate system

The versor $\hat{I}$ is directed towards the *Vernal Equinox* and $\hat{J}$ towards the hemisphere that contains *Polaris*. Once orbits shape has been defined, orbital elements could be introduced. These parameters, shown in figure 3.3, are very useful to describe fundamental properties of the orbit and represents the most used method for orbit description. Assuming a non-rotating reference frame (Equatorial coordinate system) fixed on the main body (the Earth) and a secondary body, which often is a spacecraft or a planet, the six *orbital elements* could be defined as:

- **Semimajor axis (a)**: calculated as the sum of periapsis and apoapsis distance divided by two. Useful to define the size of the orbit.
- **Eccentricity (e)**: is a way of measuring how much the orbit deviates from a perfect circle, and is measured using a number between zero and one. An eccentricity of zero means the orbit is a circle. The closer the eccentricity is to one, the more stretched out the orbit is. Useful to define the shape of the orbit.
- **Inclination (i)**: angle between the orbit plane and the reference plane, which could be equatorial or ecliptic plane. the value of the inclination may range from 0° to 180°. Orbits may be categorized as direct or retrograde, based on their inclination. Direct orbit rotate towards east, this is the direction in which the Sun, the Earth, and most of the planets and their moons rotate around their own axes, and the direction in which all of the planets revolve around the Sun.

- **Longitude of the ascending node (Ω)**: angle between the X axis, which correspond to the Vernal Equinox direction, and the *nodal line*. The *nodal line* represents the line of intersection between the orbital plane and the reference plane (equatorial or ecliptic plane) and connects two specific points, the *ascending node* and the *descending node*, points of intersection between the *nodal line* and the orbit. This angle is measured eastward from 0° to 360°.
- **Argument of periapsis (ω)** : angle between the ascending node and the perigee of the orbit. Measures the orientation of the conic section in the orbital plane. So, ω, is measured from the nodal line in the direction of motion of the body in its orbital plane, from 0° to 360°.
- **True anomaly (γ)**: angle between the perigee and the actual position of the spacecraft during his trajectory.

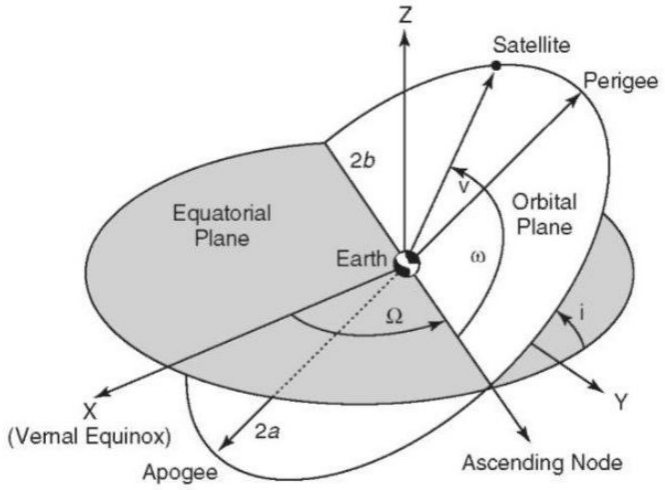

Figure 3.3: Orbital elements

An alternative sets of orbital elements has to be used in particular cases, when classic orbital elements are not suitable for describing certain orbits. Here follows some examples:

- When the orbital inclination is zero, both elements ω and Ω are unidentified. For equatorial orbits must be used $\tilde{\omega} = \Omega + \omega$, called *longitude of perigee* and describes the location of perigee. This angle is measured in the equatorial plane from the X-axis to the ascending node and subsequently in the orbital plane to perigee.

- When the orbit is circular, the orbital elements ω and γ are unidentified. For circular orbits must be used $u = \omega + \gamma$, called *argument of latitude* to described the in-orbit position of the satellite.
- For parabolic orbits a = inf and e=1, which means that both a and e does not allow to distinguish one parabolic orbit from another. In this case must be used $q = a(1 - e)$, which indicates the perigee distance.

3.2 Perturbations

Since orbital elements, described in the previous subsection, are derived from the solution for the *Two-Body Problem*, they don't take any form of perturbations into account and remain unchanged during the motion (except for the true anomaly). These phenomena lead to a value variation of all six orbital elements. Orbitals perturbations could be classified as follows (figure 3.4):

- **Secular Variations**: a linear variation of the element value, has a long-term effect on the orbit.
- **Short-Period Variations**: a periodic perturbation with a period similar or less than the orbital one.
- **Long-Period Variations**: a periodic perturbation with a period greater than the orbital one.

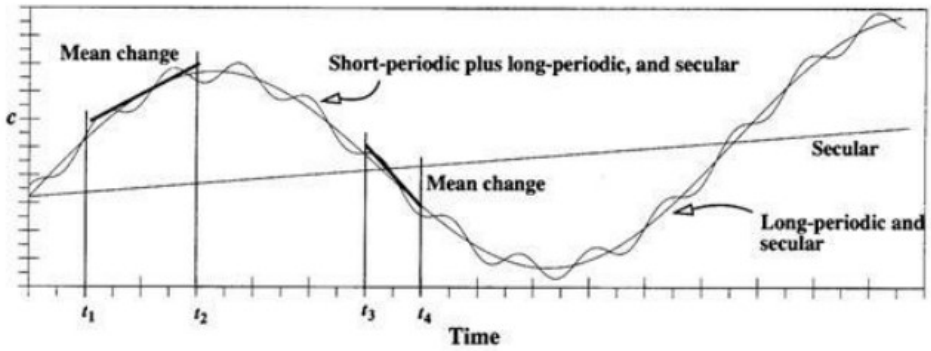

Figure 3.4: Classification of perturbations

Once a first classification has been defined, it's necessary to go deeper and discuss the most important perturbing forces.

3.2.1 Earth's gravitational force

Assuming the general case of a body with arbitrary shape and internal mass density distribution with a static external potential, neglecting the effects of solid-Earth, ocean and pole tides, *gravitational potential of Earth* at a point outside the Earth may be written as:

$$U = -\mu/r(1+\sum_{n=2}^{\inf}\sum_{m=0}^{n}(R/r)^n P_{\mathrm{n,m}}\sin\phi)(C_{\mathrm{n,m}}\cos m\Lambda + S_{\mathrm{n,m}}\sin m\Lambda)) \quad (3.8)$$

where:

- r, ϕ, Λ are the spherical coordinates of the point considered, relative to the geocentric rotating reference frame. r is the distance from the mass center of the Earth, ψ is the geocentric latitude and Λ is the geographic longitude.
- R is the mean equatorial Earth radius.
- $\mathrm{C_{n,m}}$ and $\mathrm{S_{n,m}}$ are model parameters
- $\mathrm{P_{n,m}}\sin\phi$ are *associated Legendre functions of the first kind* of degree n and order m.

When m=0 terms and $m \neq 0$ are separated, [3.8] could be rewritten as:

$$U = -\mu/r(1+\sum_{n=2}^{\inf}C_{\mathrm{n,0}}(R/r)^n P_{\mathrm{n,0}}\sin\phi) + \sum_{n=2}^{\inf}\sum_{m=1}^{n}(R/r)^n P_{\mathrm{n,m}}\sin\phi) \\ (C_{\mathrm{n,m}}\cos m\Lambda + S_{\mathrm{n,m}}\sin m\Lambda)) \quad (3.9)$$

where:

- $\mathrm{J_n} \equiv J_{\mathrm{n,0}} = \text{-}\mathrm{C_{n,0}}$
- $\mathrm{P_n}\sin\phi \equiv P_{\mathrm{n,0}}\sin\phi$
- $\mathrm{C_{n,m}} = \mathrm{J_{n,m}}\cos m\Lambda_{\mathrm{n,m}}$
- $\mathrm{S_{n,m}}=\mathrm{J_{n,m}}\sin m\Lambda_{\mathrm{n,m}}$

the expression for the gravitational potential can be written as:

$$U = -\mu/r(1 + \sum_{n=2}^{\inf} J_{\mathrm{n}}(R/r)^n P_{\mathrm{n}} \sin\phi) + \\ + \sum_{n=2}^{\inf} \sum_{m=1}^{n} J_{\mathrm{n,m}}(R/r)^n P_{\mathrm{n,m}} \sin\phi(\cos m(\Lambda - \Lambda_{\mathrm{n,m}})) \quad (3.10)$$

where the terms $\mathrm{P_n}(\sin\phi)$ are *Legendre polynomials* of degree n, $\mathrm{J_{n,m}}$ and $\Lambda_{\mathrm{n,m}}$ replace the model parameters $\mathrm{C_{n,m}}$ and $\mathrm{S_{n,m}}$.
For the *Legendre polynomials* and associated *Legendre function* of the first kind the following expressions hold:

$$x = \sin\phi$$

$$P_{\mathrm{n}}(x) = (1/(-2)^n n!)(d^n/dx^n)(1-x^2)^n \quad (3.11)$$

$$P_{\mathrm{n,x}} = (1-x^2)^{m/2}(d^m/dx^m)P_{\mathrm{n}}(x) \quad (3.12)$$

The definition $\mathrm{J_n} \equiv \text{-}\mathrm{C_{n,0}}$ makes $\mathrm{J_2}$ positive, so it's just a matter of convention. The summation index n begins at two, because the reference frame is fixed on Earth's center of mass and consequently $\mathrm{C_{1,0}}$, $\mathrm{C_{1,1}}$, $\mathrm{S_{1,1}}$, $\mathrm{J_1}$ and $\mathrm{J_{1,1}}$ are all zero. The coefficients $\mathrm{C_{2,1}}$, $\mathrm{S_{2,1}}$ and $\mathrm{J_{2,1}}$ would vanish if the Z-axis would be aligned with the Earth's main axis of inertia. A gravity model could now be built up with $\mathrm{C_{n,m}}$ and $\mathrm{S_{n,m}}$ coefficients, together with values of μ and R. The first term in [3.10] represents the gravitational potential of a spherical body with radially symmetric mass density distribution, called *the Newton potential*, whereas the second term represents the influence of deviations of the shape and mass density distribution in north-south direction and the third terms represents the influence of deviations of the shape and mass density distribution in north-south and east-west direction.
It's possible to define:

$$J_{\mathrm{n,m}} \equiv \sqrt{C_{\mathrm{n,m}}^2 + S_{\mathrm{n,m}}^2} \quad (3.13)$$

$$\Lambda_{\mathrm{n,m}} = 1/m \arctan C_{\mathrm{n,m}}/S_{\mathrm{n,m}} \quad (3.14)$$

where the signs of $\mathrm{C_{n,m}}$ and $\mathrm{S_{n,m}}$ determine the quadrant of $\Lambda_{\mathrm{n,m}}$. Modern gravity models contain coeffiecients up to degree and order 2150, and even up to higher. However, for most applications a truncated version is preferred. Based on n and m values it's possible to define:

- **Zonal Harmonics** when $n \neq 0$ and m=0
- **Sectorial Harmonics** when $n = m \neq 0$

- **Tesseral Harmonics** when $n \neq m \neq 0$

The spatial structure of *Zonal Harmonic* (a), *Sectorial Harmonic* (b), *Tesseral Harmonic* (c) is show in the figure below (Figure 3.5):

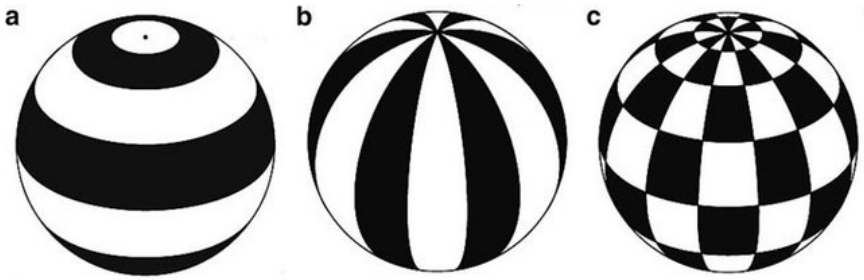

Figure 3.5: Spatial structure of spherical harmonics

Here follows a figure where some Harmonic values are collected (Figure 3.6).

n	m	$J_{n,m}$ (10^{-6})	$\Lambda_{n,m}$ (°)	n	m	$J_{n,m}$ (10^{-6})	$\Lambda_{n,m}$ (°)
Zonal harmonics							
2	0	1082.6357	-----	6	0	0.5406168	-----
3	0	-2.5324737	-----	7	0	-0.3505229	-----
4	0	-1.6199743	-----	8	0	-0.2040168	-----
5	0	-0.2279051	-----	9	0	-0.1221502	-----
Tesseral and sectorial harmonics							
2	1	0.0018225	98.3325	5	2	0.1177945	-13.1874
2	2	1.8155628	-14.9287	5	3	0.0165311	-51.5184
3	1	2.2094849	6.9684	5	4	0.0023321	42.6063
3	2	0.3744510	-17.1887	5	5	0.0017034	-15.0730
3	3	0.2213884	20.9932	6	1	0.0632600	160.7431
4	1	0.6786576	-138.5480	6	2	0.0468934	-41.2906
4	2	0.1675835	31.0578	6	3	0.0012011	2.9578
4	3	0.0604207	-3.8219	6	4	0.0018140	-25.0853
4	4	0.0076442	30.3487	6	5	0.0004837	-23.2946
5	1	0.0971238	-123.6853	6	6	0.0000554	-14.6194

Figure 3.6: Some coefficients of the GRACE GGM02C Earth gravity field model

The value of J_2, that represents the first perturbing term, is way greater than all other J-coefficients, so the first perturbing terms produces by far the largest perturbing force. In order to quantify the perturbing force due to J_2 term, a perturbing acceleration $\bar{f}$ is defined as follows:

$$\bar{f} = -\bar{\nabla}(U + \mu/r) \tag{3.15}$$

Assuming the only effect of J_2 [3.10] could be rewritten as:

$$\bar{f} = -\bar{\nabla}(\mu/rJ2(R/r)^2 P_2(\sin\phi)) \tag{3.16}$$

Developing equation [3.11], the following result is obtained:

$$P_2(\sin\phi) = 1/2(3\sin^2\phi - 1) \tag{3.17}$$

then substituting the previous equation in [3.16]:

$$\bar{f} = -\bar{\nabla}(1/2\mu J2(R^2/r^3)P_2(3\sin^2\phi - 1)) \tag{3.18}$$

with $\sin\phi = z/r$, [3.18] becomes:

$$\bar{f} = -\bar{\nabla}(1/2\mu J2(R^2/r^3)P_2(3(z^2/r^2 - 1)) \tag{3.19}$$

Starting from [3.19], the rectangular components of the perturbing acceleration could be derived as:

- $f_{\mathrm{x}} = -3/2\mu J2(R^2/r^5)x(3(1 - 5z^2/r^2))$
- $f_{\mathrm{y}} = -3/2\mu J2(R^2/r^5)y(3(1 - 5z^2/r^2))$
- $f_{\mathrm{z}} = -3/2\mu J2(R^2/r^5)z(3(1 - 5z^2/r^2))$

It's useful now to change from rectangular to spherical coordinates as follows:

- $f_{\mathrm{r}} = 3/2\mu J2(R^2/r^4)(3\sin^2\phi - 1))$
- $f_\phi = -3/2\mu J2(R^2/r^4)(\sin 2\phi))$
- $f_\Lambda = 0$

A visualization of the direction of the J_2 acceleration is shown below:

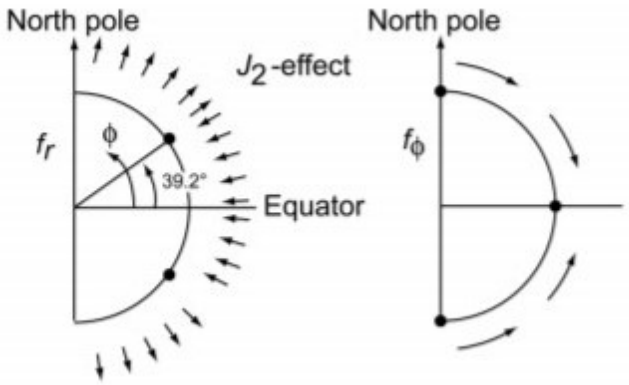

Figure 3.7: Diagrams for the direction of the J_2 accelerations in the meridional plane.

When acceleration direction change, as it is shown in figure 3.7, the value of f goes to zero. In particular:

- f_r=0 if ϕ=-39.18°, 39.18°
- f_ϕ=0 if ϕ=-90°,0°,90°

Since J_2 is greater than zero, f_r is positive for $\phi > 39.2°$ and $\phi < -39.2°$ and negative for -39.2°< ϕ <39.2°. The latitude acceleration, f_ϕ, is negative for 0°<ϕ<90° and positive for -90°<ϕ<0°. Figure [3.7], in which J_2 effect is represented, may suggests an additional ring of mass around Earth's equator and a shortage of mass at the polar regions. However this theory is not correct as may seems, since J_2 effects depends on Earth's potential and could also be seen as a perfect sphere with a higher density around the equator. The maximum value of perturbing acceleration components, for a specified distance r, are:

- $|f_r|_{max}=3/2\mu J_2(R^2/r^4)$ at ϕ=-90°,90°
- $|f_\phi|_{max}=-3/2\mu J_2(R^2/r^4)$ at ϕ=-45°,45°

it could be useful to make an example, assuming a satellite at an altitude of 250km the perturbing acceleration components are: $|f_r|_{max}=2$ $|f_\phi|_{max}=2.73$ cm/s^2, which is about 0.3% of Earth's gravitational acceleration (9.81 m/s^2). For higher altitudes are smaller and smaller. For a Geostationary satellite, the J_2 effect produces a constant acceleration of $-8.33 * 10^{-6} m/s^2$ in radial

direction, which is about 0.004% of Earth's gravitational acceleration.
Since Earth completes one revolution about it's axis in one day while the satellite orbit in LEO keeps a fixed orientation in space, the deviations in the shape will average out over period loger than a day, consequently $J_{n,m}$ terms could be ignored form most of applications. Whereas, Geostationary satellite, located above the same point on Earth's equator, is strongly perturbed by $J_{n,m}$ terms. However, Since the value (R/r)=0.15, in most cases only the first few $J_{n,m}$ terms must be taken into account.

3.2.2 Atmospheric Drag

Atmospheric Drag represents a friction force, acting opposite to the relative motion of an object and it's quite important at low altitude. First of all it's necessary to define the acceleration component:

$$\bar{f} = -1/2 C_D \rho A/M |\bar{v}| \bar{v} \tag{3.20}$$

where:

- ρ is the atmospheric density
- $\bar{v}$ is the velocity of the satellite relative to Earth's atmosphere
- M is the mass of the satellite
- C_D is the drag coefficient related to the surface A

The force generated on the satellite surfaces is mainly tangential, even a perpendicular component is exerted on the satellite but is so small that could be ignored. While the satellite mass is well defined, serious problems come out trying to define C_D,A and ρ.
At altitude above 180km, the mean free path is larger than 120m, consequently the flow around the satellite could be defined as a *free molecular flow type*. If altitude and shape of the satellite are well known, surface orientation relative to the incoming flow could be derived. However, this process could be very complicated and usually it's preferred to use the cross-sectional area of the satellite, perpendicular to the velocity vector, as a reference surface. The drag coefficient, C_D, depends on the kind of atmospheric particles that strike the satellite, the kinetic energy of those, the satellite speed, the satellite surface characteristics and temperature. After the definition of these parameters, C_D can be computed. The value of this coefficient lies on a range between 2 and 3, for lower altitude tends to be closer to 2 and for higher altitude to 3.

3.2.3 Gravitational attraction by other celestial bodies

The presence of other celestial bodies besides the Earth, specially the Moon and the Sun, will create a perturbing force that affects the orbit of the satellite. Assuming the presence of a single perturbing body, denoted as j, the perturbing acceleration of the satellite, denoted as i, around the Earth, denoted as k, could be derived from the *multy-body problem* as:

$$\bar{f} = -\bar{\nabla}(-\mu_{\mathrm{j}}(1/r_{\mathrm{ij}} - (x_{\mathrm{i}}x_{\mathrm{j}} + y_{\mathrm{i}}y_{\mathrm{j}} + z_{\mathrm{i}}z_{\mathrm{j}})/r_{\mathrm{j}}^3)) \tag{3.21}$$

where $\mu_{\mathrm{j}} = Gm_{\mathrm{j}}$ and:

$$r_{\mathrm{ij}}^2 = (x_{\mathrm{i}} - x_{\mathrm{j}})^2 + (y_{\mathrm{i}} - y_{\mathrm{j}})^2 + (z_{\mathrm{i}} - z_{\mathrm{j}})^2 \tag{3.22}$$

through which it's possible to derive the rectangular components of the perturbing acceleration:

- $\mathrm{f_x} = \mu_{\mathrm{j}}((x_{\mathrm{j}} - x_{\mathrm{i}})/r_{\mathrm{ij}}^3 - x_{\mathrm{j}}/r_{\mathrm{j}}^3)$
- $\mathrm{f_y} = \mu_{\mathrm{j}}((y_{\mathrm{j}} - y_{\mathrm{i}})/r_{\mathrm{ij}}^3 - y_{\mathrm{j}}/r_{\mathrm{j}}^3)$
- $\mathrm{f_y} = \mu_{\mathrm{j}}((z_{\mathrm{j}} - z_{\mathrm{i}})/r_{\mathrm{ij}}^3 - z_{\mathrm{j}}/r_{\mathrm{j}}^3)$

All coordinates are referred to a non-rotating reference frame fixed on the Earth's center. The maximum valued of the ratio between the acceleration due to the gravitational attraction by the perturbing body, $\mathrm{f_d}$, and by the Earth, $\mathrm{f_E}$, could be written as:

$$(f_{\mathrm{d}}/f_{\mathrm{E}})_{\max} = 2m_{\mathrm{d}}/m_{\mathrm{E}}(r_{\mathrm{i}}/r_{\mathrm{d}})^3 \tag{3.23}$$

The relative perturbing acceleration increases with increasing orbital altitude of the satellite, consequently, the geostationary orbit are the most influenced by this kind of perturbation. In the figure 3.8 is shown the value of perturbing acceleration for a geostationary satellite due to the presence of a perturbing body.

Perturbing body	m_d/m_E	r_s/r_d	$(a_d/a_m)_{max}$
Sun	$3.33*10^{5}$	$2.82*10^{-4}$	$1.5*10^{-5}$
Moon	$1.23*10^{-2}$	$1.10*10^{-1}$	$3.9*10^{-5}$
Mercury	$5.53*10^{-2}$	$4.60*10^{-4}$	$1.1*10^{-11}$
Venus	$8.15*10^{-1}$	$1.02*10^{-3}$	$1.7*10^{-9}$
Mars	$1.07*10^{-1}$	$5.38*10^{-4}$	$3.4*10^{-11}$
Jupiter	$3.18*10^{2}$	$6.71*10^{-5}$	$1.9*10^{-10}$
Saturn	$9.52*10^{1}$	$3.30*10^{-5}$	$6.8*10^{-12}$
Uranus	$1.45*10^{1}$	$1.55*10^{-5}$	$1.1*10^{-13}$
Neptune	$1.71*10^{1}$	$9.70*10^{-6}$	$3.1*10^{-14}$
Pluto	$2.10*10^{-3}$	$7.32*10^{-6}$	$1.7*10^{-18}$
Proxima Centauri	$4.09*10^{4}$	$1.06*10^{-9}$	$9.6*10^{-23}$
Large Magellanic Cloud	$\approx 10^{15}$	$\approx 10^{-14}$	$\approx 10^{-25}$

Figure 3.8: Gravitational perturbing acceleration values for different perturbing bodies

3.2.4 Radiation Force

Satellites orbiting around the Earth will experience a radiation force due to direct sunlight, sunlight reflected by the Earth, called *albedo radiation*, and thermal infrared radiation emitted by the Earth, called *terrestrial radiation*. The force acting upon the satellite, due to radiation, could be written as:

$$F = C_{\mathrm{R}} W A/c \tag{3.24}$$

where:

- W is the energy flux of the solar radiation
- A is the effective cross-sectional area of the satellite
- c is the speed of light
- C_R is the satellite reflectivity
- $C_R W/c$ is the radiation pressure

and the perturbing acceleration due to radiation force could be written as:

$$\bar{f} = -C_{\mathrm{R}}(WA/cM)\bar{e}_{\mathrm{S}} \tag{3.25}$$

where M is the mass of the satellite and $\bar{e}_S$ is the unit vector from the satellite to the Sun. Consequently the force acts along the Sun-satellite vector. The

energy flux of the solar radiation, at the distance of 1 AU, is approximately 1361 W/m^2. Whereas, *albedo radiation*, produced by reflection and scattering of incident solar radiation, can vary from 95 W/m^2, over a cloudless ocean, to 1250 W/m^2, over large and thick cumulonimbus clouds. In contrast to albedo radiation, the *Earth's infrared radiation* is a near isotropic re-emission of direct solar radiation absorbed by the Earth and its atmosphere and correspond to the spectrum of a black body with an effective temperature of 255K, leading to an average energy flux of 240 W/m^2.

3.3 Impulsive Maneuvers

In this section, different types of maneuvers are discussed. The first to be introduced are impulsive maneuvers, co-planar and out-of-plane maneuvers in particular, up to low-thrust maneuvers.

3.3.1 Impulsive Co-planar Transfer

Assuming two circular co-planar orbits, characterized by two different radius, r_1 and r_2, in order to accomplish successfully the maneuver, the satellite must get into an intermediate orbit that intersects both initial and target orbits. This last condition could be summarized as follows (figure 3.9):

- the periapsis radius of the transfer orbit must be equal or less than the radius of the inner orbit

$$r_{\mathrm{p}} = p/(1+e) \leq r_1 \tag{3.26}$$

- the apoapsis radius of the transfer orbit must be equal or greater than the outer orbit

$$r_{\mathrm{a}} = p/(1-e) \geq r_2 \tag{3.27}$$

where p and e are the parameter (semi-latus rectum) and eccentricity of the transfer orbit, while r_1 and r_2 are, respectively, the radii of the inner and the outer orbits. Once all conditions have been defined, the energy (E_t) and angular momentum (h_t) of the transfer orbit could be defined as:

- $E_{\mathrm{t}} = -\mu(1-e^2)/2p$
- $h_{\mathrm{t}} = \sqrt{\mu p}$

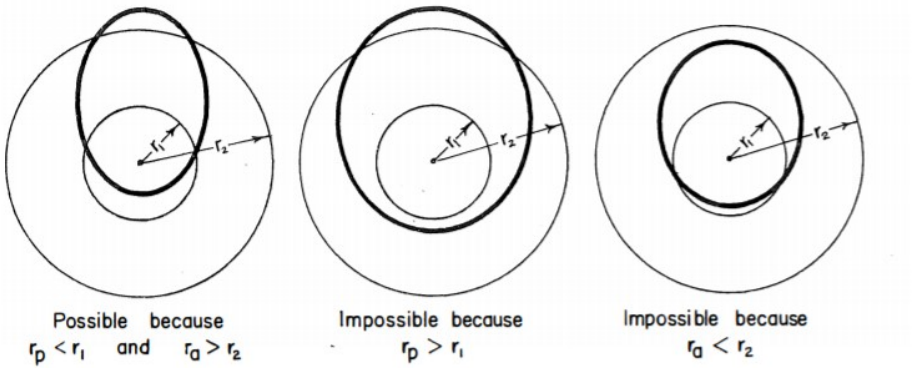

Figure 3.9: Co-planar transfer between circular orbits

Solving the energy equation for the speed at point 1 (beginning of maneuver) in the transfer orbit:

$$v_1\sqrt{2(\mu/r_1 + E_t)} \tag{3.28}$$

assuming a circular velocity, for the inner orbit, as:

$$v_{CS1} = \sqrt{\mu/r_1} \tag{3.29}$$

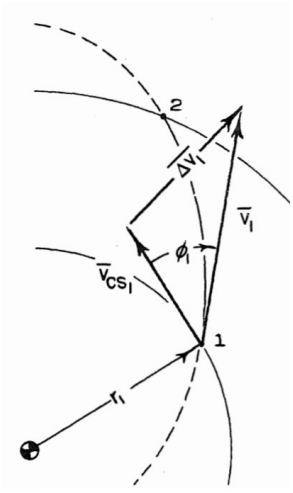

Figure 3.10: schematic of the maneuvers at point 1

defining ϕ_1 as the angle between v_1 direction and v_{CS1} direction, and $h = rv\cos\phi$.

$$\cos\phi_1 = h_t/r_1 v_1 \tag{3.30}$$

Since all needed data are available, it's possible to calculate the ΔV_1 required as:

$$\Delta V_1 = v_1^2 + v_{\mathrm{CS1}}^2 - 2v_1 v_{\mathrm{CS1}} \cos\phi_1 \tag{3.31}$$

whereas, the same method could be applied to compute the ΔV_2 required:

$$\Delta V_2 = v_2^2 + v_{\mathrm{CS2}}^2 - 2v_2 v_{\mathrm{CS2}} \cos\phi_2 \tag{3.32}$$

The total cost of the maneuver could easily be defined as:

$$\Delta V_{\mathrm{TOT}} = \Delta V_1 + \Delta V_2 \tag{3.33}$$

3.3.2 The Hohmann transfer

The least ΔV required for a transfer between two circular orbits is achieved by using a doubly-tangent transfer ellipse (figure 3.11), called *Hohmann Transfer*. This maneuver could be achieved through the following conditions:

- the periapsis radius of the transfer orbit must be equal to the radius of the inner orbit
$$r_{\mathrm{p}} = p/(1+e) = r_1 \tag{3.34}$$
- the apoapsis radius of the transfer orbit must be equal to the outer orbit
$$r_{\mathrm{a}} = p/(1-e) = r_2 \tag{3.35}$$

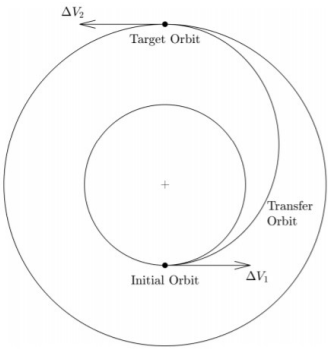

Figure 3.11: schematic of the Hohmann transfer

Assuming to travel from the inner orbit (r_1) to the outer orbit (r_2), v_1 can be computed through the energy equation of the transfer orbit.

$$E_{\mathrm{t}} = -\mu/2a_{\mathrm{t}} = -\mu/(r_1 + r_2) \tag{3.36}$$

$$v_1 = \sqrt{2(\mu/r_1 + E_t)} \tag{3.37}$$

Since the angle of misalignment ϕ is zero in both begging and arrival point, the cost of Hohmann maneuver could be defined as:

$$\Delta V_1 = v_1 - v_{CS1} \tag{3.38}$$

With the same method is easy to find the ΔV_2:

$$\Delta V_2 = v_2 - v_{CS2} \tag{3.39}$$

consequently the total cost of the Hohmann transfer could be found:

$$\Delta V_{TOT} = \Delta V_1 + \Delta V_2 \tag{3.40}$$

The time-of-flight for a Hohmann transfer correspond to half period of the transfer orbit and could be defined as:

$$T = \pi\sqrt{a_t^3/\mu} \tag{3.41}$$

Hohmann transfer represents the most economical maneuver, in term of ΔV required, whereas it takes longer than any other possible manouver between the same two circular orbits.

3.3.3 Impulsive Out-of-Plane Transfer

In order to change the orientation of the orbital plane, and not only the size or shape, a ΔV component perpendicular to the orbital plane is required. Assuming the needs to a simple plane change, after the application of a ΔV, the speed of flight and the flight-path angle are unchanged and only the inclination has been modified.

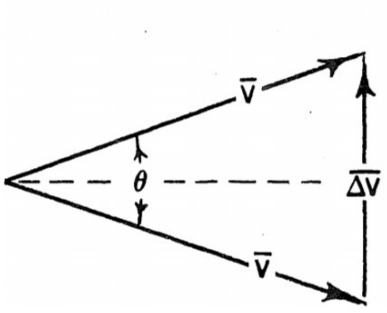

Figure 3.12: schematic of simple plane change

Assuming a plane change from an inclined orbit to an equatorial one, a perpendicular ΔV is applied to achieve an inclination variation of θ. The initial and final velocity magnitude is the same and together with the ΔV vector form an isosceles triangle (figure 3.12) that allows to apply the law of cosines to find the ΔV required.

$$\Delta V = 2v \sin(\theta/2) \tag{3.42}$$

In order to change the inclination from a certain value to zero (equatorial orbit), the ΔV must be applied at one of the nodes (intersection point figure 3.13).

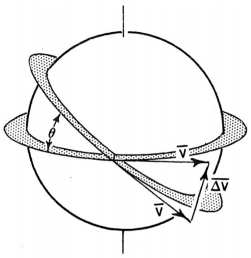

Figure 3.13: simple plane change maneuver

3.4 Low-Thrust maneuver

Unlike the impulsive maneuver, that achieves a certain result through the application of an high thrust for an infinitesimal time lapse, *low-thrust maneuver* are carried out through a continuous thrust production linked to long time lapse (figure 3.14).

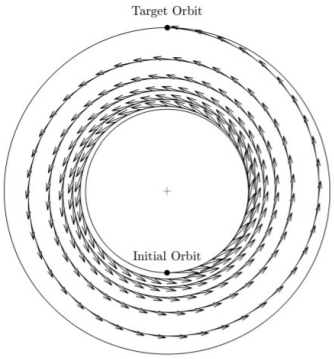

Figure 3.14: Low-thrust maneuver

3.4.1 Low-Thrust transfer solution through indirect method

Classical approaches to low-thrust trajectory optimization consist of using optimal control theory, name indirect method, Lagrange multiplier or adjoint variables. The first who tried to get proper result was Edelbaum with his theory on transfer between circular orbits of different semimajor axis and inclination. As will be shown in the next chapter, Edelbaum developed an analytical solution to maximize the inclination change achieving a specific change of semimajor axis. A deeper analysis was conducted by Edelbaum to analyze the multi-revolutions transfer in order to minimizing consumption for a fixed transfer duration with semimajor axis and inclination specified. The assumption made to simplify the model, such as considering only circular orbits throughout the transfer and a constant thrust angle for each revolution, didn't seem to affect the validity of the model. Whereas, assuming the thrust acceleration constant throughout all transfer didn't allow to define a proper fuel consumption and considering two-body dynamics was not suitable for long duration missions.
Wiesel and Alfano reworked the problem to minimize the maneuver cost, with semimajor axis and inclination well specified, assuming a thrust magnitude and mass flow rate constant, instead of a constant thrust acceleration and the thrust angle was allowed to vary. They solved the resulting two-point boundary value problem numerically to produce a contour map of a Lagrange multiplier as a function of Δa and Δi.
Kéchichian reformulated Edelbaum's theory as a minimum time problem and found an analytical expression for the time-varying thrust angle to achieve the desired Δa and Δi. He obtained the adjoint equations of motion for the minimum time rendezvous problem in non-singular equinoctial elements and presented a numerical solution with Newton-Raphson iteration. Then he extended this result to long duration rendezvous improving Edelbaum's transfer to include changes in the right ascension of the ascending node $\Delta\Omega$ and Earth's J_2 perturbation. The indirect problem is solved when adjoint variables are found to produce admissible states and controls that extremize the Hamiltonian at very instant in time, while satisfying boundary conditions. This analysis allowed to find an analytic expression that enable quick trajectory computation. However, adjoint variables need to be guessed, evaluated in the motion equations and than corrected.

3.4.2 Edelbaum's Theory

Through *Edelbaum's law of motion*, the dynamic low thrust maneuver could be explained. Assuming, for simplicity, only circular orbits with low level of inclination and thrust involved, the following approximation could be made:

- $r \approx a \approx p$
- $V^2 \approx \mu/r$
- $\theta = \Omega + \omega + \nu$
- $e \approx 0$
- $a_{\mathrm{T}} << \mu/r^2$
- $a_{\mathrm{R}} << \mu/r^2$
- $a_{\mathrm{W}} << \mu/r^2$

where the last three conditions say that all the acceleration components, inside the plane (tangential (T) and perpendicular (R) to the velocity vector) and out-of-plane (W), are far smaller than the gravitational acceleration. Once all conditions has been defined, equations of motion could be written as follows:

$$\begin{cases} V\dot{a}/a = 2a_{\mathrm{T}} \\ V\dot{E} = 2\cos\nu a_{\mathrm{T}} + \sin\nu a_{\mathrm{R}} \\ V\dot{i} = \cos\omega + \nu a_{\mathrm{W}} \\ iV\dot{\Omega} = \sin\omega + \nu a_{\mathrm{W}} \\ V\dot{\omega} = -V\dot{\Omega} + (2\sin\nu a_{\mathrm{T}} - \cos\nu a_{\mathrm{R}})/e \\ \dot{\theta} = n = \sqrt{\mu/a^3} \end{cases} \tag{3.43}$$

Before moving on to the integration of motion equations, could be useful to redefine acceleration component as follows:

$$a_{\mathrm{T}} = A\cos\alpha\cos\beta \tag{3.44}$$

$$a_{\mathrm{R}} = A\sin\alpha\cos\beta \tag{3.45}$$

$$a_{\mathrm{W}} = A\sin\beta \tag{3.46}$$

where A=T/m represents the *overall acceleration*. In this sections, the equations for Ω and ω are neglected and both are considered constant. The next step is the integration of the motion equations over a single revolution,

that means a variation of time from t_0=0 to t_f=$2\pi\sqrt{a^3/\mu}$ and ν from 0 to 2π).

$$\Delta a = (2aA/V)\int_0^{2\pi} \cos\alpha \cos\beta d\nu \tag{3.47}$$

$$\Delta e = (A/V)\int_0^{2\pi} (2\cos\alpha\cos\nu + \sin\nu\sin\alpha)\cos beta d\nu \tag{3.48}$$

$$\Delta i = (A/V)\int_0^{2\pi} \cos\omega + \nu\sin\beta d\nu \tag{3.49}$$

Once the variation of orbital elements has been defined, a study for each parameter change is conducted:

- $\boldsymbol{\Delta a}$: planar case where the maximum increase in a is obtained through $\alpha = \beta = 0$, consequently a_T=A, a_R=a_W=0 and $\Delta e = \Delta i = 0$
- $\boldsymbol{\Delta e}$: planar case where the maximum increase in e is obtained through $\tan\alpha = (1/2)\tan(\nu/2)$, $\beta = 0$ and $\Delta a = \Delta i = 0$
- $\boldsymbol{\Delta i}$ and $\boldsymbol{\Delta a}$: three-dimensional case where the maximum increase in both a and i is obtained through $\tan\beta = k\cos\omega + \nu$, that means a_T = $A\cos\beta$, a_R=0 and a_W = $A\sin\beta$ (with β to be specified).

With the Edelbaum's maneuver, a great value change of semimajor axis and inclination is achieved, maintaining the orbit circular, through a great number of orbit revolutions. So the next step is the calculation of parameters change over multiple orbit revolutions.
Assuming $\theta = \omega + \nu$, acceleration components could be rewritten as:

$$a_T = A/\sqrt{1 + (k\cos\theta)^2} \tag{3.50}$$

$$a_W = Ak\cos\theta/\sqrt{1 + (k\cos\theta)^2} \tag{3.51}$$

Using these acceleration components for the integration, leads to an analytically unsolvable problem. In order to solve this issue, an approximation must be taken into account. From now on β should be considered constant ($\bar{\beta}$) as shown in Figure[3.15].

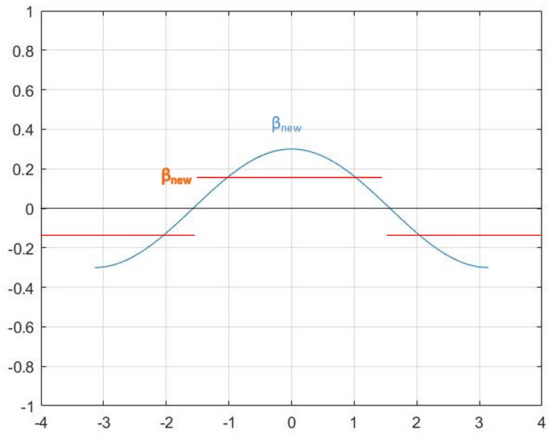

Figure 3.15: Beta angle

it's now possible to resolve the integration and finds:

$$\Delta a/a = a\pi A \cos\bar{\beta}/nV \tag{3.52}$$

$$\Delta i = 4A \sin\bar{\beta}/nV \tag{3.53}$$

$$\Delta t = 2/pi/n \tag{3.54}$$

Using a constant value of β does not affect much the accuracy of the model, differences between optimal value and constant value of β is shown in Figure[3.16].

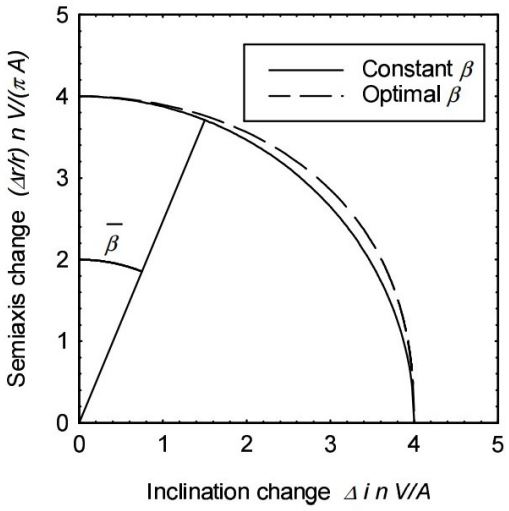

Figure 3.16: Differences between optimal value and constant value of β

In order to evaluate the behavior of the parameters through multiple revolutions is useful to compute the derivative for each one, dividing the variation on one revolution by the Δt. Obtaining:

$$\dot{a} = 2Aa\cos\beta/V \tag{3.55}$$

$$\dot{i} = 2A\sin\beta/\pi V \tag{3.56}$$

$$\dot{V} = -n\dot{a}/2 \tag{3.57}$$

Then it's necessary to define the first derivative of i and t with respect to dV:

$$di/dV = -2\tan\beta/\pi V \quad dt/dV = -1/a\cos\beta \tag{3.58}$$

in order to find the optimal value of β, the first derivative with respect to dβ must be equal to zero:

$$\partial(di/dV + k(dt/dV))/\partial\beta = 0 \tag{3.59}$$

that leads to the following solution:

$$V\sin\beta = V_0\sin\beta_0 = constant \tag{3.60}$$

The means of equation [3.60] is that for great radii the β angle must be large. In a few words, once β_0 has been selected, motion equations are integrated up to r_1, that corresponds to a certain value of velocity.
Assuming a maneuver that increase the orbit radius with a fixed β_0, the solution could be visualized in Figure[3.17].

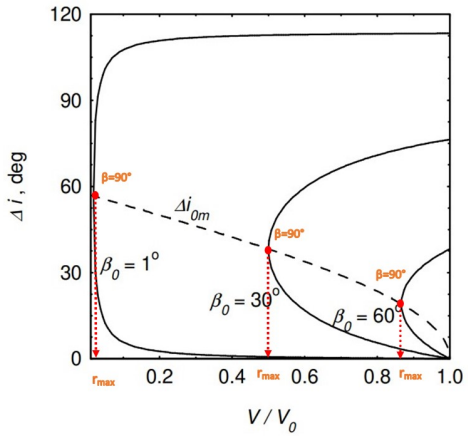

Figure 3.17: three-dimensional Edelbaum's manouver

With a fixed β_0 there's a maximum value of radius reachable, higher is the value of β_0 and lower will be the radius value. This is due to the fact that β increases with the radius and starting with an high angle value leads to an early achievement of the maximum value of β (90°) and r_{max}. With small value of β_0 it's possible to reach more distant orbits.
In terms of a reachable combination of radius and inclination, all points that lie beneath the black dashed line in Figure [3.17] could be reached directly. In order to get on a point that lies above the same line, β must go over 90° and, consequently, the spacecraft would start to decelerate reaching a lower orbit with a two-way transfer. The maximum one-way inclination change is obtained for $\beta_0 \to 0$, which gives V_{max}=0, r_{max}=inf and Δ_{max}=57.3°.
The ΔV required could be obtained as:

$$\Delta V = \sqrt{V_0 + V_1 - 2V_0V_1 \cos{(\pi/2)\Delta i}} \quad if \quad \Delta i < 114,6^\circ \tag{3.61}$$

3.5 Edelbaum' theory with J_2 effect

Since the analysis conducted in this work takes into account gravitational perturbations, *Edelbaum's theory* must be supplemented with the J_2 effect. This applies especially to LEO orbits with a sufficient altitude to suffer little aerodynamic effects and could remain stable for long period of time. As seen in chapter 3.3, J_2 effect causes secular and short-period variations of the orbital elements.
The same assumptions made in chapter 3.4.2 are still valid and since considered orbits are almost circulars, changes of eccentricity, argument of periapsis and the true anomaly equation are neglected.
As discussed in Chapter 1.1, a chaser spacecraft is on an initial orbit, dictated by the launcher trajectory, defined by semimajor axis value, inclination and RAAN (Ω), whereas the target orbit is well defined in the same way. Due to J_2 effect, the target and spacecraft RAAN changes over time and this effect could be used as a benefit.
In order to understand properly the phenomenon, Edelbaum's theory must be modified, starting from the one-revolution transfer up to the multiple-revolution transfer.

3.5.1 One-Revolution Transfer

The same assumptions made in chapter 3.4.2 are adopted, and short-period variations due to J_2 effect are negleted. In this study only secular variations

are considered and the J_2 effect on RAAN change could be defined through the derivative with respect to time:

$$\begin{aligned}\dot{\Omega}_{\mathrm{J2}} &= -(3/2)J_2(r_{\mathrm{E}}/a)^2(V/r)\cos i \\ &= -(3/2)J_2(r_{\mathrm{E}}/a)^2(\mu^{1/2}a^{-3/2})\cos i\end{aligned} \tag{3.62}$$

Equation [3.62] depends only on semimajor axis and inclination. Since eccentricity changes are neglected, the only control variable is the out-of-plane angle of thrust β. In order to take into account the J_2 effect, differential equations found in chapter 3.4.2 are rewritten as follows:

$$\dot{a} = 2Aa\cos\beta/V \tag{3.63}$$

$$\dot{i} = A\sin\beta\cos\theta/V \tag{3.64}$$

$$\sin i\dot{\Omega} = A\cos\theta\cos\beta - J_2(3/2)(r_{\mathrm{E}}/a)^2V/a\cos i\sin i \tag{3.65}$$

it could be useful to rewrite these equations using θ (measured starting from the ascending node) as the independent variable instead of time.

$$da/d\theta = 2a^3A\cos\beta/\mu \tag{3.66}$$

$$di/d\theta = a^3 2\cos\theta\sin\beta/\mu \tag{3.67}$$

$$d\Omega/d\theta = a^2A\sin\theta sin\beta/\sin i - J_2(3/2)(r_{\mathrm{E}}/a)^2\cos i \tag{3.68}$$

$$dt/d\theta = \sqrt{a^3/\mu} \tag{3.69}$$

Since thrust and J_2 effect are really small and just one revolution has been taken into account, semimajor axis, inclination and thrust acceleration could be considered constant. An Hemiltonian optimal law has been applied in order to obtain an indirect optimization of the problem. For each differential equations have been associated an adjoint variable λ and consequently the Hamiltonian has been defined as:

$$H = \lambda_{\mathrm{a}}2Aacos\beta + \lambda_{\mathrm{i}}A\cos\theta\sin\beta + \lambda_\Omega(A(\sin\theta sin\beta/sini) - J_2 3/2(r_{\mathrm{E}}/a)^2\cos i) \tag{3.70}$$

where A, in this case, represents the non-dimensional acceleration $A = (T/m)/(\mu/a^2)$. Since the one-revolution problem is being studied, H does not depend on the state variable and the adjoint variables could be treated as adjoint constants. Nullifying the partial derivative of the Hamiltonian, the optimal thrust angle β is obtained as:

$$\tan\beta = (\lambda_{\mathrm{i}}\cos\theta + (\lambda_\Omega/\sin i)\sin\theta)/(2\lambda_{\mathrm{a}}a) \tag{3.71}$$

It could be useful to introduce the angle θ_0 as:

$$\tan\theta_0 = (\lambda_\Omega/\sin i)/\lambda i \tag{3.72}$$

I'ts now possible to give a definition to the adjoint variables through the introduction of:

$$\Lambda = \sqrt{\lambda_{\mathrm{i}}^2 + (\lambda_\Omega/\sin i)^2} \tag{3.73}$$

obtaining:

$$\lambda_{\mathrm{i}} = \Lambda\cos\theta_0 \qquad \lambda_\Omega/\sin i = \Lambda\sin\theta_0 \tag{3.74}$$

The β angle could now be rewritten as:

$$\tan\beta = \Lambda/(2\lambda_{\mathrm{a}}a)\cos(\theta-\theta_0) = K\cos(\theta-\theta 0) \tag{3.75}$$

Another modification to β could be defined through the introduction of two new variables:

$$\theta' = \theta - \theta_0 \qquad K' = \sqrt{1+(K\cos\theta')} \tag{3.76}$$

obtaining:

$$\cos\beta = 1/K' \qquad sin\beta = K\cos\theta'/K' \tag{3.77}$$

The final form of the differential equations can be finally obtained

$$da/d\theta' = A(2r/K') \tag{3.78}$$

$$di/d\theta' = A(K\cos\theta'\cos(\theta'+\theta_0))/K' \tag{3.79}$$

$$d\Omega/d\theta' = (A/\sin i)(K\cos\theta'\sin(\theta'+\theta_0)/K' - J_2 3/2(r_{\mathrm{E}}/a)^2\cos i \tag{3.80}$$

Elliptic integrals are used to solve the one-revolution problem successfully. Assuming θ_0 and neglecting J_2 effect, the same solutions of Chapter 3.4.2 are found for changes in semimajor axis and inclination. The differences between this model and the Edelbaum's solution could be summarized as follows:

$$\Delta i = \Delta i_0\cos\theta_0 \qquad \Delta\Omega = (\Delta i_0/\sin i)\sin\theta_0 - 3\pi J_2(r_{\mathrm{E}}/a)^2\cos i \tag{3.81}$$

In these equation, thanks to the presence of θ_0, the contribution of out-of-plane thrust in inclination and RAAN change is split. As seen in chapter 3.4, β angle could be assumed constant without a great loss of accuracy in order to make the equations analytically integrable. The integration results over a single revolution are:

$$\Delta a = 4\pi A a\cos\beta \tag{3.82}$$

$$\Delta i = aA\sin\beta\cos\theta_0 \tag{3.83}$$

$$\Delta\Omega = 4A(\sin beta/\sin i)\sin\theta_0 - 3\pi J_2(r_{\mathrm{E}}/a)^2\cos i \tag{3.84}$$

$$\Delta t = 2\pi\sqrt{a^3/\mu} \tag{3.85}$$

3.5.2 Multiple-Revolution Transfer

Once the one revolution model has been studied, a *multiple-revolution transfer* could be introduced. With the same assumption made in the previous analysis, such as considering the β angle constant, the time derivatives of the orbital elements are calculated through the ratio of changes over a single revolution (Δa,Δi,$\Delta\Omega$) to the orbital period (Δt). The spacecraft mass equation must be added to the state equations, since mass consumption could not be neglected anymore in multiple-revolution transfer.

$$da/dt = 2T/m\sqrt{a^3/\mu}\cos\beta \tag{3.86}$$

$$di/dt = 2T/\pi m\sqrt{a/\mu}\sin\beta\cos\theta_0 \tag{3.87}$$

$$d\Omega/dt = 2T/\pi m\sqrt{a/\mu}\sin\beta(\sin\theta_0/\sin i) - J_2 3/2(r_\mathrm{E}/a)^2\sqrt{\mu/a^3}\cos i \tag{3.88}$$

$$dm/dt = -T/c \tag{3.89}$$

where c is the exhaust effective velocity. The same optimal control law, applied in the previous analysis, is used here. The Hamiltonian is the calculated as:

$$H = 2T/m\pi\sqrt{a/\mu}(\pi\lambda_\mathrm{a} a\cos\beta + \lambda_\mathrm{i}\sin\beta\cos\theta_0 + \lambda_\Omega\sin\beta(\sin\theta_0/\sin i)) - \lambda_\Omega J_2 3/2(r_\mathrm{E}/a)^2\sqrt{\mu/a^3}\cos i - \lambda_\mathrm{m}T/c \tag{3.90}$$

and the Euler-Lagrange equations are:

$$d\lambda_\mathrm{a}/dt = -3\lambda_\mathrm{a}T/m\sqrt{a/\mu}\cos 7beta - \lambda_\mathrm{i}(T/\pi m\sqrt{a/\mu}\sin\beta\cos\theta_0) - \lambda_\Omega(T/\pi m\sqrt{a/\mu}\sin\beta(\sin\theta_0/\sin i) + J_2 21/4(r_\mathrm{E}/a)^2\sqrt{\mu/a^5}\cos i) \tag{3.91}$$

$$d\lambda_\mathrm{i}/dt = \lambda_\Omega(2T/\pi m\sqrt{a/\mu}\sin\beta(\sin\theta_0/\sin i))\cos i + J_2 3/2(r_\mathrm{E}/a)^2\sqrt{\mu/a^3}\sin i \tag{3.92}$$

$$d\lambda_\Omega/dt = 0 \tag{3.93}$$

$$d\lambda_\mathrm{m}/dt = T/m\sqrt{a/\mu}(\lambda_\mathrm{a} a\cos\beta + \lambda_\mathrm{i}2/\pi\sin\beta\cos\theta_0 + \lambda_\Omega 2/\pi\sin\beta(\sin\theta_0/\sin i) \tag{3.94}$$

The control variable are β, θ_0 and T (thrust magnitude). The Hamiltonian derivative with respect to θ_0 is nullified in order to obtain:

$$\tan\theta_0 = \lambda_\Omega/(\lambda_\mathrm{i}\sin i) \tag{3.95}$$

the same method is applied with respect to β in order to find:

$$\tan\beta = \lambda_{\mathrm{i}}\cos\theta_0 + \lambda_\Omega(\sin\theta_0/\sin i)/(\pi a\lambda_{\mathrm{a}}) \tag{3.96}$$

The optimal control law applied must maximize the Hamiltonian in agreement with *Pontryagin's Maximum Principle* and the correct quadrant must be selected: $\cos\beta$ must have the same sign as λ_{a} and$\sin\beta$ as $\lambda_{\mathrm{i}}\cos\theta_0 + \lambda_\Omega(\sin\theta_0/\sin i)$.
Assuming a positive value of $\sin\beta$ and correspondingly the right quadrant to obtain:

$$\sin\beta = \Lambda/\sqrt{\Lambda^2 + (\pi a\lambda_{\mathrm{a}})^2} \tag{3.97}$$

$$\cos\beta = \pi a\lambda_{\mathrm{a}}/\sqrt{\Lambda^2 + (\pi a\lambda_{\mathrm{a}})^2} \tag{3.98}$$

$$\sin\theta_0 = \lambda_\Omega/(\Lambda\sin i) \tag{3.99}$$

$$\cos\theta_0 = \lambda_{\mathrm{i}}/\Lambda \tag{3.100}$$

Since the Hamiltonian magnitude is linear with respect to the thrust magnitude, it can be rewritten as:

$$H = TS_{\mathrm{F}} - \lambda_\Omega J_2 3/2(r_{\mathrm{E}}/a)^2\sqrt{\mu/a^3}\cos i \tag{3.101}$$

where $\mathrm{S_F}$ represents the *Switching function* and it is defined as:

$$S_{\mathrm{F}} = 2/\pi m\sqrt{a/\mu}\sqrt{(\pi a\lambda_{\mathrm{a}})^2 + \lambda_{\mathrm{i}}^2 + (\lambda_\Omega/\sin i)^2} - \lambda_{\mathrm{m}}/c \tag{3.102}$$

the *switching function* dictates the state of thruster, since when $\mathrm{S_F}>0$ the engine must be turn on and the opposite when $\mathrm{S_F}<0$. In the multiple-revolutions transfer the adjoint variables can be seen as influence functions, since they represents the derivative of the performance index with respect to a change of the corresponding variable. Adjoint variables have the same sign of the desired overall change of the corresponding variable, but locally could shown the opposite behavior.

3.5.3 Optimization

The optimal control law used in this study depends on the boundary conditions and on the performance index. Initial orbital elements a_0, i_0 are well defined while $\Omega_0 = 0$. The same is done for the target orbit with a_T, i_T and Ω_{T0}. Taking into account the $\mathrm{J_2}$ perturbation, the target RAAN varies by $\dot{\Omega}_{\mathrm{J2}}$.

The final time boundary conditions could be written as:

- a_f=a_t
- i_f=i_t
- $\Omega_f = \Omega_{T0} + \dot{\Omega}_{J2} t_f$

Since the purpose of the study is represented by finding the *minimum time solution* and the *maximum final mass solution*, boundary conditions should be modified according to the solution chosen.
In the case of minimum time solution, the boundary conditions are:

- H_f-$\lambda_\Omega \dot{\Omega}_{J2} t_f$=1
- $\lambda_{mf} = 0$

in this case the *switching function* is always positive and the engine is always turn on. Since the problem is homogeneus, the boundary condition on the Hamiltonian value could be replaced by specifying one of the initial values, in this case λ_Ω. Since the correct sign of the inital value must be chosen correctly in order to not have a negative flight time, λ_Ω sign is the same as the difference between inital and teaget RAAN.
In the case of maximum final mass solution, λ_{mf} must be equal to 1, the *switching function* can now assume negative values and the engine could be turned off in certain conditions. If the final time is specified then the boundary condition t_f is equal to k, otherwise H_f-$\lambda_\Omega \dot{\Omega}_{J2} t_f$=0 for free final time. In some cases a decrease of altitude is needed to vary the J_2 perturbation and in order to avoid an exceeding penetration of the atmosphere, a constrained optimization problem must be defined adding an altitude constrain (h_{lim}=200km). This leads to a three-arc structure for the maneuver. The spacecraft follows an optimal control law in the initial and final arc from t_0 to t_1 and from t_2 to t_f. In the middle arc, from t_1 to t_2, the spacecraft flies at a fixed altitude ($\beta = 90°$). This maneuver could be carried out adding a new boundary condition a_2=r_E+h_{lim}.
An important observation came from the Euler-Lagrange equations, when a pure change of RAAN is required with the same initial and traget orbit inclination, the maneuver is not performed at constant inclination. For direct orbits, the derivatives of λi is positive, means that the adjoint variable, referred to the inclination, must be initially negative (i is reduced) and then turns positive (i increases till the initial value). That represents the cost

dependence on inclination, that's smaller when inclination low and orbit plane is closer to the equator.
The effect of J_2 appears when λ_Ω is not equal to zero. In case of a direct orbit and a RAAN increase, λ_a and λ_i are initially positive and then become negative: in other words, a and i both increase to reduce the negative drift cause by J_2, which contrasts the required RAAN change.

4 Single Target Solution

4.1 Introduction

The solution of low-thrust many-revolutions transfer optimization is obtained through an implemented FORTRAN script that uses the theory shown in the previous chapter. Through the utilization of an indirect method, once all boundary conditions have been defined, the script finds the *Minimum Time Solution* or the *Minimum Propellant Solutions*, based on the choice made. Once the script has converged and the best solution has been found, every variables trend is saved in a text file.

4.2 Results

First of all is necessary to define the initial conditions of the problem. it has been chosen for the initial orbit the following conditions:

- a=400km
- i=51°

Once initial conditions have been defined, both types of solution are studied.

4.2.1 Minimum Time Solution

As seen in chapter 3.5.3, in order to obtain the minimum time solution, the *switching function* is always positive and consequently engines are always turned on. For the first case, the following target conditions have been selected:

- $\Delta a = 100$ km
- $\Delta i = 0°$
- $\Delta\Omega = 10°$

The results are visualized through a MATLAB script, that generates trend-graphs over time for some variables. First the semimajor axis and inclination trends (figure 4.1) are studied:

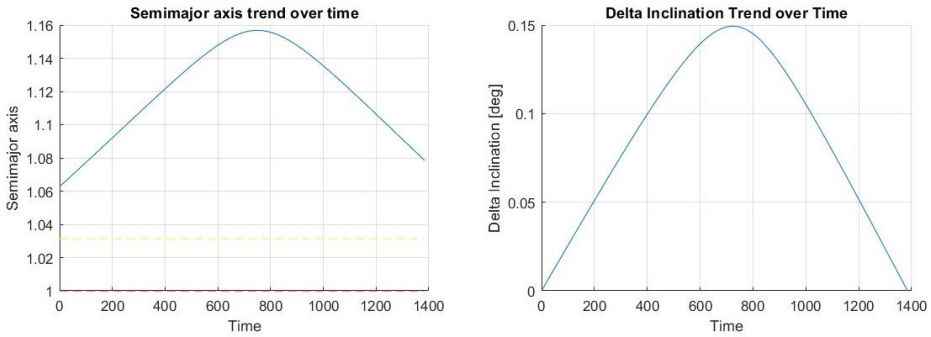

Figure 4.1: Semimajor axis and inclination trends over time

In Figure 4.1 it's possible to see how semimajor axis and inclination change over time. First of all, taking into account equation [3.62], it's possible to notice that the drift of $\dot{\Omega}$ is inversely proportional to the cube of the semimajor axis and proportional to the cosine function of inclination. Since target orbit has an Ω_T greater than 10° and the Ω drift is towards negative values, in order to get nodes closer, J_2 effect must be reduced and $\dot{\Omega}$ is decreased. In order to take advantage of J_2 effect, semimajor axis is increased way over the target value to get a reduction of J_2 effect. Since initial orbit has a lower altitude than the target one, at first, *nodes* are moving away from each other and J_2 effect is counterproductive. This disadvantageous behavior shows up until the altitude of the initial orbit reaches the one of the target orbit, then the effect become advantageous and nodes begins to approach. At the same time, an increase of inclination reduces the J_2 effect and, although the influence is much weaker, reflects the semimajor axis behavior. In figure 4.2 the distance between nodes can be visualized. It's

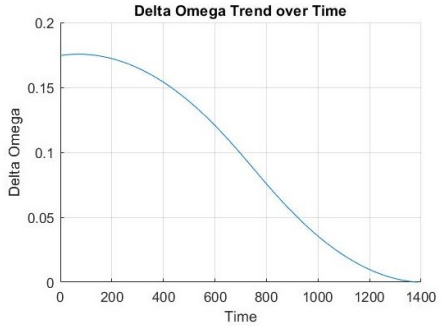

Figure 4.2: $\Delta\Omega$ trend over time

possible to notice the behavior of J_2 effect that causes a first increase of $\Delta\Omega$ that reaches a maximum value at t=108 and then decrease continuously until it becomes zero. The maximum value of $\Delta\Omega$ does not correspond exactly to the point where the spacecraft reaches the target altitude, but is placed just before, due to the contribution of inclination change.
Since engines are always on, mass fuel consumption is decreasing linearly as shown in figure 4.3.

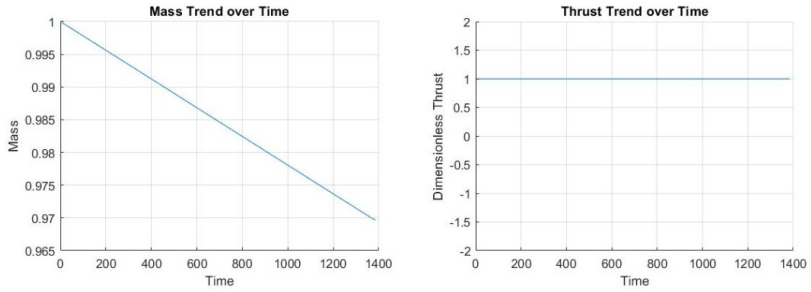

Figure 4.3: thrust and mass trend over time

For further considerations, a new case is considered here. This time target conditions are defined as follows:

- Δa = 100 km
- Δi = 0°
- $\Delta\Omega$ = -10°

as done for the previous case, here follows, in figure 4.4, the visualization of semimajoraxis and inclination trends:

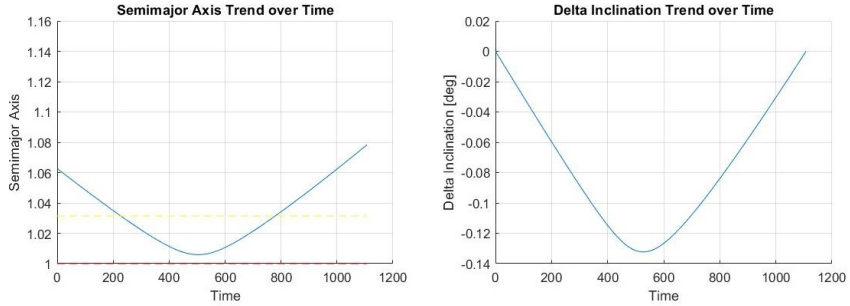

Figure 4.4: Semimajor axis and inclination trends over time

in this case, since $\Delta\Omega$ has a negative value, the J_2 effect need to be emphasized

in order to get nodes closer. The semimajor axis is reduced in order to increase $\dot{\Omega}$ and consequently emphasizing the J_2 effect. The inclination trend assume the same behavior of semimajor axis, as seen in the previous case.

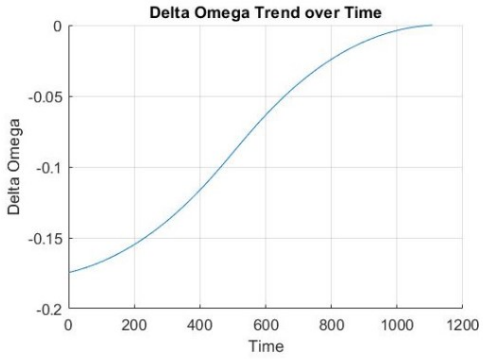

Figure 4.5: $\Delta\Omega$ trend over time

In figure 4.5, the $\Delta\Omega$ trend shows a different behavior with respect to the previous case, in fact it hasn't any point of maximum/minimum. This phenomenon could be explained easily. Since J_2 effect needs to be emphasized and the spacecraft at the initial point is at a lower altitude than the target, from the beginning nodes are getting closer and there is not a first moment of drawback. Since engines are always on, mass fuel consumption is decreasing linearly as shown in figure 4.6.

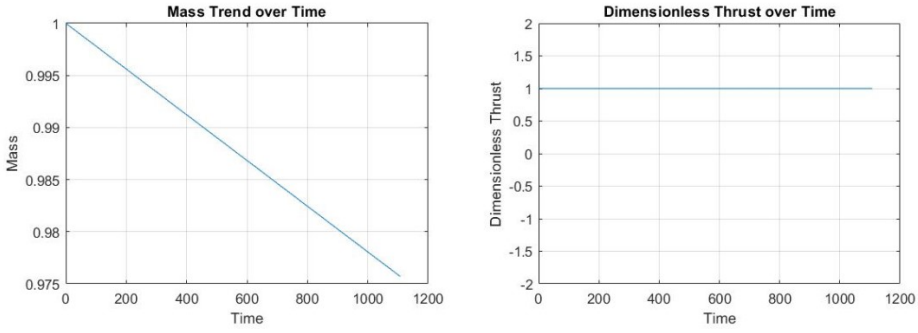

Figure 4.6: thrust and mass trend over time

As it is easy to see in figure 4.4, the spacecraft altitude decrease way below the altitude restrain that has been introduced in chapter 3.5.3, it is therefore necessary to modify the script used, introducing a three-phase transfer.

4.2.2 Three-phases transfer

In order to reach an acceptable solution, the new boundary conditions defined in chapter 3.5.3 must be taken into account. When the restrain is implemented, once the spacecraft reached the altitude of 200 km over the Earth's surface, β angle is fixed to a value of 90°, the second arc of the transfer takes place and the altitude is blocked. At a certain time β angle becomes free to vary again and altitude is not more fixed.
Considering the previous case, after the modification applied to the script, the new altitude trend could be visualize as follows:

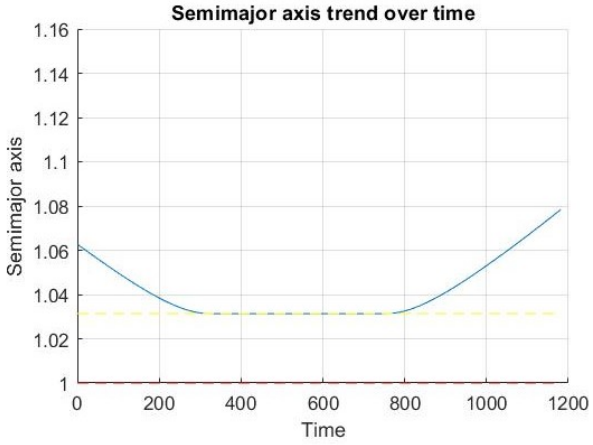

Figure 4.7: Altitude trend over time with constrain

The script finds the optimal solution even in terms of the initial and final time of the middle arc.

4.2.3 Maximum Final Mass Solution

Once the minimum time solution has been found, boundary conditions could be modified in order to reach the target with the minimum consumption, maximizing the benefical effect of J_2. The solution is carried out through a three phases transfer, with a middle arc in which engines are turned off (when the switching function becomes negative) and nodes gets closer passively through the only J_2 effect. As soon as the spacecraft reaches the optimal value of $\Delta\Omega$, engines are turned on again and the transfer is completed. The mission time is defined arbitrarily by the user and must be greater than the one get by the *minimum time solution*.

As seen in the previous section, the following target conditions have been selected:

- $\Delta a = 100$ km
- $\Delta i = 0°$
- $\Delta\Omega = 10°$
- $t_f = 2400$

In the figure below (figure 4.6) is shown a visualization of semimajor axis and inclination trends over time:

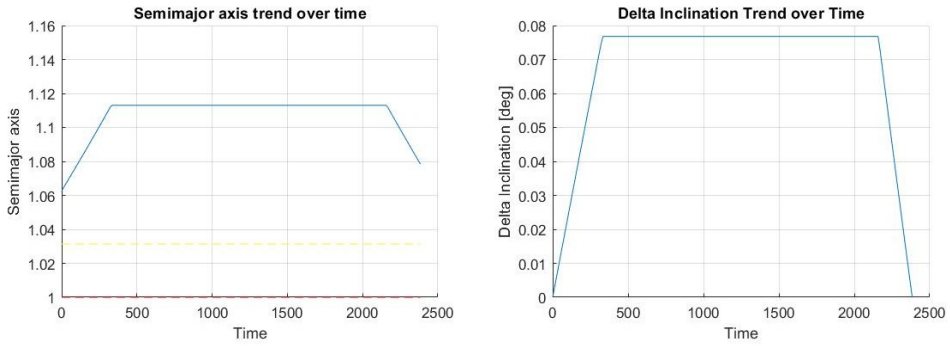

Figure 4.8: Semimajor axis and inclination trends over time

As shown in the figure above, the structure of the transfer is based on three phases in which, at a certain time, engines are turned off and the altitude and inclination keep fixed till engines are turned on again. The duration and the start time of the middle arc depends on the total mission time. Altitude and inclination general trends reflect the same behaviour of the *minimum time solution*, the only difference lies on the presence of the middle arc, dictated by engines status. In the next chapter, the influence of t_f on the solution will be studied.
In order to exploit the J_2 effect, before turning off engines, altitude an inclination must be increase enough to reach an optimal value of $\dot{\Omega}$, dictated by the total mission time.
This effect could be seen in the figure below (figure 4.9).

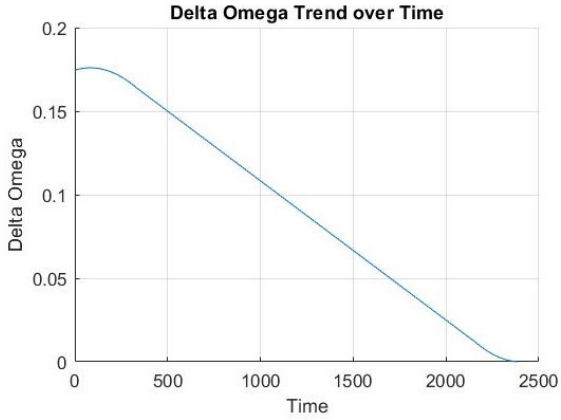

Figure 4.9: $\Delta\Omega$ trend over time

Once the first moment of nodes removal is overtaken, $\Delta\Omega$ continuously decreases. Even when engines are turned off, $\Delta\Omega$ is passively reduced without a fuel consumption, that could be seen in the mass trend, shown in the figure below (figure 4.10).

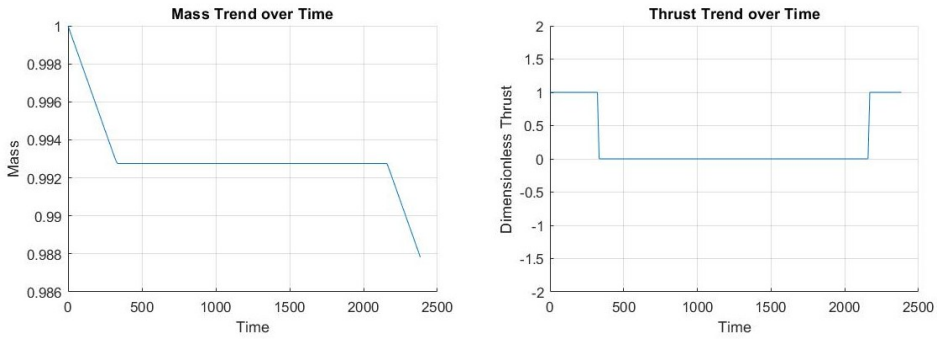

Figure 4.10: thrust and mass trend over time

During the middle arc engines are turned off and there is no fuel consumption, that leads to a steady mass trend over time. Thrust trend shows that when the *switching function* takes on a negative value thrust value gets zero and the middle arc takes place.
As done in the previous section, a similar case is analyzed here. The new target conditions are defined as follows:

- $\Delta a = 100$ km
- $\Delta i = 0°$

- $\Delta\Omega$ = -10°
- t_f=1650

In the figure below (figure 4.11) is shown a visualization of semimajor axis and inclination trends over time:

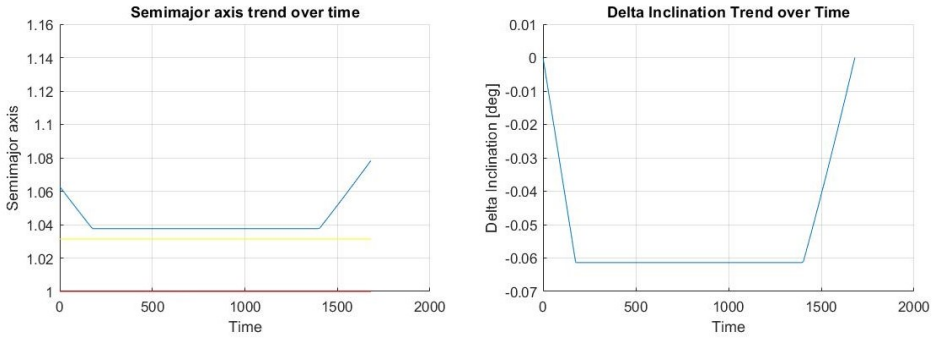

Figure 4.11: Semimajor axis and inclination trends over time

Similar consideration to the previous case, in terms of behavior, could be made. This time, though, J_2 effect is beneficial from the beginning and there is no need anymore to reduce altitude and inclination before turning off engines. Hypothetically the solution could be pushed to the limit with higher and higher total mission time, until the first arc disappears obtaining a two-phases transfer.

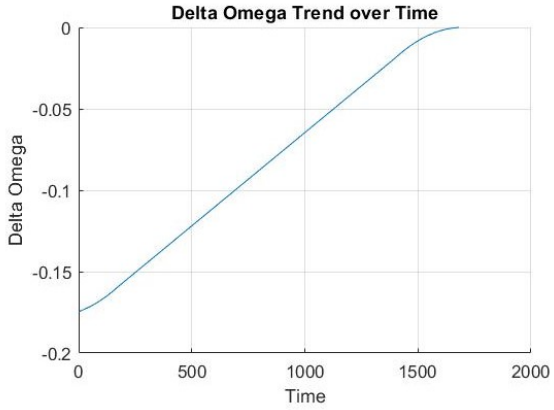

Figure 4.12: $\Delta\Omega$ trend over time

In figure 4.12 it's possible to seen the same trend of the previous case, where

$\Delta\Omega$ continuously decreases even without engines contribution.

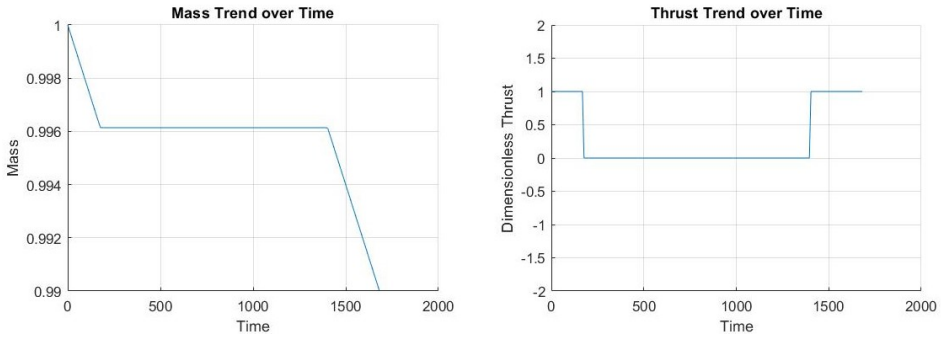

Figure 4.13: thrust and mass trend over time

In the figure above (figure 4.13) is shown mass and thrust trends that follows the same behavior of the previous case.

4.2.4 Confrontation

Once both types of solution have been defined, a confrontation between the two must be conducted. Introducing again the first case, the target conditions have been defined as follows:

- $\Delta a = 100$ km
- $\Delta i = 0°$
- $\Delta\Omega = 10°$

First of all a visualization of semimajor axis and inclination trends over time is shown in the figure below (Figure 4.14).

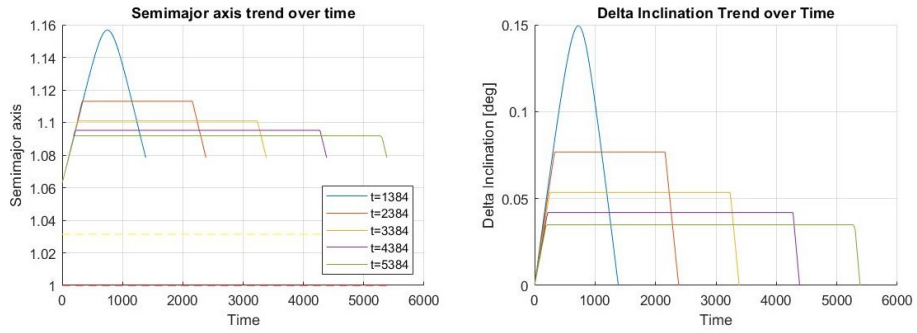

Figure 4.14: Semimajor axis and inclination trends over time

The minimum time solution is compared with the maximum final mass solution with different value of total mission time value, in particular four cases with a Δt of 1000 that, more or less, correspond to a 10 days time lapse.
It's easy to notice that as total mission time increases, the middle arc starts at lower time and with a lower altitude and inclination. This is due to the fact that with more time available to accomplish the transfer, it's acceptable to exploit a weaker J_2 beneficial effect, with a lower altitude and inclination, to reach the optimal value of $\Delta\Omega$ more slowly.
The main purpose of accept longer time lapse is to accomplish the transfer with a less fuel consumption and consequently a lower ΔV required. A table that encloses transfer costs for each total mission time is shown (table 4.1):

Table 4.1: Transfer costs for different mission time

Time	Final Mass	ΔV [km/s]
1384	0.9696	9.56647 10^{-2}
2384	0.9878	3.79771 10^{-2}
3384	0.9912	2.717544 10^{-2}
4384	0.9929	2.20958 10^{-2}
5384	0.9939	1.90957 10^{-2}
6384	0.9945	1.71045 10^{-2}
7384	0.9950	1.56835 10^{-2}
8384	0.9553	1.46171 10^{-2}
9384	0.9956	1.37869 10^{-2}
10384	0.9958	1.31219 10^{-2}

As shown in the table above, as the total mission time increases the final mass obtained increases and the ΔV required gets lower. This results confirm that if there is no restrain on total mission time, it's far convenient to lengthen times for a lower consumption. It's important to remember that long mission times correspond to a longer exposure to other types of perturbations that are not considered in this study.
It's now possible to study how $\Delta\Omega$ trend changes respect to total mission time (figure 4.15).

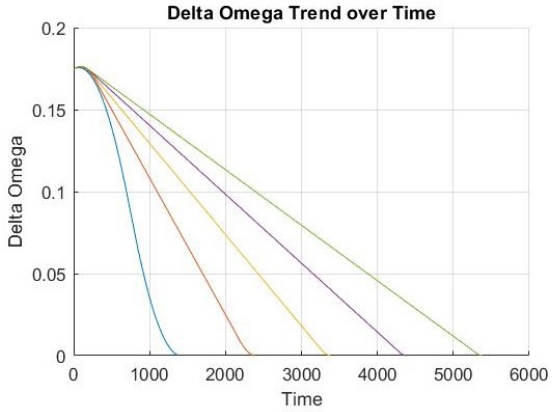

Figure 4.15: $\Delta\Omega$ trend over time

As shown in the figure above, as time increases the effect of J_2 gets weaker and the Ω variation becomes slower, since the same variation needs longer time. The free and passively change of Ω gets higher and higher as total mission time increases, whereas the active change needed decreases.

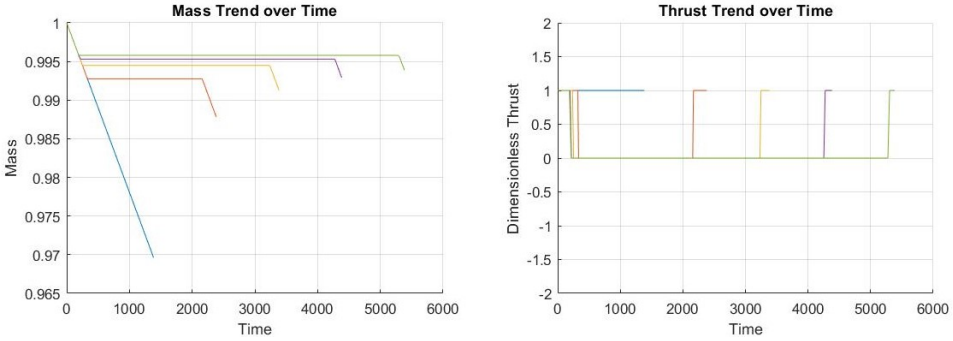

Figure 4.16: thrust and mass trend over time

According to table 4.1, the final mass obtained at the end of the transfer gets lower as total time increases (figure 4.16) and engines are turned off for a longer time lapse.
For further considerations, as done in the previous section, another case is taken into account. The new target conditions are defined as follows:

- $\Delta a = 100$ km
- $\Delta i = 0°$
- $\Delta\Omega$ = -10°

The minimum time solution is compared with the maximum final mass solution with different value of total mission time value, in particular four cases with a Δt of 500 that, more or less, correspond to a 5 days time lapse.

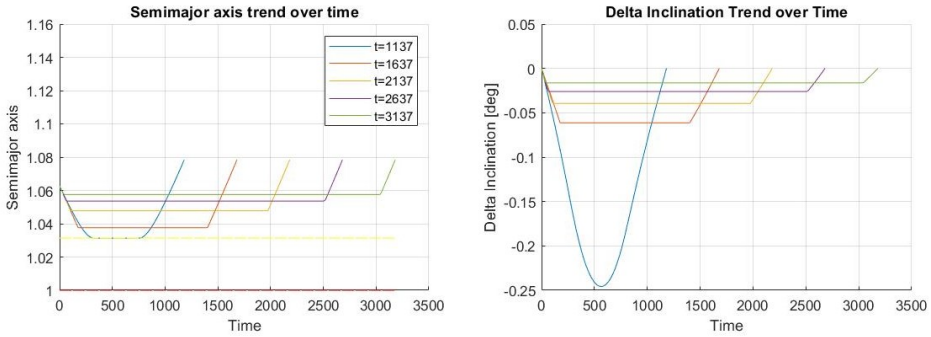

Figure 4.17: Semimajor axis and inclination trends over time

The same consideration of the previous case could be made to explain the behavior of these results. A table that encloses transfer costs for each total mission time is shown (table 4.2):

Table 4.2: Transfer costs for different mission time

Time	Final Mass	ΔV [km/s]
1137	0.9750	7.84063 10^{-2}
1637	0.9931	3.34681 10^{-2}
2137	0.9931	2.15796 10^{-2}
2637	0.9951	1.53818 10^{-2}
3137	0.9963	1.14747 10^{-2}
3637	0.9972	8.76126 10^{-3}

In this particular case, since the beneficial effect of J_2 start from the beginning of the transfer and consequently nodes are getting closer immediately, increasing total mission time enough leads to the disappearance of the first arc. This behavior is shown in figure 4.18, where the first arc in the altitude trend disappears for t_f=4200 and the dimensionless thrust start from zero (engines turned off).

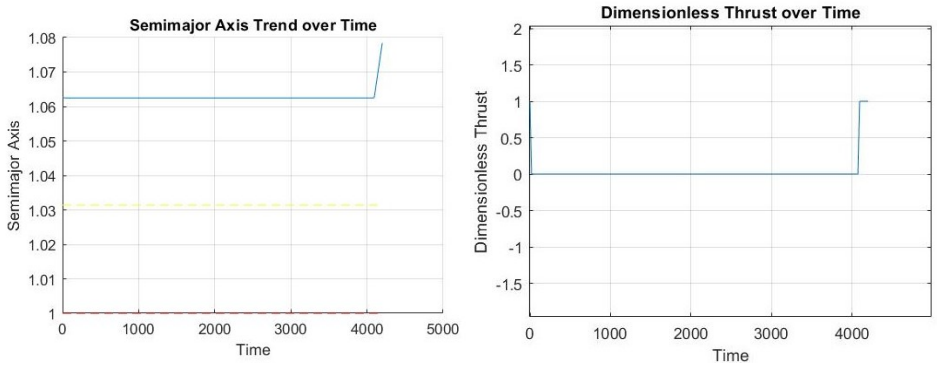

Figure 4.18: Semimajor axis and thrust trends for large total time mission

$\Delta\Omega$ trend has the same behavior as the previous case, with a lower rate of change as total mission time increases (figure 4.19).

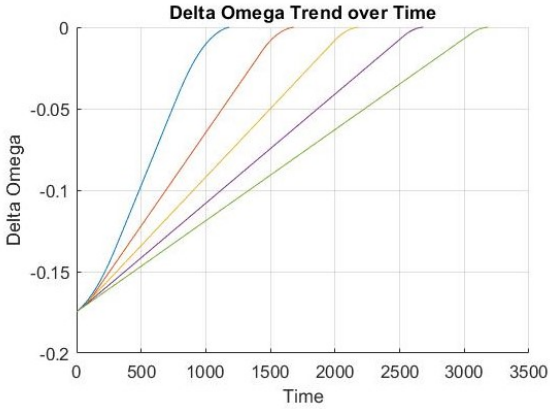

Figure 4.19: $\Delta\Omega$ trend over time

According to table 4.2, the final mass obtained at the end of the transfer gets lower as total time increases (figure 4.20) and engines are turned off for a longer time lapse.

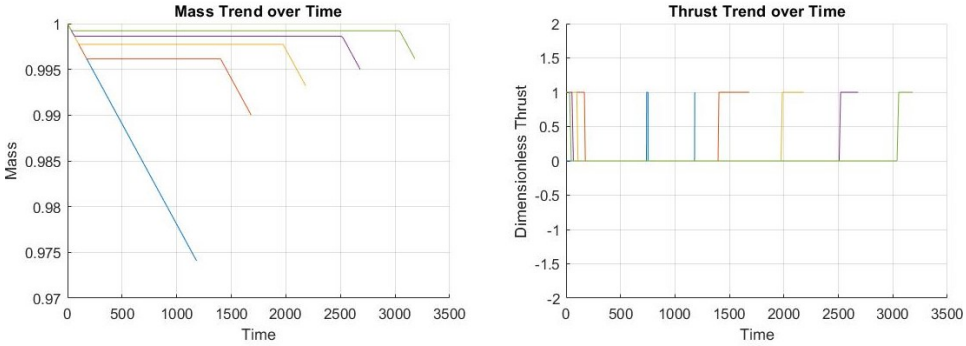

Figure 4.20: thrust and mass trend over time

4.3 Change in Initial Conditions

Once both types of solution has been studied, a change in initial conditions could be made in order to study the influence of initial inclination on the model. Two more cases are added, one with an inclination of 10° and another with an inclination of 97°, both with the same altitude of 400km.

4.3.1 High inclination Initial Orbit

In this section an high inclination initial orbit is analyzed, and the following conditions are taken into account:

- a=400km
- i=97°

With this particular characteristics the spacecraft is located on a *retrograde orbit*. In the following section, the *minimum time solution* and the *maximum mass solution* will be studied together. For the first case, the following target conditions are the same as the previous case, in order to obtain an effectively comparison:

- $\Delta a = 100$ km
- $\Delta i = 0°$
- $\Delta\Omega = 10°$

And, as done before, a visualization of semimajor axis and inclination trends are discussed (figure 4.21).

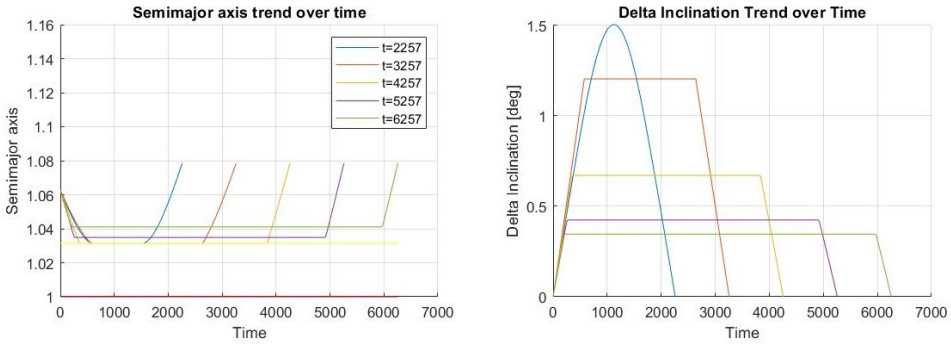

Figure 4.21: Semimajor axis and inclination trends over time

Even this time different total mission times are selected, with a $\Delta t = 1000$, in order to compare multiple solutions in terms of fuel mass consumption. The following results have been obtained (table 4.3):

Table 4.3: Transfer costs for different mission time

Time	Final Mass	ΔV [km/s]
2257*	0.9505	0.15752
3257*	0.9738	8.24098 10^{-2}
4257*	0.9831	5.29780 10^{-2}
5257	0.9869	4.07927 10^{-2}
6257	0.9893	3.34203 10^{-2}
7257	0.9910	2.81646 10^{-2}
8257	0.9922	2.42163 10^{-2}
9257	0.9932	2.11389 10^{-2}
10257	0.9940	1.86737 10^{-2}

The presence of "*" means that a three phases transfer has been applied to take the altitude constrain into account.
It's interesting to notice that, although the same target condition of the first case (chapter 4.2.1) are selected, there is a completely different behavior in terms of altitude trend (figure 4.22).

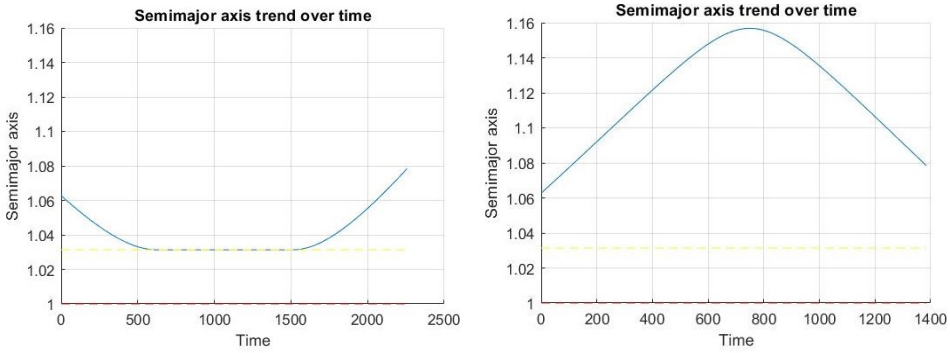

(a) i_0=97° (b) i_0=51°

Figure 4.22: Semimajor axis trend for different initial inclinations

This difference could be explained through the equation [3.62], where the drift of Ω depends on inclination and altitude. Since $\dot{\Omega}$ is directly proportional to the cosine function, when inclination goes over 90° the sign of the equation change. When this condition occurs, the J_2 effect has an opposite effect on the orbit and the spacecraft behaviour must change. In this particular case, since J_2 effect must be reduced, altitude is lowered and inclination is increased in order to raise the value of the cosine function. Although the inclination trend of this case and the one with i_0=51° seems similar, this has an opposite effect on $\dot{\Omega}$, since over 90° an increase of inclination means a raise of the cosine function, whereas, below 90°, an increase of inclination leads to a decrease of the cosine function.

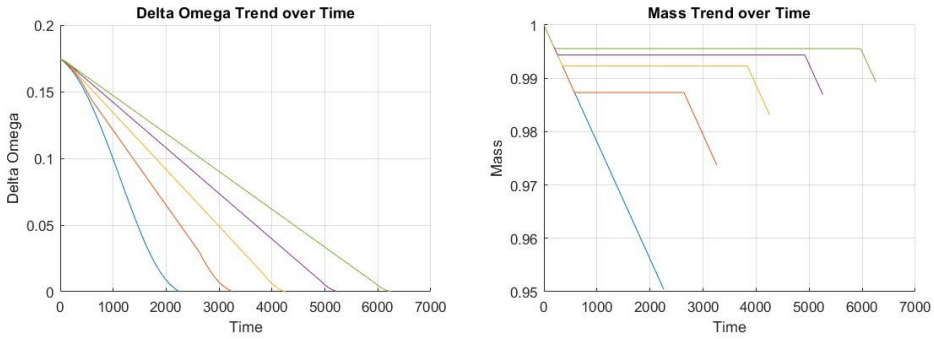

Figure 4.23: $\Delta\Omega$ and Dimensionless Thrust trends over time

As shown in the figure above (figure 4.23), $\Delta\Omega$ and Dimensionless Thrust trends over time has the same behavior as the previous cases, so there is no

need for further considerations.

4.3.2 Low Inclination Initial Orbit

In this section an high inclination initial orbit is analyzed, and the following conditions are taken into account:

- a=400km
- i=10°

Since inclination is lower than 90°, the orbit is *direct* and the following target conditions are selected:

- $\Delta a = 100$ km
- $\Delta i = 0°$
- $\Delta\Omega = 10°$

The semimajor axis and inclination trends could be visualized as follows (figure 4.25):

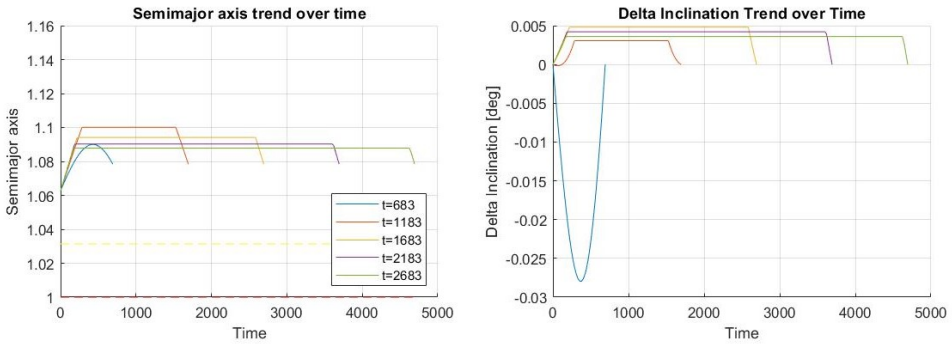

Figure 4.24: Semimajor axis and inclination trends over time

Different total mission times are selected, with a $\Delta t = 1000$, in order to compare multiple solutions in terms of fuel mass consumption. The following results have been obtained (table 4.4):

Table 4.4: Transfer costs for different mission time

Time	Final Mass	ΔV [km/s]
683	0.9850	4.68378 10^{-2}
1183	0.9874	3.93877 10^{-2}
1683	0.9898	3.18681 10^{-2}
2183	0.9914	2.66387 10^{-2}
2683	0.9926	2.30806 10^{-2}
3183	0.9934	2.05616 10^{-2}
3683	0.9940	1.87005 10^{-2}
4183	0.9944	1.73750 10^{-2}
4683	0.9948	1.61503 10^{-2}
5183	0.9951	1.52414 10^{-2}

Unlike what it has been seen in the previous chapter for a direct orbit, the behavior shown in the figure above is quite different. The altitude trend changes when the maximum mass solution is applied. The spacecraft, when the total mission time is raised for an exploit of J_2 effect, increases its altitude way over the one reaches with the minimum time solution, a phenomenon that didn't show up in the previous cases (figure 4.26).

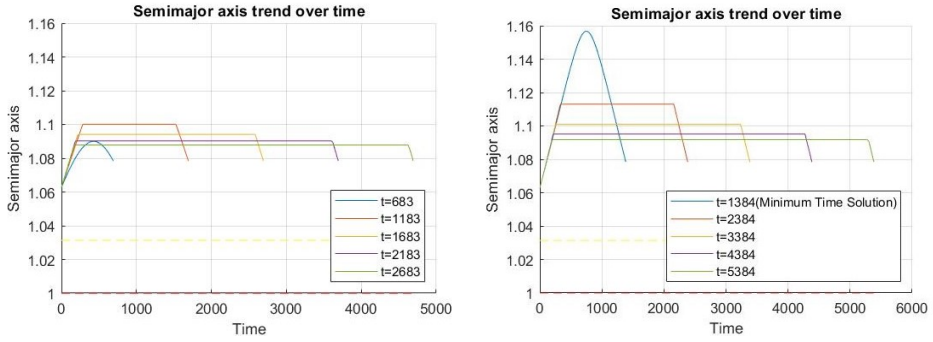

(a) i_0=10° (b) $i\{ped0$=51°

Figure 4.25: Semimajor axis trends comparison

As shown in the figure above, in order to accomplish the minimum time maneuver with the same target conditions, the spacecraft with an initial inclination of 10° reaches a low altitude with respect to the other, this fact is due to the stronger J_2 effect that is exercised on lower inclination orbit,

since $\dot{\Omega}$ is proportional to the cosine function of the inclination and the cost of RAAN change is lower for obit near the equator. This effect leads to a quicker maneuver with a lower fuel consumption with respect to the previous case.
Since the minimum time solution has a very low maximum altitude, when maximum final mass solution is taken into account, the altitude reaches by the middle arc, when engines are turned off, is way higher in order to exploit only J_2 effect to get nodes closer and find the optimal solution (figure 4.27).

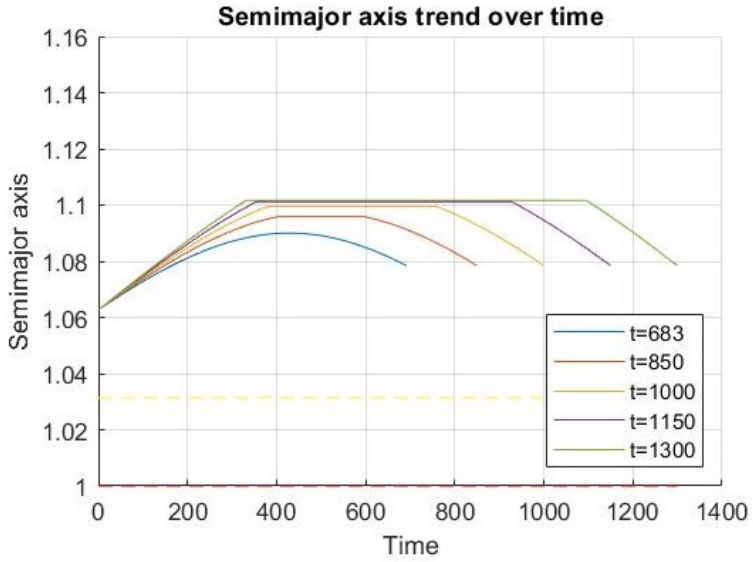

Figure 4.26: Semimajor axis trends over time for low inclination orbit

With low increases of total time, the middle arc initial altitude keeps increasing. When total time is increased enough, altitude stops increasing and the middle arc start before with a lower altitude, this is due to an higher time lapse available to exploit the J_2 effect that could be weaker (figure 4.27).
In conclusion, as it's possible to see in table 4.4, the maximum final mass solution is convenient with respect to the minimum time solution only for high total mission time, and the gain obtained is lower with respect to the previous case with i_0=51° (table 4.1).

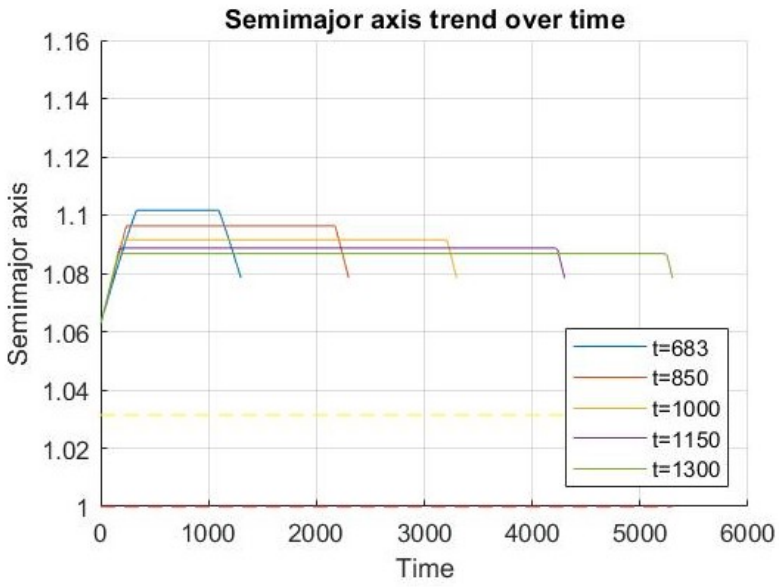

Figure 4.27: Semimajor axis trends over time for low inclination orbit

The other discrepancy with respect to the previous case is the different behavior of the inclination trend. The minimum time solution has a inclination trend opposite to the case of i_0=51°, although both are direct orbits (figure 4.28)

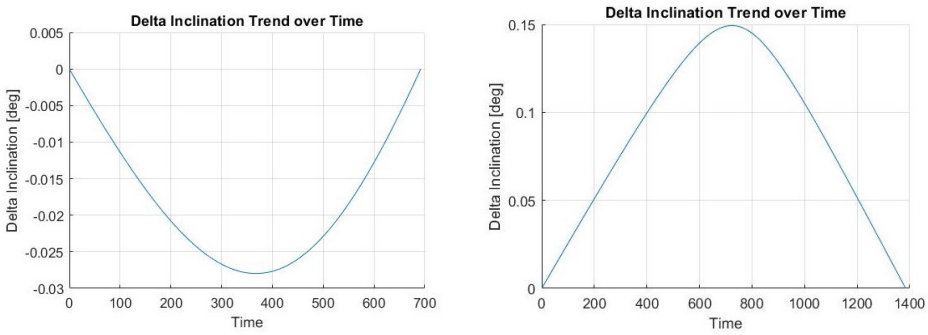

(a) i_0=10° (b) i_0=51°

Figure 4.28: Inclination trends comparison

This particular behavior is due to the low inclination of the initial orbit, in fact cost of RAAN change depends on the value of inclination and in particular, RAAN cost change is lower for orbit near equator. This dependency

could be seen in equation [3.68] where RAAN cost change is proportional to the sine function of inclination and this dependency is stronger for low inclination, since cost variation is proportional to the cosine function of inclination.
Following this behavior, at i_0=10° the optimal solution corresponds to a decrease of the inclination, even if it means a disadvantage in terms of J_2 effect. In fact an increase of altitude leads to a reduction of J_2 effect, whereas a decrease of inclination leads to an emphasizing of it.
This tendency appears for the minimum time solution and seems to fade for higher total mission time (figure 4.29).

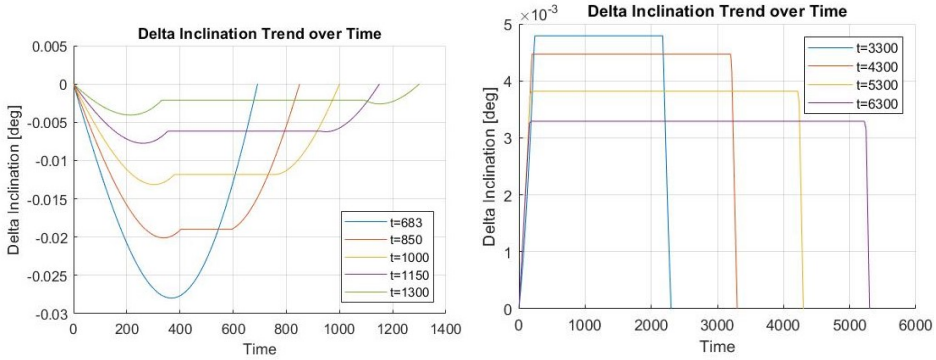

Figure 4.29: Inclination trend over different total mission time values

This is due to the fact that for low time mission, RAAN change is obtained mainly by an active use of thrust and in order to reduce the total cost, inclination is reduced. As total time increases, RAAN change is obtained more and more passively, exploiting J_2 effect, with all engines turned off, and a reduction of i is not more required. The influence of initial inclination on RAAN change could be seen in the following table (table 4.5):

Table 4.5: Transfer costs for different initial inclination values

i_0	Minimum time	Final Mass	Δ V [km/s]
98°	2257	0.9505	0.15752
51°	1384	0.9696	$9.56647\ 10^{-2}$
10°	683	0.9850	$4.68378\ 10^{-2}$

As seen before, the cost of RAAN change is proportional to the sine function of inclination (equation [3.68]) and, consequently, for near polar orbit the

ΔV required is far lower with a less fuel consumption and a total mission time that gets shorter as time decreases.

4.3.3 Pure change of RAAN for multiple values of initial inclination between 0° and 97°

In this section, the influence of initial inclination on results will be discussed deeply. Unlike previous cases, both Δa and Δi will be put equal to zero, in order to achieve a pure change of RAAN maneuver. So, in summary, the new target conditions could be described as follows:

- $\Delta a = 0$ km
- $\Delta i = 0°$
- $\Delta\Omega = 10°$

As regards initial conditions, in order to get enough information to be discussed, multiple values of initial inclination are selected, adequately spaced within the range of 6 to 86 degree. The following analysis will be conducted taking into account only the minimum time solution, since including maximum final mass solution would lead to equal considerations. The semimajor axis and inclination trends could be visualized as follows (figure 4.30 and figure 4.31):

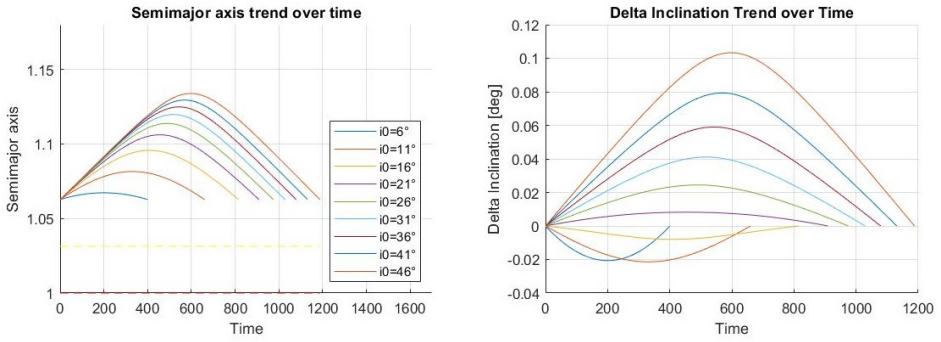

Figure 4.30: Semimajor axis and inclination trends over time

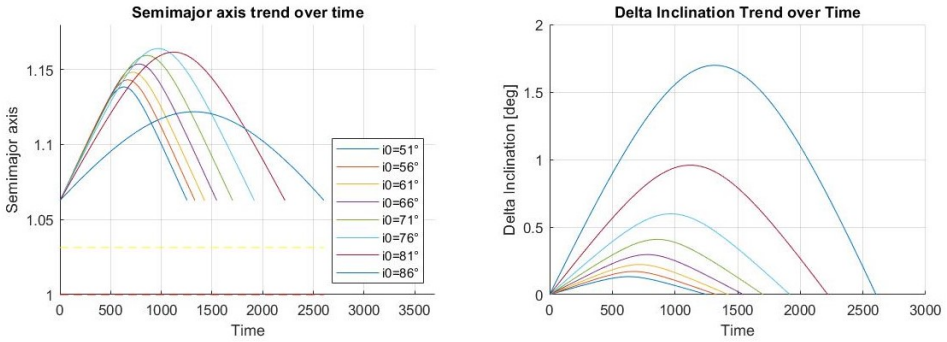

Figure 4.31: Semimajor axis and inclination trends over time

As seen in the previous sections, since the cost of RAAN change is proportional to the sine function of inclination, when initial orbit is near equatorial, the maneuver cost is very low and it is accomplished in a short amount of time. Since RAAN change is achieved actively, with engines contribution, when initial inclination is low and the cost variation due to inclination influence is strong (proportional to the $\cos i$), inclination value is decreased in order to get a reduction of maneuver cost, even though is counterproductive in term of J_2 effect exploiting. This behavior disappears as initial inclination increases and the general trend gets similar to the case in section 4.2.1.
As initial inclination increases, cost of RAAN change and total mission time raises. As regards the semimajor axis trend, the spacecraft reaches higher and higher altitude as initial inclination increases, until initial orbit gets near polar and the trend changes as shown in the figure below (figure 4.32).

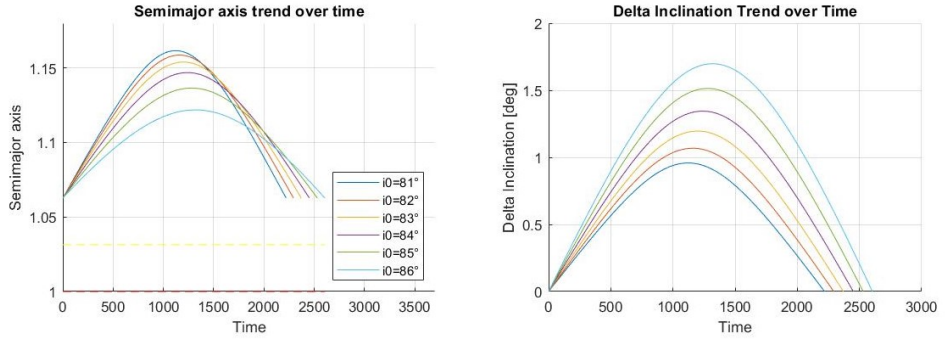

Figure 4.32: Semimajor axis and inclination trends over time

As regards for $\Delta\Omega$ trend, as initial inclination increases, the zero value is reached with longer amount of time (figure 4.33).

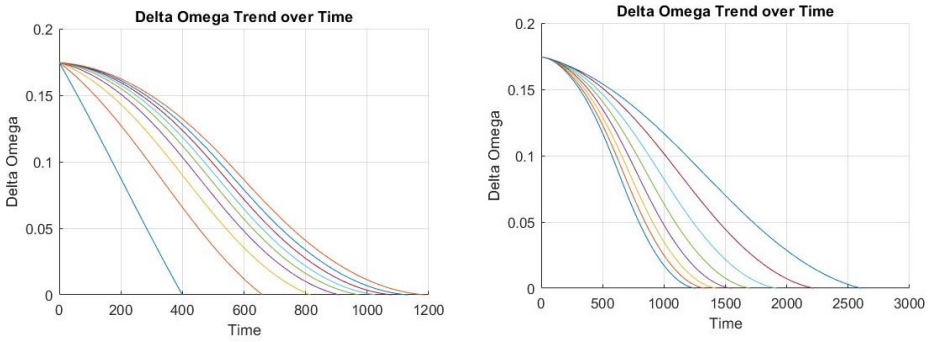

Figure 4.33: $\Delta\Omega$ trend over time for different initial inclination values

For further considerations, it's necessary to analyze deeply orbits near equator, from 1° to 5° of initial inclination values. This analysis is conducted apart from the previous in order to visualize better all results. First of all, initial inclination value is set to 1° and the semimajor axis and inclination trends are obtained (figure 4.33). It seems that semimajor axis trend is

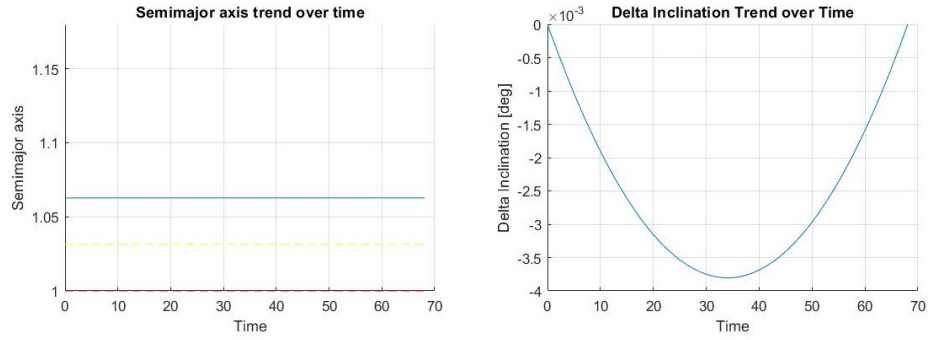

Figure 4.34: Semimajor axis and inclination trends over time

constant throughout all the maneuver while inclination change very little. Since initial inclination value is near the zero value and the cost of RAAN change is proportional to the sine function of inclination, the total cost and time of this maneuver is very small. In reality, using the proper value on y-axis, the typical trend could be visualized (figure 4.35)

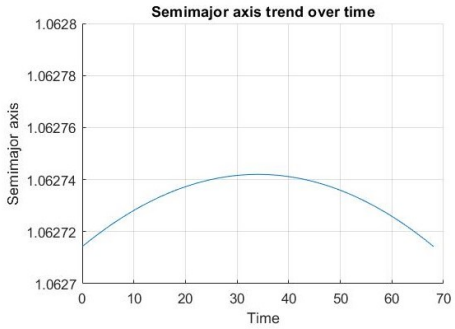

Figure 4.35: Semimajor axis trend of i_0=1°

It's now possible to visualize all results from 1° to 5° values of initial inclination, using again a different scale on y-axis (figure 4.36).

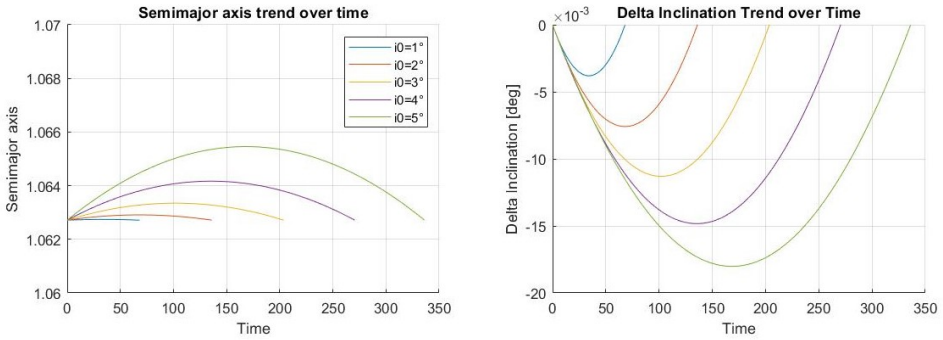

Figure 4.36: Semimajor axis and inclination trends over time

Since all initial orbits taken into account are near equatorial, total time mission and consumption are limited. Apart from the typical trend of the semimajor axis, for all values of initial inclination from 1° to 5°, inclination trends tend to decrease for a cost reduction due to the dependency of cost variation proportional to the cosine function of i.

As done for near equatorial orbits, a deeper analysis for initial inclination values that goes from 88° to 97° must be conducted. It's important to remember that increasing initial inclination values over 90° leads to obtain retrograde orbits. Since lots of initial inclination values are taken into account, a separated analysis for multiple groups will be conducted. The semimajor axis and inclination trends of i_0=88° and i_0=89° are visualized in the figure below (figure 4.37).

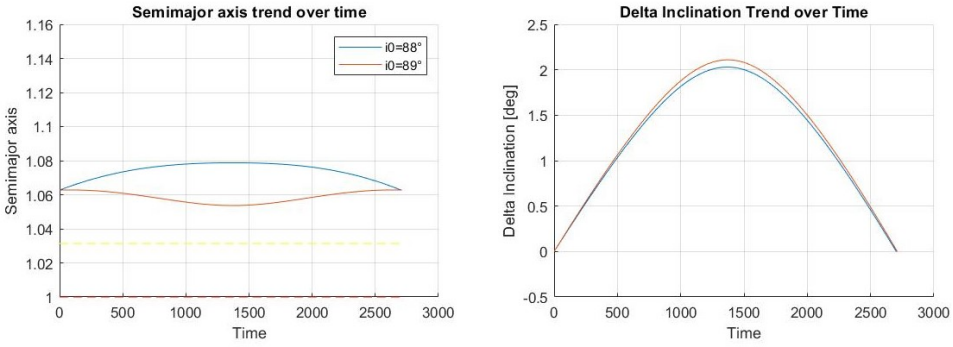

Figure 4.37: Semimajor axis and inclination trends over time

As regards i_0=88°, a typical trend of semimajor axis and inclination could be visualized, whereas i_0=89°, though is still a direct orbits, has a particular behavior due to the increase of inclination that changes the nature of the orbit (into a retrograde orbit) for a quite long time lapse. Since J_2 effect changes when inclination gets over 90°, the semimajor axis trend must change in order to exploit the gravitational drift of Ω. So, after a first increasing of altitude, the semimajor axis must decrease and then increase again when inclination decreases below 90°, when the orbit return to be direct again.

Initial inclination values of i_0=90°, i_0=91°, i_0=92° are now taken into account. The semimajor axis and inclination trends are shown in the figure below (figure 4.38).

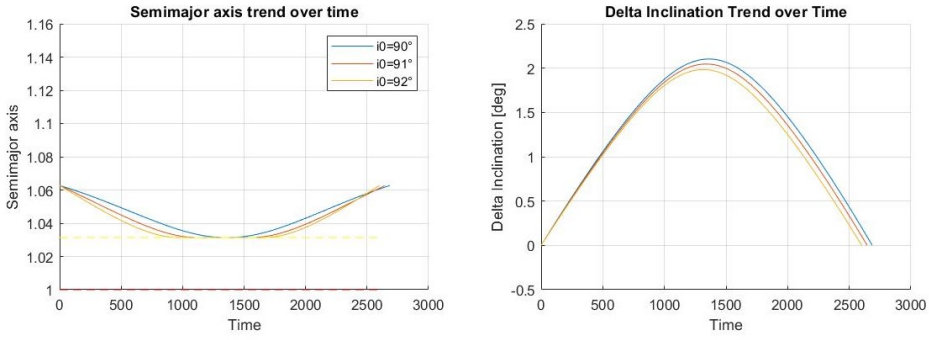

Figure 4.38: Semimajor axis and inclination trends over time

All these three orbits are retrograde so, since J_2 effect changes, from now on as initial inclination increases semimajor axis gets lower and lower, inclination reaches lower maximum level and total time mission starts decreasing. Since

there's a constrain on altitude that must be taken into account, when initial inclination gets over 90°, the minimum value of semimajor axis will always be equal to the h_{lim}, while the starting time of the middle arc decreases as initial inclination values get higher. It's the opposite for the end time of the middle arc.
As regards the remaining values of initial inclination (i_0=93°, i_0=94°, i_0=95°, i_0=96°, i_0=97°), same considerations could be done (figure 4.39).

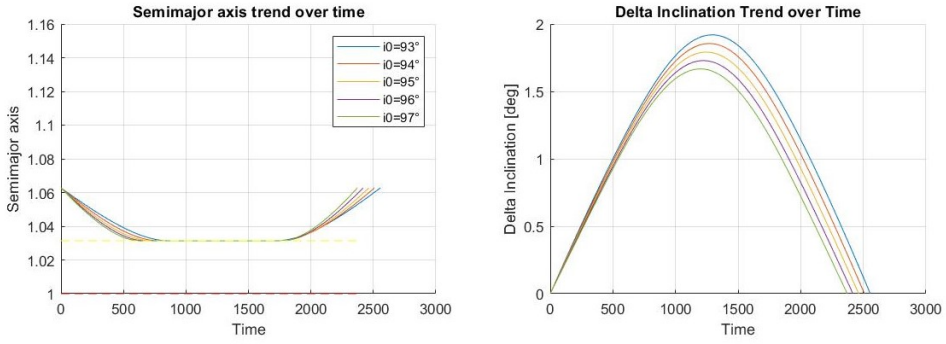

Figure 4.39: Semimajor axis and inclination trends over time

Could be interesting to visualize the maximum value of altitude and Δ inclination trend over all different initial inclination values (table 4.6). Since particular behavior appears for initial orbits near polar or near equator, smaller interval are used for inclinations that lie between 1° to 5° and 86° to 97°, whereas for inclinations from 6° to 86° a bigger Δ_0 has been chosen.

Table 4.6: Results for all initial inclination values

i_0	Δa_{max} [km]	Δi_{max} [deg]	t_f	m_f
1°	0.1767	-0.0038°	68	0.9985
2°	1.2564	-0.0075°	136	0.9970
3°	4.0424	-0.0112°	203	0.9955
4°	9.2639	-0.01482°	271	0.9941
5°	17.477	-0.0180°	336	0.9926
6°	28.939	-0.206°	400	0.9912
11°	119.77	-0.0214°	660	0.9855
16°	210.29	-0.00083°	815	0.9821
21°	276.61	0.0082°	908	0.9801
26°	325.32	0.0244°	974	0.9786
31°	363.54	0.0411°	1029	0.9774
36°	395.87	0.0590°	1079	0.9763
41°	425.18	0.0793°	1131	0.9752
46°	453.43	0.1033°	1188	0.9739
51°	482.04	0.1329°	1253	0.9725
56°	512.11	0.1711°	1331	0.9708
61°	544.49	0.2226°	1426	0.9687
66°	579.45	0.2962°	1546	0.9661
71°	615.57	0.4088°	1703	0.9626
76°	644.88	0.5980°	1917	0.9579
81°	629.94	0.9582°	2219	0.9513
86°	610.99	1.6978°	2604	0.9429
87°	581.15	1.8802°	2665	0.9415
88°	536.03	2.0294°	2703	0.9407
89°	469.94	2.1093°	2711	0.9405
90°	376.69	2.1026°	2686	0.9411
91°	102.25	2.0458°	2645	0.9420
92°	0.6246	1.9834°	2601	0.9429
93°	-200	1.9193°	2555	0.9439
94°	-200	1.8550°	2509	0.9450
95°	-200	1.7912°	2463	0.9460
96°	-200	1.7284°	2417	0.9471
97°	-200	1.6666°	2372	0.9480

The respective trend over initial inclination values could be visualized as follows (figure 4.40):

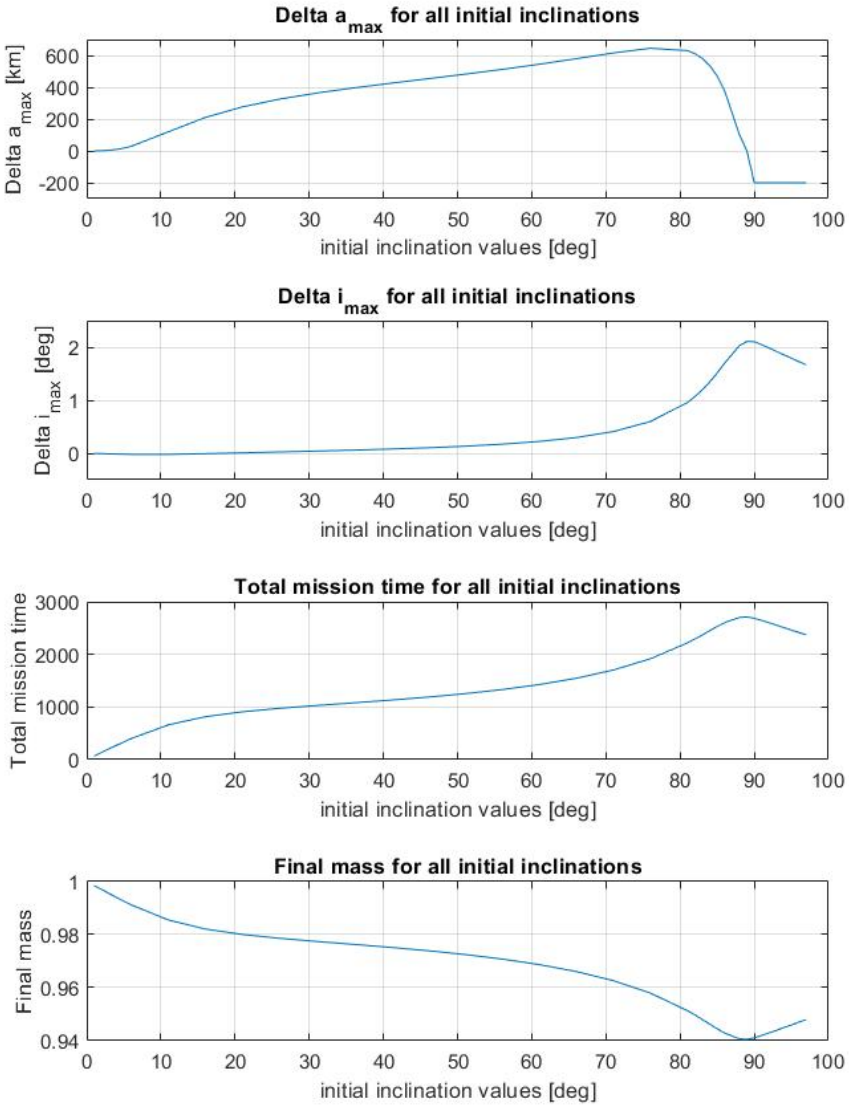

Figure 4.40: Trends for all initial inclination values

All considerations seen before are summarized in trends shown on figures above. In terms of final mass and total mission time, initial inclination values near polar and equatorial orbits seem to have a greater effect upon results than initial inclination values between 20 and 70 degree. Semimajor axis raises as initial inclination values increases till 75° and then starts decreasing. Δ inclination seems quite stable till 60° and then increases rapidly near polar orbit. As soon as initial inclination reach values near 90° total mission time and consumption start decreasing due to the change on J_2 effect and semimajor axis trend gets fixed on the constrain value. Although it's hard to see in the figure above, $\Delta i_{\max}$ assumes negative values from i_0=1° to i_0=16°, as shown in table 4.6, and changes to positive values at i_0=18.46° (figure 4.41).

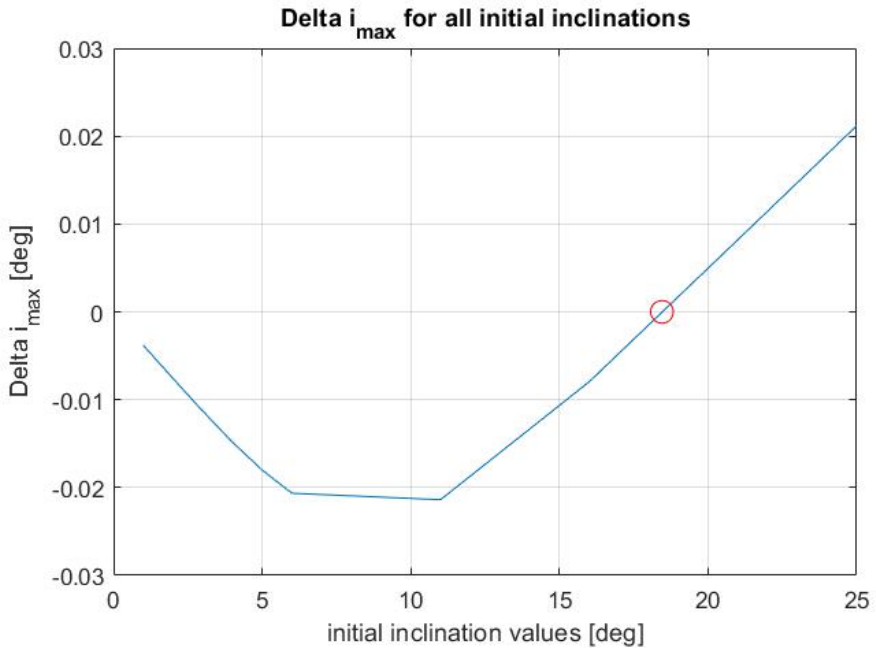

Figure 4.41: Δi values for initial inclination values from 0° to 25°

It's now possible to move forward and analyze a new case with a negative pure change of RAAN. The new target conditions could be summarized as follows:

- Δa = 0 km
- Δi = 0°
- $\Delta\Omega$ = -10°

As done before, an adequately spaced interval of initial inclination values is selected between 1° and 97° and minimum time solution only is taken into account. The semimajor axis and inclinations trends could be visualized as follows (figure 4.42 and figure 4.43):

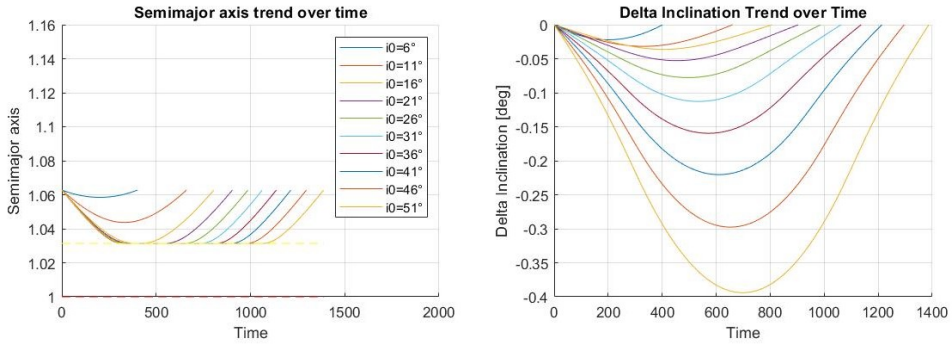

Figure 4.42: Semimajor axis and inclination trends over time

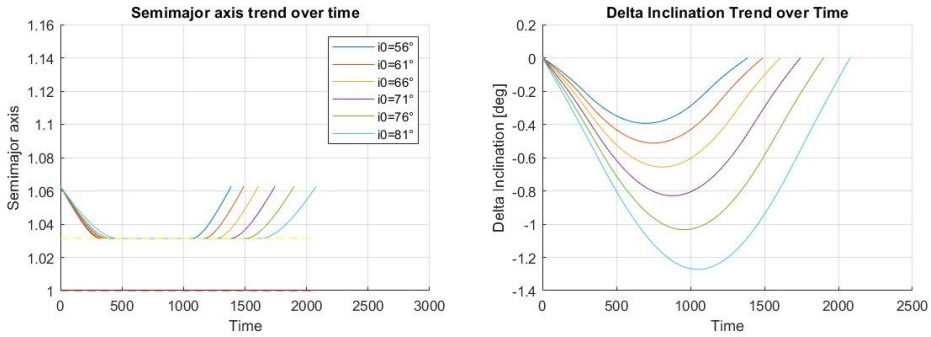

Figure 4.43: Semimajor axis and inclination trends over time

Same considerations as the previous case could be made. It's clear that this time, since a reduction of inclination is also needed to exploit the J_2 effect and get nodes closer, there won't be a trend change of inclination even for orbits near equator. A reduction of inclination value for low initial inclination orbits reduces the RAAN cost change (according to equation [3.68]) and, at the same time, since $\Delta\Omega$ is negative, a beneficial exploit of J_2 effect is obtained, unlike the previous case.

As regards semimajor axis trend, the minimum values is lower and lower as initial inclination values increases, but from i_0=16° the altitude constrain

takes place and Δa_{max} get fixed on h_{lim} value. As seen in the previous case, as initial inclination values increases, total mission time raises.

As done before, a focused analysis on near equatorial orbits is needed, for initial inclination values that goes from 1° to 5°. Here follows the semimajor axis and inclination trends over time (figure 4.44):

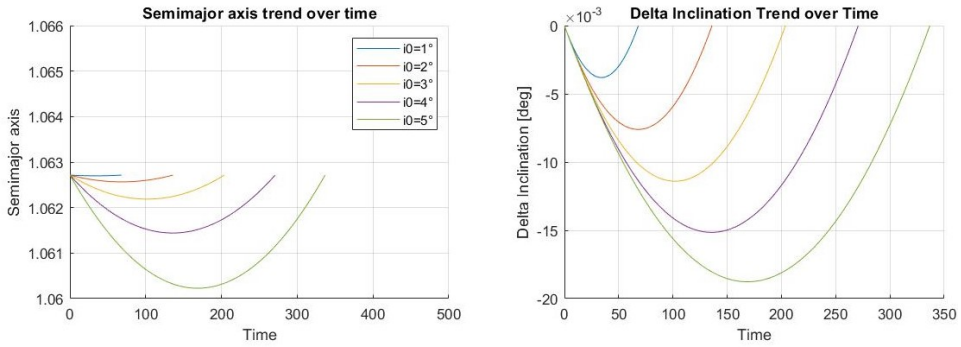

Figure 4.44: Semimajor axis and inclination trends over time

Since RAAN cost change is proportional to the sine function of i, fuel consumption and time needed are very low to the point that the i_0=1° solution seems to have a fixed altitude throughout all the maneuver. In reality the solution presents the typical trend but with an imperceptible variation, viewable only with a proper y-axis value (figure 4.45).

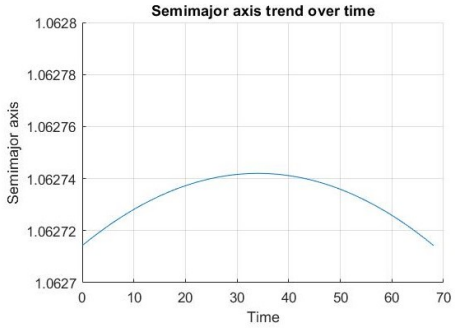

Figure 4.45: Semimajor axis trend of i_0=1°

It's now necessary to carry out a focused study on near polar orbits, where initial inclination values go from 88° to 97°. Initial inclination values of i_0=88°, i_0=89°, i_0=90°, i_0=91° are now taken into account. The semimajor axis and inclination trends are shown in the figure below (figure 4.46).

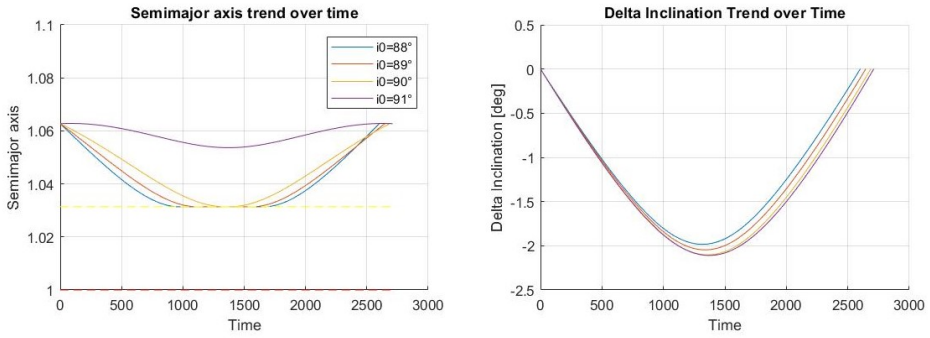

Figure 4.46: Semimajor axis and inclination trends over time

As shown in the figure above, from a certain value of initial inclination, the minimum value of altitude start raising till the constrain is no longer needed (i_0=91°). Unlike the previous case, i_0=89° and i_0=90° keep a typical trend and only i_0=91° is affected by a change of nature (from direct to retrograde and vice-versa). This is due to the fact that inclination decreasing trend maintains i_0=89° and i_0=90° direct orbit throughout all the maneuver, whereas i_0=91° starts being a retrograde orbit and becomes a direct one due to the inclination decreasing.

As regards the remaining values of initial inclination (i_0=93°, i_0=94°, i_0=95°, i_0=96°, i_0=97°), same considerations could be done (figure 4.47).

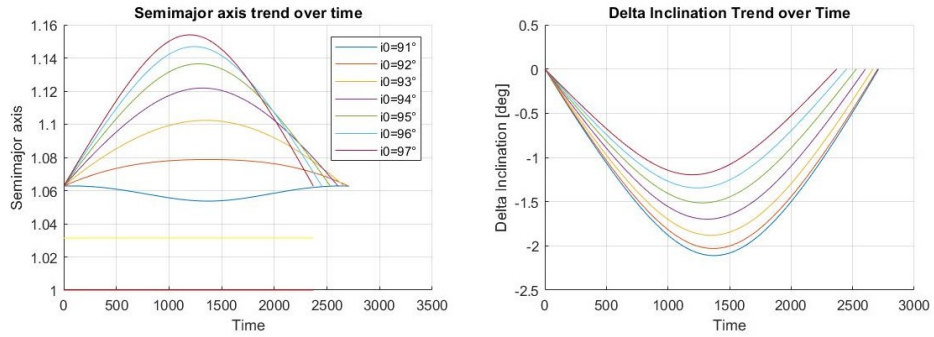

Figure 4.47: Semimajor axis and inclination trends over time

It's easy to see that when initial inclination values gets higher i_0=91°, as i_0 increases total mission time gets lower and minimum values of inclination reached gets higher. As done before, a visualization of the maximum value of altitude and Δ inclination trend over all different initial inclination values is made (table 4.6).

Table 4.7: Results for all initial inclination values

i_0	Δa_{max} [km]	Δi_{max} [deg]	t_f	m_f
1°	-0.5470	-0.0038°	68	0.9985
2°	-1.396	-0.0076°	136	0.9970
3°	-3.809	-0.0114°	203	0.9955
4°	-8.558	-0.0151°	270	0.9940
5°	-16.29	-0.0187°	336	0.9926
6°	-27.42	-0.0221°	400	0.9912
11°	-121.5	-0.0318°	660	0.9855
16°	-200	-0.0362°	805	0.9823
21°	-200	-0.0527°	903	0.9801
26°	-200	-0.0777°	986	0.9783
31°	-200	-0.112°	1062	0.9766
36°	-200	-0.159°	1136	0.9750
41°	-200	-0.220°	1213	0.9733
46°	-200	-0.297°	1296	0.9715
51°	-200	-0.393°	1387	0.9695
56°	-200	-0.512°	1490	0.9672
61°	-200	-0.656°	1608	0.9647
66°	-200	-0.829°	1743	0.9617
71°	-200	-1.033°	1899	0.9583
76°	-200	-1.272°	2078	0.9543
81°	-200	-1.546°	2283	0.9499
82°	-200	-1.606°	2326	0.9489
83°	-200	-1.666°	2371	0.9479
84°	-200	-1.728°	2416	0.9469
85°	-200	-1.791°	2462	0.9459
86°	-200	-1.855°	2508	0.9449
87°	-200	-1.919°	2555	0.9439
88°	-200	-1.983°	2601	0.9429
89°	-200	-2.045°	2645	0.9419
90°	-200	-2.102°	2686	0.9410
91°	0.1770	-2.109°	2710	0.9405
92°	101.8	-2.029°	2703	0.9406
93°	252.1	-1.880°	2665	0.9415
94°	376.2	-1.697°	2604	0.9428
95°	469.4	-1.513°	2530	0.9444
96°	535.5	-1.344 °	2450	0.9462
97°	580.7	-1.196°	2370	0.9479

The respective trend over initial inclination values could be visualized as follows (figure 4.48):

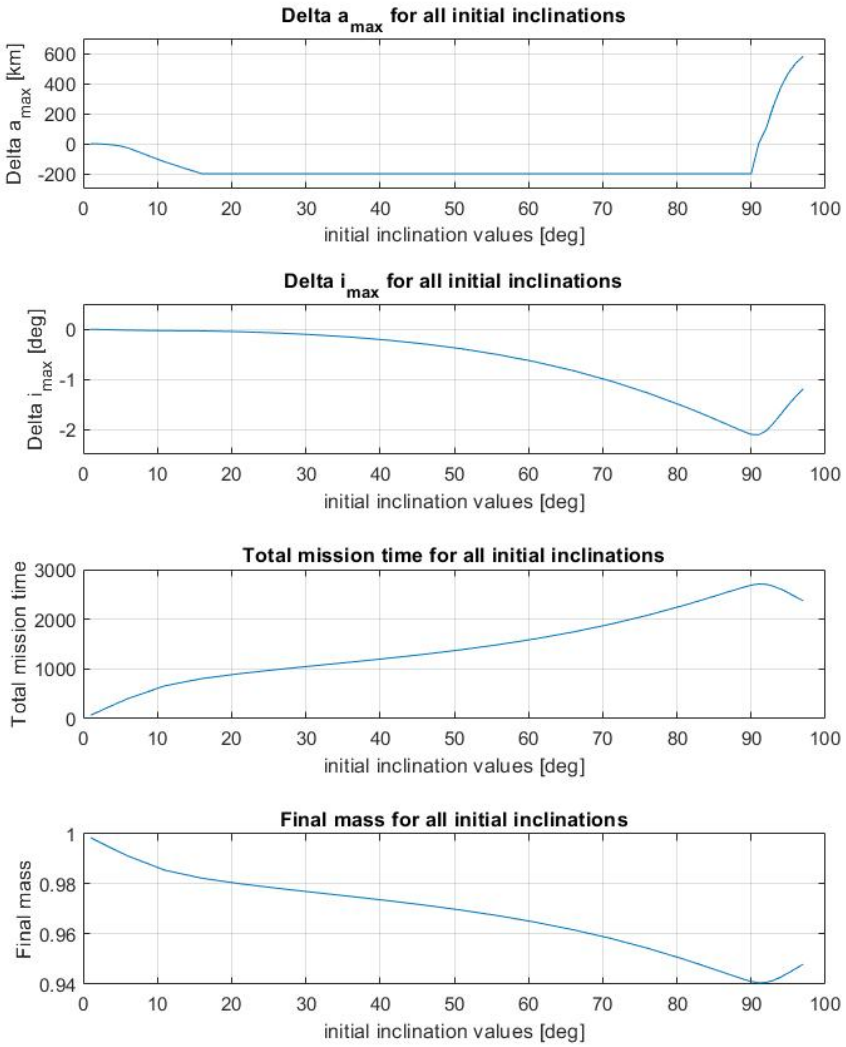

Figure 4.48: Trends for all initial inclination values

All considerations seen before are summarized in trends shown on figures above. Semimajor axis decreases as initial inclination values increases till altitude constrain takes place and then starts increasing once i_0 gets higher than 91°. Δ inclination seems quite stable till 90° and then increases rapidly when initial inclination gets higher than 90°. As soon as initial inclination

reach values near 90° total mission time and consumption start decreasing due to the change on J_2 effect.
In conclusion it's possible to visualize the confrontation between the two different trends (figure 4.49).

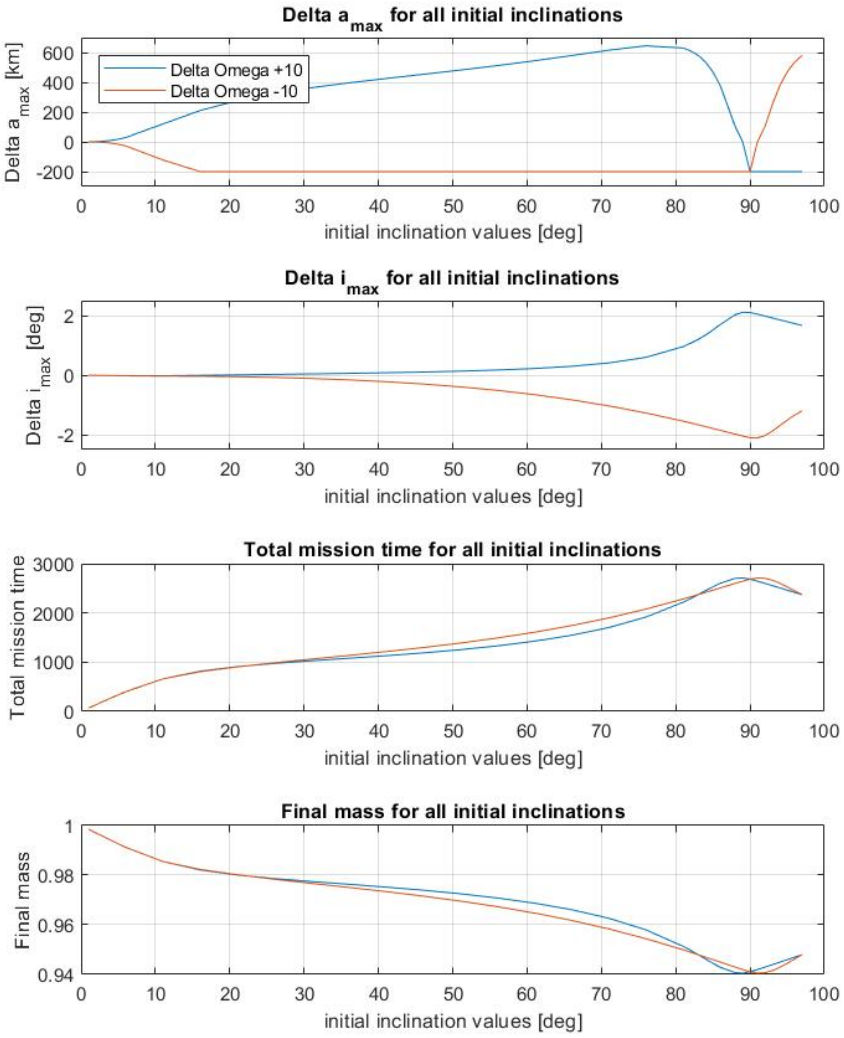

Figure 4.49: Confrontation between Trends for all initial inclination values

it's clear that semimajor axis and inclination trends would be symmetric with respect to the x-axis if it wasn't for the altitude constrain that play a huge role in the $\Delta\Omega = -10°$ solution.

4.3.4 Pure change of RAAN for multiple values of initial inclination between 97° and 180°

In this section, a deep analysis on pure RAAN change maneuver for retrograde orbits is taken into account. The target conditions could be described as follows:

- $\Delta a = 0$ km
- $\Delta i = 0°$
- $\Delta\Omega = 10°$

First of all, multiple values of initial inclination are selected, adequately spaced within the range of 97 to 167 degree. The semimajor axis and inclination trends could be visualized as follows (figure 4.50 and figure 4.51):

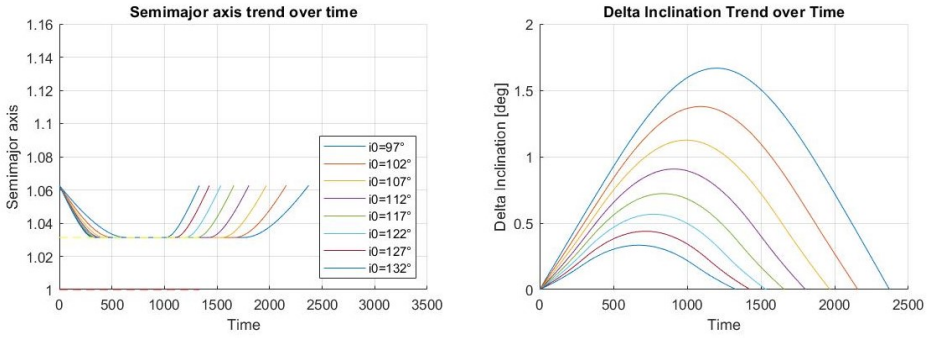

Figure 4.50: Semimajor axis and inclination trends over time

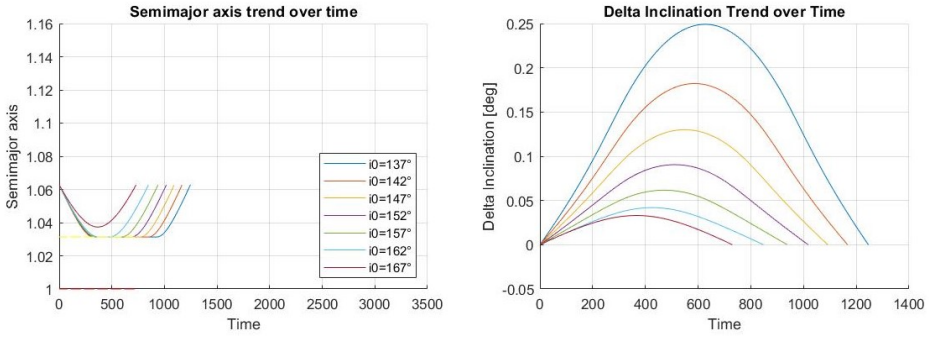

Figure 4.51: Semimajor axis and inclination trends over time

As seen in the previous sections, since the cost of RAAN change is proportional to the sine function of inclination, when initial orbit is near polar,

the maneuver cost is very high and it is accomplished in a long time lapse. As initial inclination time increases, the sine function of inclination starts decreasing and the same goes for the maneuver cost, consequently, total mission time decreases. As regards the semimajor axis trend, the spacecraft altitude is fixed on the constrain value of h_{lim} until initial inclination values get higher enough (i_0=167°). As initial inclination values increase, the minimum value of semimajor axis could be found at higher altitude values (figure 4.52). Δi values get lower as initial inclination values increase.

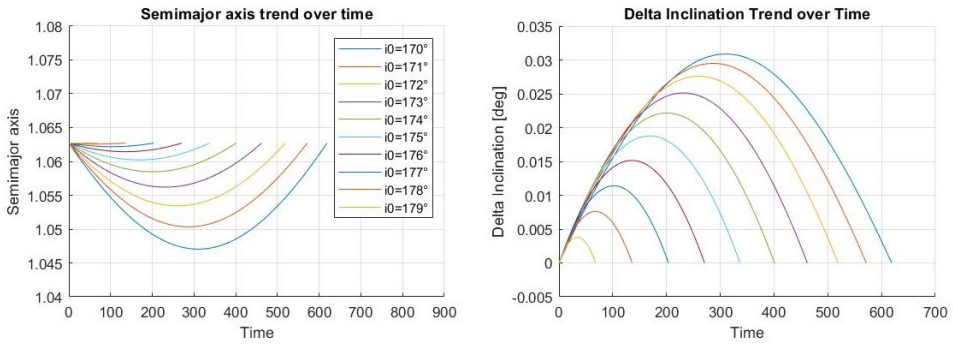

Figure 4.52: Semimajor axis and inclination trends over time

As done before, a visualization of the maximum value of altitude and Δ inclination trend over all different initial inclination values is made (table 4.8).

Table 4.8: Results for all initial inclination values

i_0	Δa_{max} [km]	Δi_{max} [deg]	t_f	m_f
97°	-200.0000	1.6667°	2371	0.9480
102°	-200.0000	1.3779°	2158	0.9527
107°	-200.0000	1.1249°	1968	0.9568
112°	-200.0000	0.9072°	1803	0.9604
117°	-200.0000	0.7222°	1660	0.9636
122°	-200.0000	0.5670°	1536	0.9663
127°	-200.0000	0.4386°	1427	0.9687
132°	-200.0000	0.3337°	1332	0.9708
137°	-200.0000	0.2491°	1246	0.9727
142°	-200.0000	0.1821°	1167	0.9744
147°	-200.0000	0.1300°	1092	0.9760
152°	-200.0000	0.0905°	1018	0.9777
157°	-200.0000	0.0617°	938	0.9794
162°	-200.0000	0.0419°	848	0.9814
167°	-161.5285	0.0330°	730	0.9840
170°	-99.8301	0.0309°	619	0.9864
171°	-78.8579	0.0295°	571	0.9875
172°	-59.0948	0.0276°	519	0.9886
173°	-41.5333	0.0251°	462	0.9899
174°	-26.9775	0.0221°	401	0.9912
175°	-15.8468	0.0188°	337	0.9926
176°	-8.1114	0.0151°	271	0.9941
177°	-3.3624	0.0114°	204	0.9955
178°	-0.9487	0.0076°	136	0.9970
179°	-0.0995	0.0038°	68	0.9985

The respective trend over initial inclination values could be visualized as follows (figure 4.55):

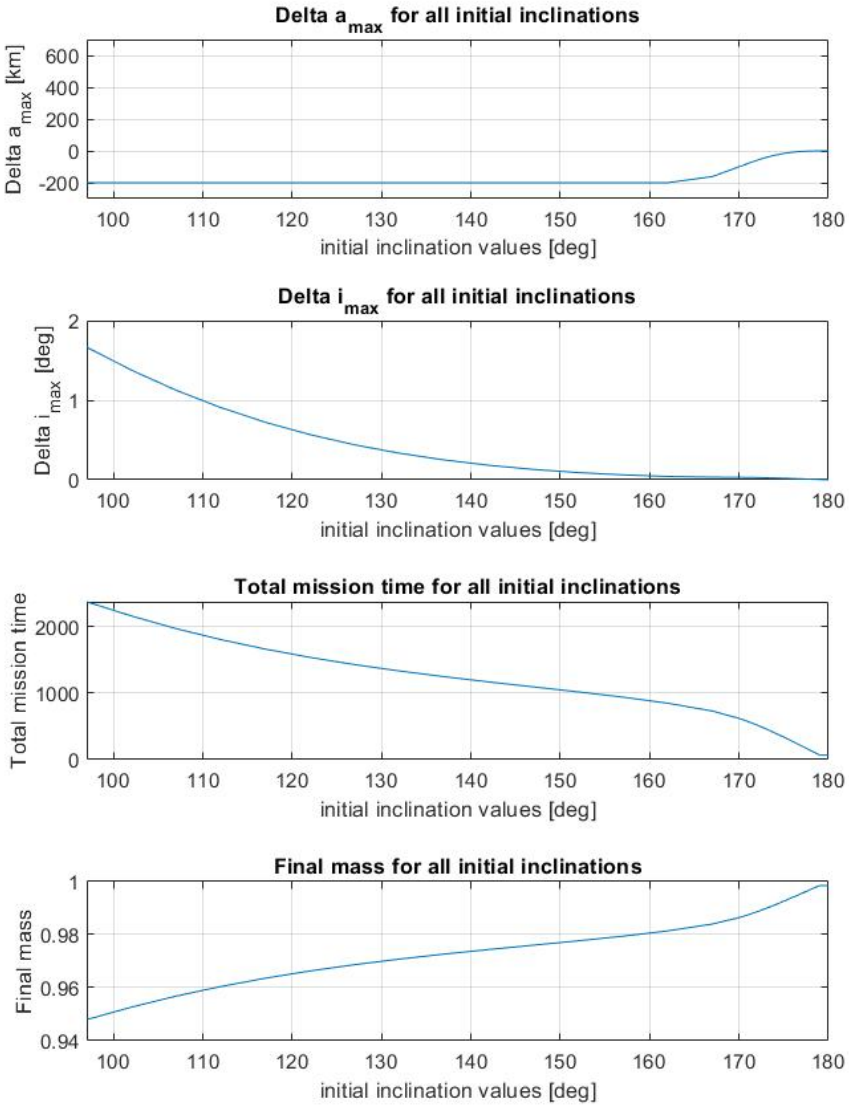

Figure 4.53: Trends for all initial inclination values

As show in the figure an the table above, all considerations that have been made before are confirmed.

It's now possible to move forward and analyze a new case with a negative pure change of RAAN. The new target conditions could be summarized as follows:

- $\Delta a = 0$ km
- $\Delta i = 0°$
- $\Delta\Omega$ = -10°

As done before, an adequately spaced interval of initial inclination values is selected between 97° and 180° and minimum time solution only is taken into account. The semimajor axis and inclinations trends could be visualized as follows (figure 4.57 and figure 4.58):

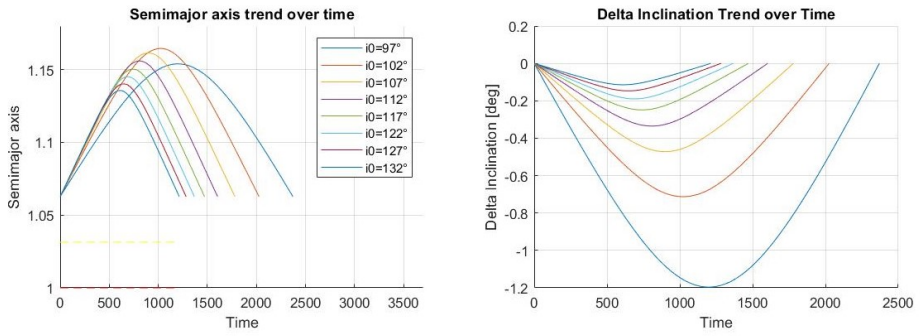

Figure 4.54: Semimajor axis and inclination trends over time

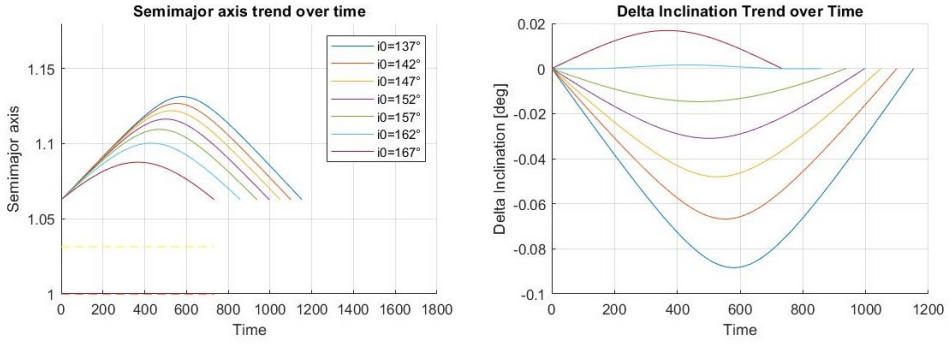

Figure 4.55: Semimajor axis and inclination trends over time

The semimajor axis maximum value raises as initial inclination value increases for i_0 that goes from 90° to 102°, where the cosine function of inclination assumes low values and the J_2 effect is weak. Then, when i_0 gets higher than 102°, the maximum value of altitude starts decreasing as initial inclination value increases due to a stronger J_2 effect that could be exploited. The inclination trend, on the other hand, has a negative minimum value that increases as initial inclination values increases and becomes positive for i_0 between 157° and 162°.
For further considerations, a thicker interval between 170° and 179° has been selected and the semimajor axis and inclinations trends could be visualized as follows (figure 4.59):

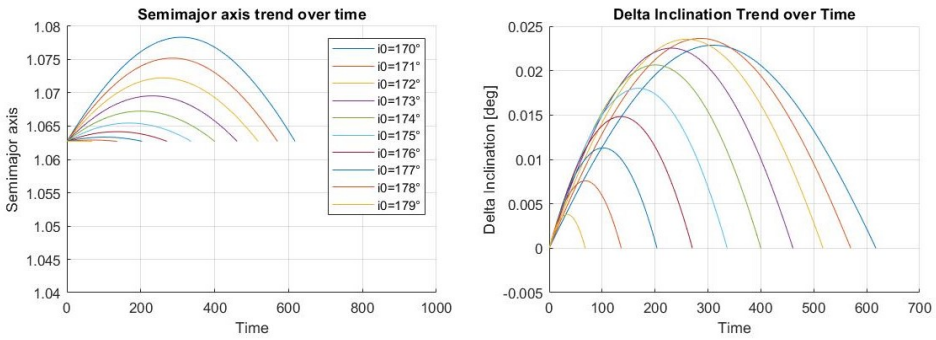

Figure 4.56: Semimajor axis and inclination trends over time

While the semimajor axis maintains the same trend, inclination maximum value increases as initial inclination value raises and change his behavior when i_0 gets higher than 170° and then it starts decreasing.
A visualization of the maximum value of altitude and Δ inclination trend over all different initial inclination values is made (table 4.9).

Table 4.9: Results for all initial inclination values

i_0	Δa_{max} [km]	Δi_{max} [deg]	t_f	m_f
97°	580.7010	-1.1960°	2370	0.9480
102°	648.3171	-0.7127°	2025	0.9556
107°	628.6012	-0.4720°	1780	0.9609
112°	593.5109	-0.3351°	1603	0.9648
117°	557.7296	-0.2487°	1470	0.9677
122°	524.3042	-0.1897°	1366	0.9700
127°	493.3939	-0.1469°	1283	0.9719
132°	464.3208	-0.1143°	1213	0.9734
137°	436.0773	-0.0884°	1153	0.9747
142°	407.3829	-0.0668°	1099	0.9759
147°	376.5404	-0.0480°	1049	0.9770
152°	341.1078	-0.0310°	997	0.9781
157°	297.2949	-0.0147°	937	0.9794
162°	239.0433	-0.0002°	858	0.9812
167°	158.3233	0.0168°	733	0.9839
170°	99.1440	0.0229°	617	0.9865
171°	79.1958	0.0236°	570	0.9875
172°	60.2231	0.0235°	517	0.9886
173°	43.0631	0.0225°	461	0.9899
174°	28.4912	0.0206°	400	0.9912
175°	17.0297	0.0180°	336	0.9926
176°	8.8164	0.0148°	271	0.9941
177°	3.5949	0.0113°	204	0.9955
178°	0.8089	0.0076°	136	0.9970
179°	-0.2708	0.0038°	68	0.9985

The respective trend over initial inclination values could be visualized as follows (figure 4.62):

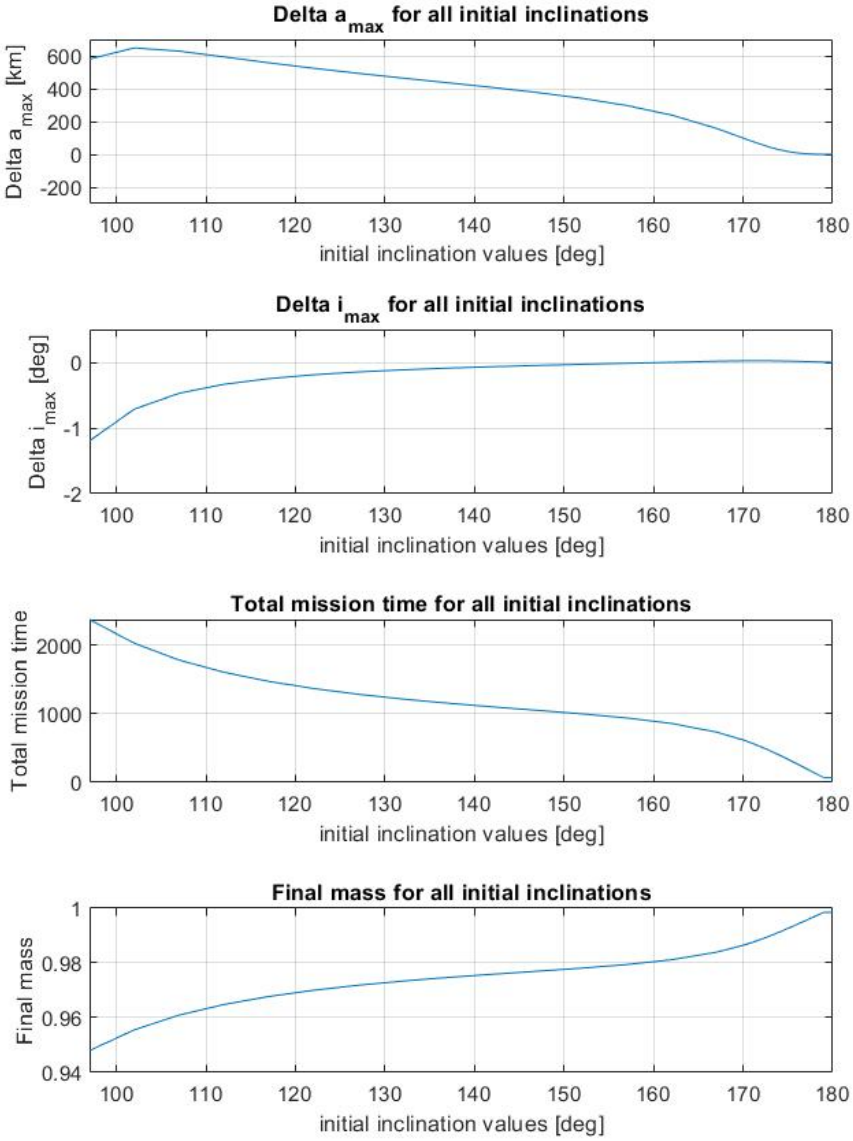

Figure 4.57: Trends for all initial inclination values

It's now possible to visualize the confrontation between the two different trends (figure 4.63).

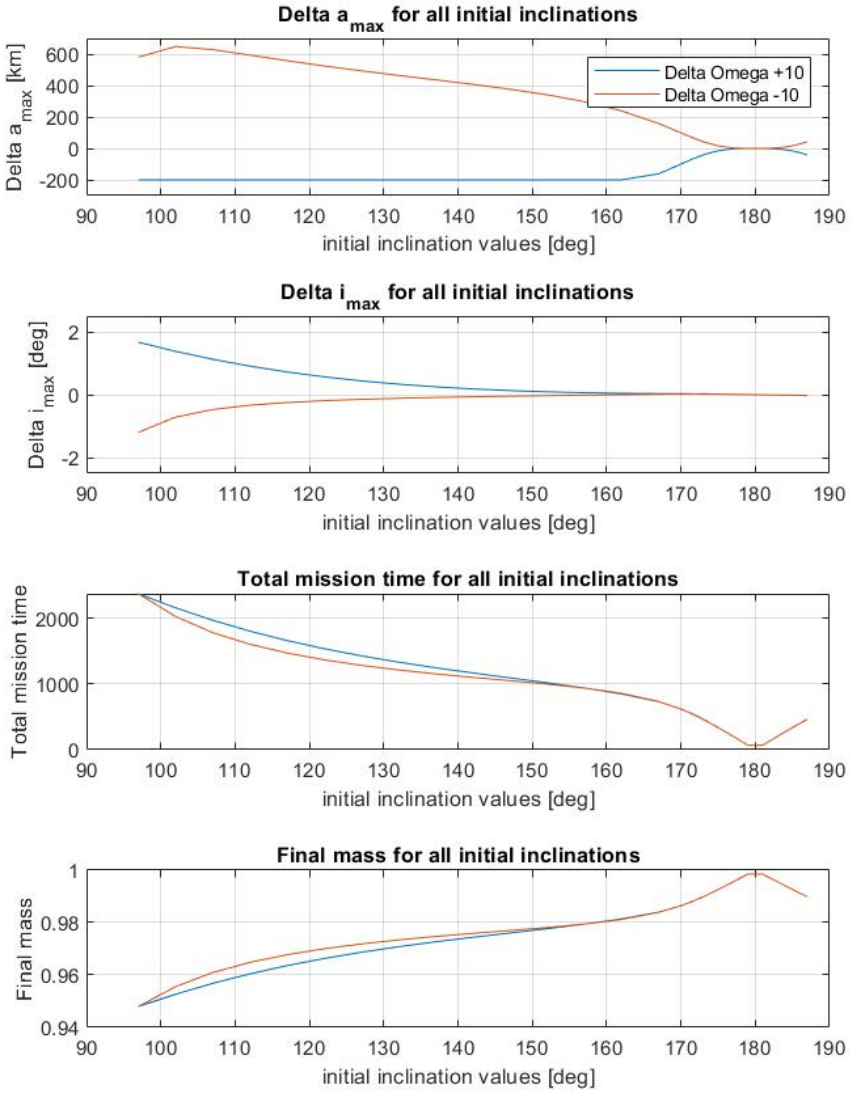

Figure 4.58: Confrontation between Trends for all initial inclination values

In conclusion, a confrontation between $\Delta\Omega = +10°$ and $\Delta\Omega = -10°$ solutions with respect to a interval of initial inclination values that goes from 0° to 180° could be made (figure 4.64).

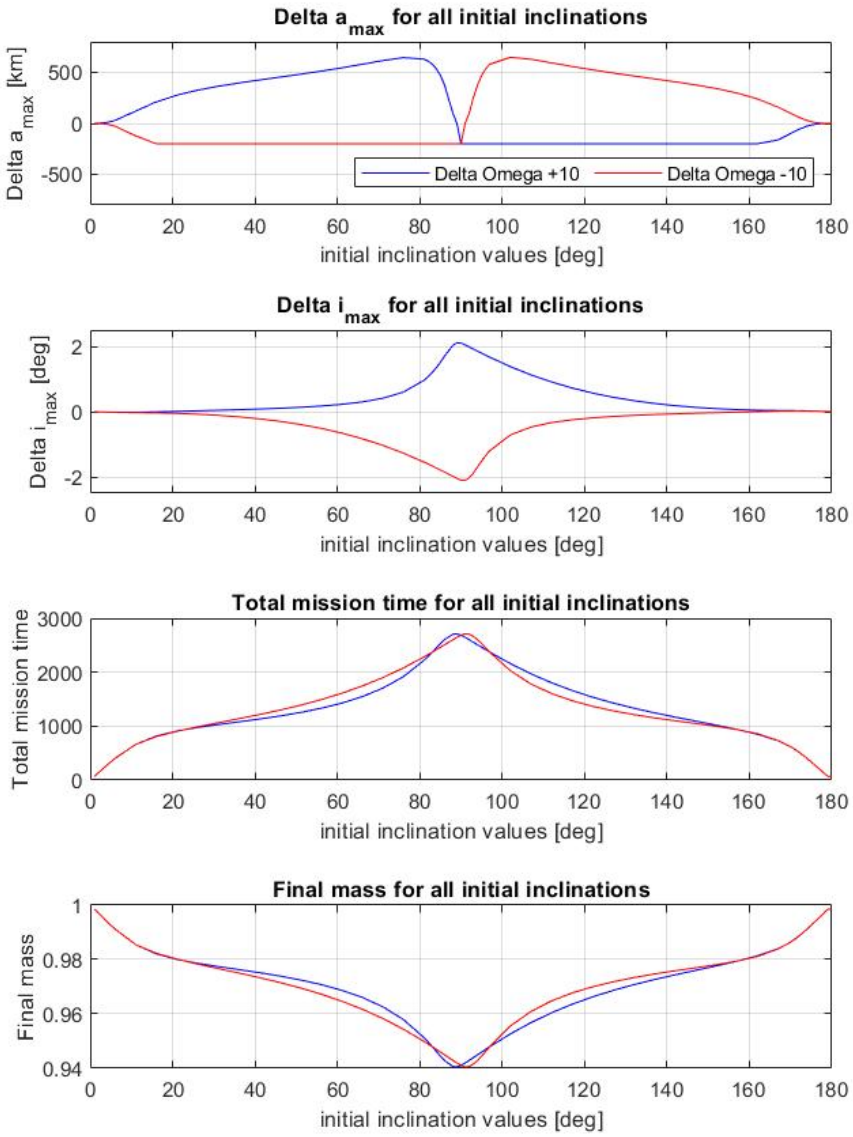

Figure 4.59: Confrontation between Trends for all initial inclination values

As expected, a visibile symmetry is show in both the semimajor axis and inclination trends, whereas the total mission time and final mass show some differences, this is due to the altitude constrain that is applied in different moment, based on the sign of $\Delta\Omega$.

5 Conclusion

The purpose of this study lies on the applicability of an indirect method for the optimization of low-thrust multi-revolution maneuver, using a modified version of the *Edelbaum's theory*, taking into account the J_2 effect, a gravitational perturbations due to the non-spherical shape of the Earth. The single target maneuver has been accomplished using electrostatic engines, such as Ion and Hall thrusters, in order to significantly reduce fuel consumption, which leads to a smaller quantity of propellant needed to be stored at the beginning of the mission.
The indirect method of optimization has been applied in two different ways. The first one leads to a *minimum time solution*, where the maneuver has been accomplished with the engine turned on throughout all the maneuver duration. Due to a shorter lapse of maneuver time, the J_2 effect exerts a weak influence on the solution. The second one leads to a *maximum final mass solution*, where the engine are turned off for an optimal amount of time, based on the total mission time, in order to exploit the J_2 effect to get the nodes of the satellite orbit and the target orbit closer. This contribution is totally free, since other types of perturbations haven't been taken into account and the total fuel consumption of the maneuver will result smaller than the one of the *minimum time solution*.
First of all, this method was applied to a well-defined initial and target conditions, varying the total mission time over the minimum time solutions. Generally speaking, both solutions converge without any problems with a total fuel consumption and ΔV required that decrease as time increases. After that, the target orbit conditions have been changed in order to study the behavior of all orbital parameters during the maneuver. The evolution trend of all orbital parameters was concordant with the theory on which the method is based on, with either an increase or decrease of inclination and semimajor axis to exploit the J_2 effect. Finally, a constrain altitude have been added for both types of solutions, in order to guarantee that the satellite wouldn't reach an altitude lower than 200km, forcing the β angle of thrust to become 90° and to use engines in order to maintain the right altitude.
In the second part of the work, the initial conditions have been changed to accomplish a pure change of RAAN between target and initial orbits. Even in this case, the method works almost perfectly with little problems of divergence for near-equatorial initial orbits and value of inclinations near

90°. The various solutions highlight a reduction of total mission time and fuel consumption for near equatorial orbits, whereas the cost is maximum for near polar orbits. In conclusion, this method turns out to be very accurate and suitable for the optimization of low-trust multi-revolution maneuvers. Further analysis could be conducted varying initial and target orbit conditions to reach a complete understanding of the phenomenon. Future development of this study could be conducted, such as the implementation of a multiple target problem, essential for active debris removal future application where multiple electrostatic engine kit could be deployed and attached to various debris, in order to de-orbit multiple targets in a single mission.

References

[1] Casalino, L. (2020). *Approximate Optimal LEO transfers with J2 perturbation*, Politecnico di Torino, Department of Mechanical and Aerospace Engineering, Corso Duca degli Abruzzi, 24, Torino, 10129, Italy

[2] Shen, H. X., Zhang, T. J., Casalino, L. and Pastrone, D. (2017). *Optimization of Active Debris Removal Missions with Multiple Targets*. Journal of Spacecraft and Rockets, 55(1), 181-189.

[3] Wakker, K.F. (2015). *Fundamentals of astrodynamics*, TU Delft Library, Delft.

[4] Bate, R., Muller, D., White, E. *Fundamentals of Astrodynamics*, Dover Publications, Inc., New York.

[5] Aziz, J. D. (2015). *Low-thrust Many-Revolution Trajectory Optimization*, Department of Aerospace Engineering Sciences, University of Colorado.

[6] Casalino, L. (2020). *Space Propulsion*, Politecnico di Torino, Department of Mechanical and Aerospace Engineering, Corso Duca degli Abruzzi, 24, Torino, 10129, Italy

[7] Todorov, E. (2006). *Optimal Control Theory*, Bayesian Brain, Doya, K. (ed), MIT Press (2006).

[8] *About space debris*, ESA [online]. Available at: https://www.esa.int/Safety_Security/Space_Debris/About_space_debris

[9] *Orbital debris*, eoPortal [online]. Available at: https://directory.eoportal.org/web/eoportal/satellite-missions/o/orbital-debris

[10] *Space Environment Statistics*, ESA's Space Debris User Portal [online]. Available at: https://sdup.esoc.esa.int/discosweb/statistics/

[11] *ESA's Annual Space Environment Report*, ESA Space Debris Office [online]. available at: https://www.sdo.esoc.esa.int/environment_report/Space_Environment_Report_latest.pdf

[12] *Space Debris Quarterly News*, National Aeronautics and Space Administration [online]. Available at https://orbitaldebris.jsc.nasa.gov/quarterly-news/pdfs/odqnv24i1.pdf

[13] *Hypervelocity Impact Technology*, Astromaterials Research and Exploration Science [online]. Available at https://hvit.jsc.nasa.gov/impact-images/space-shuttle.cfm

[14] Le Maya, S., Gehlya, S.,Carterb, B.A. , Flegela, S. (2018). *Space debris collision probability analysis for proposed global broadband*, Acta Astronautica,Volume 151, October 2018, Pages 445-455.

6 Acknowledgments

First of all i'd like to thanks professor *Lorenzo Casalino*, who assisted me and gave me the possibility to accomplish this final task, who was always available for any clarification throughout this period.

Then, i'd like to deeply thank all the people who have supported and guided me throughout all these years, without whom i wouldn't have succeeded in accomplishing my studies. I want to dedicate this success to them.

To my parents *Giorgo* and *Daniela* and my grandmother *Marcella*, who allowed me to undertake this journey and showed an endless patience in raising me throughout my entire life.

To my brother *Stefano*, who has been my source of inspiration and my role model. He has helped me avoiding wrong decisions and leaded me in the right path.

To my love *Paola* who truly loved and supported me throughout all my difficult moments, who has never gave up on me. Thanks for being my rock and for pushing me every day to be a better person.

To all my friends, who believed in me and pushed me to never give up.